

# Characterization of nanoparticles by continuous contrast variation in SAXS

Physikalisch-Technische Bundesanstalt

Raul Garcia Diez

July 27, 2016

# Characterization of nanoparticles by continuous contrast variation in SAXS

Physikalische-Technische Bundesanstalt

Raul Garcia-Diez

## Abstract

In the continuously growing field of nanomedicine, nanonoparticles have a pre-eminent position, opening exciting new possibilities as platforms for drug-delivery or encapsulating imaging agents. Indeed, polymeric colloids are starting to undergo clinical trials and a lipid vesicle was used as nanocarrier for the first approved nano-drug, Doxil®. Therefore, the current advances in nanomaterial development are focused towards tailoring polymeric nano-drug carriers with flexible surface functionalisation and controlled morphologies, defining aspects of the particle functions e.g. their *in vivo* biodistribution or their drug-delivery efficacy.

However, most current characterization techniques possess certain limitations i.e. cannot prove the innner structure present in many low-density nanoparticles. This work proposes a novel approach to contrast variation with SAXS [1] based on the constitution of a solvent density gradient in a glass capillary in order to choose *in situ* the most appropriate contrast and to acquire extensive datasets in a short time interval.

By examining the scattering curves measured at different aqueous sucrose densities, information about the internal morphology of the nanoparticles as well as their size distribution can be obtained. Additionally an estimation of the particle density can be determined focusing on the Guinier region of the curve, as shown for polymeric colloids across a wide spectrum of polymers [2]. These results were successfully compared with techniques such as DCS and several imaging methods.

The continuous contrast variation technique was also employed to characterize Doxil®, a PEGylated liposomal formulation of doxorubicin, using iodixanol as contrast agent, an iso-osmolar suspending medium. The study is focused on the isoscattering point position and the model-free analysis of the scattering curves and highlights the advantadges in comparison to widely used characterization techniques as DLS and TEM [3].

Furthermore, the response of the nanocarrier to increasing solvent osmolality is evaluated with sucrose contrast variation and compared to the different response of

PEGylated and plain liposomes to osmotic pressure depending on their size. For instance, the osmotic pressure needed for the liposomal shrinkage is quantitatively studied by focusing on the evolution of the isoscattering point intensity, which gives an insight into the Laplace law for small sized sterically stabilized liposomes and the role of the PEG moieties in the membrane resilience.

- [1] R. Garcia-Diez, C. Gollwitzer, M. Krumrey, *J. Appl. Cryst.* **48**, 20-28 (2015)
- [2] R. Garcia-Diez, A. Sikora, C. Gollwitzer, C. Minelli, M. Krumrey, *Eur. Polym. J.* (2016)
- [3] R. Garcia-Diez, C. Gollwitzer, M. Krumrey, Z. Varga, *Langmuir* **32** (**3**), 772-778 (2015)

# Contents

<b>1</b>	<b>Introduction: Nanoparticles in medicine and biology</b>	<b>6</b>
1.1	Polymeric colloids . . . . .	6
1.1.1	Functionalization for protein binding . . . . .	6
1.1.2	Polymerization consequences . . . . .	6
1.2	Liposomal nanocarriers . . . . .	6
1.2.1	Phospholipid bilayer . . . . .	6
1.2.2	polydispersity control . . . . .	6
1.2.3	Drug carrier and SSLs . . . . .	6
1.3	Physicochemical characterization . . . . .	7
1.3.1	Dimensional metrology and traceability . . . . .	7
1.3.2	Characterization tools . . . . .	7
<b>2</b>	<b>Theoretical Background</b>	<b>8</b>
2.1	Interaction of light and matter . . . . .	8
2.1.1	Beer-Lamber Law . . . . .	8
2.1.2	X-ray cross sections . . . . .	8
2.1.3	Thompson scattering . . . . .	8
2.1.4	Rayleigh and Mie scattering . . . . .	8
2.2	Small-angle X-ray scattering . . . . .	8
2.2.1	Physical process . . . . .	8
2.2.2	Evaluation of the scattering intensity . . . . .	8
2.3	Contrast variation . . . . .	10
2.3.1	Isoscattering point . . . . .	10
2.3.2	Basic functions approach . . . . .	11
2.4	Dynamic Light Scattering . . . . .	13
<b>3</b>	<b>Experimental setup for SAXS measurements</b>	<b>14</b>
3.1	BESSY II . . . . .	14

3.1.1	Insertion devices . . . . .	15
3.2	FCM Beamline . . . . .	16
3.2.1	Four-crystal monochromator . . . . .	16
3.2.2	Monitor diode: Flux monitor . . . . .	17
3.2.3	Reflectometer in vacuum: NewRef . . . . .	17
3.3	SAXS Setup . . . . .	18
3.3.1	Pilatus detector . . . . .	18
3.3.2	HZB SAXS instrument . . . . .	18
3.4	Sample environment . . . . .	21
3.4.1	Round capillaries . . . . .	21
3.4.2	Hilgenberg capillaries . . . . .	21
3.4.3	Prototype cell from zoltan . . . . .	22
3.5	Obtention of the scattering curves . . . . .	23
3.5.1	Absolute intensity calibration . . . . .	23
3.6	Small-angle X-ray scattering: DIRECT FROM PAPER . . . . .	24
3.6.1	Filling of capillaries . . . . .	25
3.6.2	Calibration of solvent density and finding of main axis . . . . .	25
3.6.3	Limitations . . . . .	26
<b>4</b>	<b>Contrast variation in SAXS with the density gradient technique</b>	<b>29</b>
4.1	Materials and Methods . . . . .	31
4.1.1	Particles and chemicals . . . . .	31
4.1.2	Diffusion time and calibration height . . . . .	31
4.2	Continuous contrast variation in SAXS on PS-COOH colloids . . . . .	32
4.3	Model dependent evaluation . . . . .	34
4.3.1	Core-shell form factor fit . . . . .	34
4.4	Model-free approach to contrast variation data . . . . .	36
4.4.1	Isoscattering point . . . . .	36
4.4.2	Guinier region . . . . .	38
4.5	Summary . . . . .	39
<b>5</b>	<b>Simultaneous size and density determination of polymeric colloids</b>	<b>42</b>
5.1	Materials and methods . . . . .	45
5.1.1	Particles and chemicals . . . . .	45
5.1.2	Differential Centrifuge Sedimentation (DCS) . . . . .	46
5.2	Technique validation for the determination of the particle size distribution . . . . .	48
5.2.1	Inter-laboratory comparison of the mean particle size . . . . .	50

5.2.2	Colloidal size distribution . . . . .	52
5.3	Considerations about contrast variation data evaluation . . . . .	54
5.3.1	Shape factor formalism . . . . .	54
5.3.2	Isoscattering point approach . . . . .	55
5.4	Determination of the particle physical density . . . . .	57
5.4.1	Validation through comparison with DCS . . . . .	58
5.4.2	Use for homogenous polymeric colloids . . . . .	58
5.5	Summary . . . . .	60
<b>6</b>	<b>Continuous contrast variation applied to relevant bio-materials</b>	<b>61</b>
6.1	Materials and methods . . . . .	62
6.1.1	Caelyx®: PEGylated liposomal doxorubicin . . . . .	62
6.1.2	Lipid vesicles: PEGylated and plain liposomes . . . . .	64
6.1.3	Human lipoproteins . . . . .	64
6.1.4	PS-COOH particles coated with IgG . . . . .	65
6.2	Traceable size determination of a liposomal drug . . . . .	66
6.2.1	Isoscattering point approach . . . . .	67
6.2.2	Shape factor calculation . . . . .	68
6.2.3	Average electron density . . . . .	70
6.3	Osmotic effects in liposomes . . . . .	71
6.3.1	Application to drug-stabilized liposomes . . . . .	72
6.3.2	Does PEGylation affect the osmotic activity of liposomes? . .	75
6.4	Sizing of blood plasma components . . . . .	83
6.5	Protein-coated low-density nanoparticles . . . . .	86
6.5.1	Hard protein corona characterization with contrast variation .	89
6.6	Summary . . . . .	91

# Chapter 1

## Introduction: Nanoparticles in medicine and biology

### 1.1 Polymeric colloids

#### 1.1.1 Functionalization for protein binding

#### 1.1.2 Polymerization consequences

initiator, co-monomer, surfactants

### 1.2 Liposomal nanocarriers

formation from amphiphilic lipids

#### 1.2.1 Phospholipid bilayer

typical lipid HSPC, DPPC, cholesterol, PEG

#### 1.2.2 polydispersity control

extrusion, paper with zoltan about scattering in SSLs

#### 1.2.3 Drug carrier and SSLs

stealth function, bilayer stability, filling with pH gradient

## **1.3 Physicochemical characterization**

### **1.3.1 Dimensional metrology and traceability**

### **1.3.2 Characterization tools**

#### **Single-particle method**

AFM, TEM, SEM, TSEM

#### **Ensemble methods**

DLS, DCS, SAXS



# Chapter 2

## Theoretical Background

### 2.1 Interaction of light and matter

#### 2.1.1 Beer-Lamber Law

#### 2.1.2 X-ray cross sections

#### 2.1.3 Thompson scattering

Elastic scattering by a single electron

#### 2.1.4 Rayleigh and Mie scattering

Scattered by an ensemble of electrons.

Differences depend on wavelength and size of the object

### 2.2 Small-angle X-ray scattering

#### 2.2.1 Physical process

#### 2.2.2 Evaluation of the scattering intensity

Form factor \*  $S(q)$  Electron density Number of colloids

**What is  $q$ ?**

## Modelling of the scattering curve

What about size distributions? Log-normal, gaussian, Monte-carlo free number of sizes (Pauw)

The scattering intensity of an ensemble of randomly oriented nanoparticles in suspension can be expressed as a function of the momentum transfer  $q$ , modulus of the scattering vector  $\vec{q}$ , as

$$I(q) = N \int_0^\infty g(R) |F(q, R)|^2 dR, \quad (2.1)$$

where  $N$  is the number of scatterers,  $g(R)$  is the size distribution function and  $F(R)$  is the particle form factor, which depends on the inner radial structure of the particle. If the particle shows a heterogeneous morphology, the form factor differs qualitatively for different suspending medium densities. For sufficiently monodisperse particle suspensions, the Fourier region of the scattering curve shows pronounced minima that characterize the particle structure.

For a typical morphology with sharp interfaces between the radial symmetric components of the particle with radius  $R_i$  the form factor is

$$F(q, R) = \Delta\eta f_{sph}(q, R) + \sum_{i=1}^{n-1} \Delta\rho_i (f_{sph}(q, R_{i+1}) - f_{sph}(q, R_i)), \quad (2.2)$$

where  $R$  is the external radius of the particle,  $n$  is the number of concentric shells and  $f_{sph}$  is the form factor of a homogeneous solid sphere given by

$$f_{sph}(q, R) = \frac{4}{3}\pi R^3 \left( 3 \frac{\sin qR - qR \cos qR}{(qR)^3} \right). \quad (2.3)$$

Sphere Gudrun polymeric colloids???

In the case of the PMMA-COOH colloids, the form factor is calculated for a homogeneous solid sphere with electron density  $\rho_0$ :

$$f_{sph}(q, R) = \frac{4}{3}\pi R^3 \left( 3 \frac{\sin qR - qR \cos qR}{(qR)^3} \right) = \frac{F(q, R)}{\rho_0}. \quad (2.4)$$

Core-shell Interface effects???

The model represents a radially symmetric particle with a sharp interface between the outer shell and the inner core. The form factor is described by

$$F(q, R) = \Delta\eta f_{sph}(q, R) + \Delta\rho [f_{sph}(q, R) - f_{sph}(q, R_{core})], \quad (2.5)$$

where  $R$  and  $R_{core}$  are the outer shell and inner core radii respectively, the excess of electron density is  $\Delta\rho = \rho_{shell} - \rho_{core}$  and the contrast is expressed as  $\Delta\eta = \rho_{core} - \rho_{solv}$ , where  $\rho_{solv}$  is the electron density of the suspending medium.

Onion model It can be used for single-SAXS experiment maybe

Vesicle 5 gaussian????

Conclusion of background  $a+b*q-4$

Double shell model Used in the protein-coated Kisker NPs (last chapter)

### Guinier approximation

deviation when using too few point Polydispersity effects

## 2.3 Contrast variation

Solvent variation

ASAXS

When analyzing contrast variation data, a widespread theoretical approach is based in the non-interacting model proposed by Stuhrmann & Kirste 1965; 1967 for monodisperse particles. The so-called *basic functions* formulation differentiates, independently of the particle inner structure, the contributions which depend on the varying solvent density or contrast ( $\Delta\eta = \rho_{core} - \rho_{solv}$ ) and on the excess of electron density of each component  $\Delta\rho_i = \rho_i - \rho_{core}$ .

### 2.3.1 Isoscattering point

One of the best known features appearing in a contrast variation experiment is the existence of *isoscattering points*. At these specific  $q$ -values, the scattering intensity is independent of the adjusted solvent contrast, i.e. all scattering curves intersect in the isoscattering points regardless of the contrast. The isoscattering points  $q^*$  are particularly interesting because they emerge for any spherical particle with an inner structure and a sufficiently narrow size distribution. From the contrast-depending

part of equation (2.2), a model-free expression can be derived which relates the position of the isoscattering points  $q_i^*$  with the external radius of the particle  $R$ , independent of its radial structure Kawaguchi & Hamanaka (1992):

$$\tan(q_i^* R) = q_i^* R \quad (2.6)$$

The positions of the isoscattering points correspond to the minima positions of the scattering intensity of a compact spherical particle with radius  $R$ . Although this expression is derived for the monodisperse case, it can still be applied up to a moderate degree of polydispersity, if care is taken regarding the shift of the minima position due to polydispersity van Beurten & Vrij (1981). If defining the polydispersity degree  $p_d$  as the full width half maximum of the particle size distribution divided by its average value, for size distributions with  $p_d$  larger than  $\approx 30\%$ , the isoscattering point is not well defined and the intersection point of the curves is smeared out, showing a diffuseness in the isoscattering point position Kawaguchi & Hamanaka (1992).

### Possible deviations

Polydispersity and ellipticity smearing (simulation, calculation)

### 2.3.2 Basic functions approach

When analyzing contrast variation data, a widespread theoretical approach is based in the non-interacting model proposed by Stuhrmann & Kirste (1965; 1967) for monodisperse particles. The so-called *basic functions* formulation differentiates, independently of the particle inner structure, the contributions which depend on the varying solvent density or contrast ( $\Delta\eta$ ) and on the excess of electron density of each component of the particle.

Deriving from this approach, the scattering intensity can be expressed as the combination of contributions corresponding to different features of the particles:

$$I(q) = I_c(q) + \Delta\eta I_{sc}(q) + (\Delta\eta)^2 I_s(q) \quad (2.7)$$

The  $I_c$  function contains the contributions from the density fluctuations inside the particle, the contribution  $I_s$  is the so-called *resonant term* and  $I_{sc}$  is the cross-term function.

### Shape factor

The  $I_s(q)$  function, also known as *shape factor*, corresponds to the scattering contributions from particles with homogenous density and a size equivalent to the volume

inaccessible to the solvent. By modelling the shape factor function, the shape and size distribution of the polymeric colloids can be determined independently of their inner structure.

For this purpose, a spherical form factor for homogeneous colloids with a gaussian size distribution was utilized, similarly to the PMMA-COOH example. In order to obtain the particle sphericity, an ellipsoid model was employed.

## Guinier law

### Gyration radius

The radius of gyration  $R_g$  is systematically employed in small-angle scattering as an evaluation tool Mertens & Svergun (2010); Sim *et al.* (2012). It can be calculated using the Guinier approximation Guinier (1939); Guinier & Fournet (1955), which assumes that the scattering intensity behaves in the limit of small  $q$  as

$$I(q) = I(0) \exp \left( -\frac{R_g^2}{3} q^2 \right), \quad (2.8)$$

where  $I(0)$  is known as forward scattering or intensity at zero angle. Using the basic functions approach, the radius of gyration of a monodisperse, heterogeneous particle can be expressed as a function of the solvent electron density  $\rho_{solv}$  and the average electron density of the particle  $\rho_0$  Feigin & Svergun (1987)

$$R_g^2 = R_{g,c}^2 + \frac{\alpha}{\rho_0 - \rho_{solv}} - \frac{\beta}{(\rho_0 - \rho_{solv})^2}, \quad (2.9)$$

where  $R_{g,c}$  is the radius of gyration of the particle shape corresponding to the volume inaccessible for the solvent  $V_c$ ,  $\alpha$  characterizes the distribution of different phases inside the particle and  $\beta > 0$  considers the eccentricity of the different scattering contributions Stuhrmann (2008). Nevertheless, particle aggregation influences the scattering curves especially in the Guinier region and must be explicitly avoided.

Avdeev (2007) proposed an extended version to equation (2.9) for the case of a polydisperse particle ensemble by introducing the *effective* values  $\tilde{R}_{g,c}^2$ ,  $\tilde{\alpha}$  and  $\tilde{\beta}$ , which are the intensity-weighted averages of the corresponding parameters over the polydispersity. The observed average electron density is not affected by the polydispersity ( $\tilde{\rho}_0 = \rho_0$ ) if the volume ratio between the different particle components is constant for all particles in the ensemble.

Assuming the same premise, the intensity at zero angle is given by

$$I(0) \propto N (\rho_0 - \rho_{solv})^2, \quad (2.10)$$

with a minimum at  $\rho_{solv} = \rho_0$ . Therefore, by analyzing the Guinier region of the scattering curves, the average electron density of the particle can be obtained without assuming an *a priori* inner structure.

Using the models presented above, it is possible to obtain by independent means the external radius and the average electron density of the particle in suspension.

$I(0)$

what happens in polydisperse systems?

## 2.4 Dynamic Light Scattering

The technique was used extensively in this thesis.

# Chapter 3

## Experimental setup for SAXS measurements

### 3.1 BESSY II

#### Electron Accelerator

The electron beam creates the free electrons: a hot thermionic cathode emits electrons which are accelerated with a high voltage to the anode until they reach energies up to 70 keV. The free electrons are transferred to a linear pre-accelerator which accelerates electrons to relativistic velocities up to  $0.99c$  via an electric field. The electrons are then inserted into the microtron, which further accelerates the electrons to 50 MeV, at which point they are injected into the synchrotron. The acceleration process takes 50 ms and can be repeated with a repetition rate of 10 Hz with successive injection of electrons. Inside the synchrotron, a set of magnets are disposed in such a way as to lead the electrons in circular trajectories, whilst high frequency (HF) resonators in linear paths of the synchrotron, temporally coupled with the magnets, further accelerate the electrons to 1.72 GeV <sup>18</sup>.

#### Storage ring

The threshold energy is reached when a high electron flux with high temporal stability is achieved. At this point the electrons are injected into the storage ring, where bending magnets are implemented to maintain the circular trajectory of the electron, as shown in Figure 3.1. The storage ring has a circumference of 240 meters and the successive injection of electrons from the synchrotron leads to currents of approximately 290 mA in the initial stage (after injection).

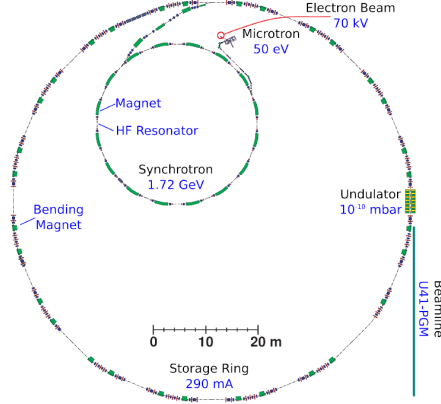


Figure 3.1: A scheme of BESSY II. From the master thesis.

### 3.1.1 Insertion devices

#### Bending magnet and bremsstrahlung radiation

It is known that relativistic electrons lose kinetic energy due to the Bremsstrahlung process (BLUMENTHAL & GOULD 1970) when they are accelerated or decelerated. This energy loss in the storage ring is compensated by high frequency resonators situated on a short linear section. In the case of a storage ring with circular shape, the electron bunches are accelerated radially (a perp v) and emit synchrotron radiation tangentially to the bunch trajectory. The power emitted

Total radiated power:

$$P = \frac{e^2 \gamma^4}{6\pi \epsilon_0 c} \left( \dot{\beta}^2 + \frac{(\vec{\beta} \cdot \dot{\vec{\beta}})^2}{1 - \beta^2} \right) \quad (3.1)$$

where  $\vec{\beta} = \frac{\vec{v}}{c}$  and  $\gamma = \frac{1}{\sqrt{1 - \beta^2}}$  is the Lorentz factor.

If the trajectory of the electrons and the acceleration are perpendicular, for circular particle trajectories:

$$P_{a \perp v} = \frac{e^2 \gamma^4}{6\pi \epsilon_0 c} \dot{\beta}^2 = \frac{e^2 \gamma^4 a^2}{6\pi \epsilon_0 c^3} \quad (3.2)$$

#### Other devices: Wigglers and undulators

High photon flux

The energy range is also different.



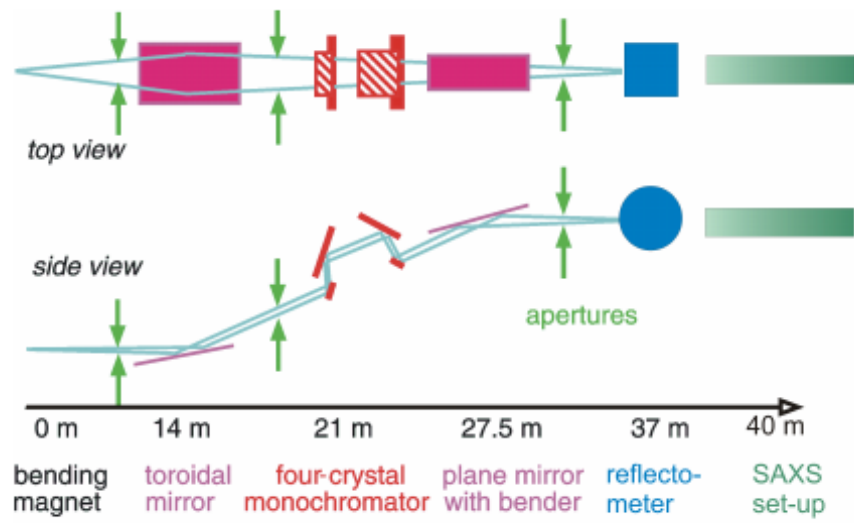


Figure 3.2: A scheme of BESSY II. From the master thesis.

Deflection parameter  $K$ . The difference between both types of devices is  $K$ . Normally you can vary  $K$  by increasing the space in the magnetic field (gap).

$$K = \frac{eB_0\lambda_0}{m_0 2\pi c} \quad (3.3)$$

## 3.2 FCM Beamline

Talk a little bit about design with mirrors and collimation

focused on the sample and collimated into a 0.5 mm circular spot by Ge pinholes situated between the sample and the monochromator

### 3.2.1 Four-crystal monochromator

energy resolving power  $E/\Delta E$  of  $10^4$

Energy resolution

Typical flux on the sample

Difference between Si and InSb

Beam size on the sample, divergence (talk to Mika)

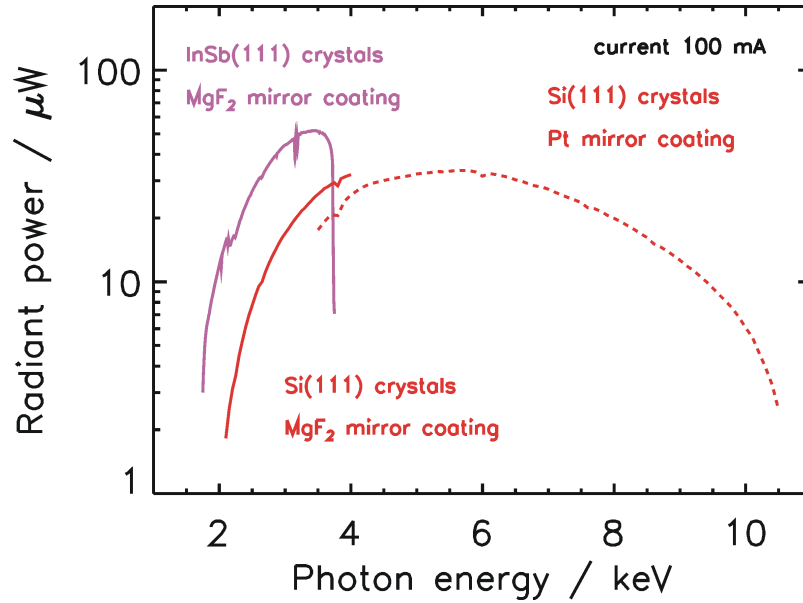


Figure 3.3: Typical flux scheme of the FCM Beamline

### 3.2.2 Monitor diode: Flux monitor

Continuous measurement of the incoming photon flux with a semitransparent silicon diode 8  $\mu\text{m}$  thick. It can be used down until 3 keV approx.

Avoiding possible fluctuations on the flux. TopUp mode should improve this but still there are variation between 297 and 299 mA which are around 1%

### 3.2.3 Reflectometer in vacuum: NewRef

goniometer allowing us to move with high precision

The rectangular capillary is placed in a sample holder which allows the movement with micrometer precision in the directions perpendicular to the incoming beam, as depicted in figure 3.7.

### Transmission measurements

calibrated diodes, SYRES II???? Calibrated against cryo-radiometer every 3 years.

To measure the total flux and sample transmission, photodiodes were used which were calibrated against a cryogenic electric substitution radiometer with a relative uncertainty of 1 % Krumrey & Ulm (2001).

very thick silicon diodes

Table 3.1:  $q$ -range available for the different experimental setups at extreme conditions. **CHECK FOR TRUE VALUES**

	<b>SAXS</b>	<b>WAXS</b>
Distance (mm)	4500	700
Energy (eV)	3500	10000
$q_{min}$ ( $\text{nm}^{-1}$ )	0.015	0.5
$q_{max}$ ( $\text{nm}^{-1}$ )	1	7

around 0.5 % uncertainty

### 3.3 SAXS Setup

How do we measure small-angle x-ray scattering?

#### 3.3.1 Pilatus detector

high dynamic range

noise free

A vacuum-compatible Pilatus 1 M hybrid pixel detector (Dectris Ltd, Baden, Switzerland) with a pixel size of  $d = (172.1 \pm 0.2) \mu\text{m}$  collected the scattered X-ray photons

#### 3.3.2 HZB SAXS instrument

Collaboration with HZB (the SAXS setup of the Helmholtz-Zentrum Berlin (HZB))

Continuos distance movement between 1.5 and 3.7 m (or so)

The distance variability is provided by bellows which allow a travel range of about 2.3 m.

Possibility to extract the bellows (WAXS)

Which  $q$ -range are available for each distance and energy? Small table for high and low energy

#### Calibration of the distance

Typically 10-4 uncertainty

Typically 30 seconds measurement at every 50 mm, forwards and backwards to increase accuracy.

Optical encoder with micrometer precision

Using AgBehe to triangulate the sample-detector distance

Before it was done only with the position of the AgBehe but we realized that the crystal lattice depended on the chemical preparation (image comparing Alfa Aesar and MTA silver benehate)

Another reference standard such as SBA (mesoporous silica, SBA-15 Zhao *et al.* (1998)) was used for calibration at long distances (larger periodic distance, Eike material???)

Using a distance range of 1300 mm, moving every 50 mm and with a measurement time of 15 s with an energy of 9000 eV, the AgBehe sample achieve a relative uncertainty in the distance of 0.02 %. This deviations at long distances are visible in the inset of figure 3.4b.

In figure 3.4b, it can be also observed how this deviations dissappears at long distances for SBA-15. In this case, the uncertainty is 0.004 %

#### REAL MEASUREMENT, WHOLE DISTANCE

Using a distance range of 2200 mm, moving every 100 mm and with a measurement time of 10 s with an energy of 8000 eV, the AgBehe sample achieve a relative uncertainty in the distance of 0.03 % (1.5 mm). This deviations at long distances are visible in the inset of figure 3.4b, by looking at the residuals for short distance. We just used the region for distances larger than 1000 mm.

In figure 3.4b, it can be also observed how this deviations dissappears at long distances for SBA-15. In this case, the uncertainty is 0.007 % (0.3 mm)

There is always a factor 5 between the uncertainties of SBA-15 and AgBehe. The best uncertainty achieved is with SBA and moving every 50 mm and longer exposure times (0.004 % (0.2 mm))

In figure 3.4a we can see how AgBehe has problems at long distances. We can only use it for Pilatus Pos larger than 1000 mm.

The uncertainty of the fit (around 0.2 mm and 0.8 mm for AgBehe) is smaller than the difference between the 2 measurements (0.5 mm). Besides, the thickness of the sample is only approx in 0.5 mm. Therefore, the overall uncertainty that we can give is exactly 0.5 mm, which corresponds to 0.5 mm/4630 mm, 0.01 %

The position of the peak of AgBehe is  $1.0765 \text{ nm}^{-1}$  (FWHM  $0.06 \text{ nm}^{-1}$ , ratio is 5.5 %), while the peak position of SBA is  $0.681 \text{ nm}^{-1}$  (FWHM  $0.018 \text{ nm}^{-1}$ , ratio is 2.6 %). The peak of SBA-15 obviously narrower, that is why the uncertainty is also smaller.

Good from AgBehe is that the position of the peak is always at  $1.0766 \text{ nm}^{-1}$  Blanton *et al.* (1995) (with a crystal parameter of 58.36 angstroms, giving  $1.07553 \text{ nm}^{-1}$ ) and varies only 0.5 %. Nevertheless, by radiation it can create small silver

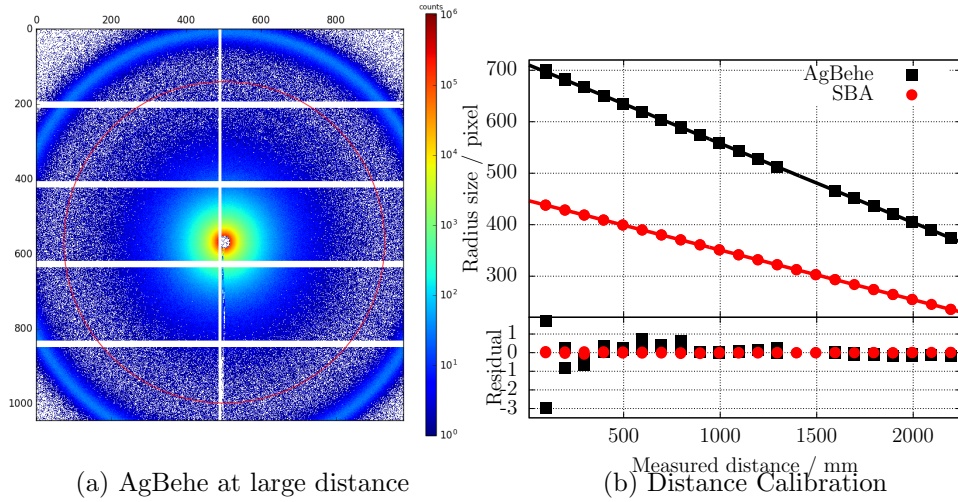


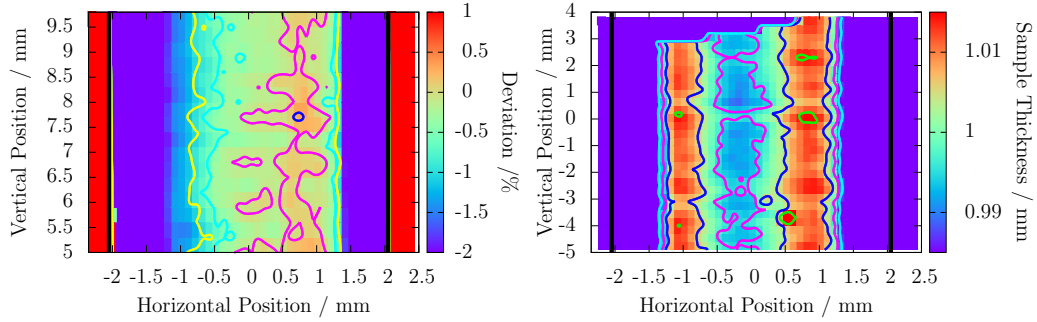
Figure 3.4: Sample-to-detector distance calibration by triangulation: a) Problems of the AgBehe sample for large distances (measured at 8 keV and a distance of 995.5 mm, file "messung kmc daten 2015 1Q pilatus 201501 0394.tif"), b) Comparison between AgBehe and SBA. The challenges of AgBehe for large distances is highlighted in the inset.

nanoparticles which increase the background Liu *et al.* (2006) thermal decomposition of AgBehe.

On the other hand, SBA-15 has a narrower peak which is visible along a wider distance range and gives better statistics for the fit. However, the position of the peak is strongly dependent on the preparation (e.g. calcination time, mesopores size is tunable as explained in paper from zhao...), and can vary until 1 % (the shape also depends on the chemical preparation). Radiation damage effects are visible for short calcination times.

### Other standard materials

dry rat tail tendon collagen with a d-spacing of 6.5 angstroms Amenitsch *et al.* (1997) rat tail tendon collagen fibres. Features from three hierarchical levels are recognized simultaneously, i.e. the meridional helix diffraction peak at 2.9 angstroms from the triple helical molecules (1), the equatorial ordering peak from the lateral order of the collagen fibrils at 11.5 angstroms (2) and the third-order reflection from the lateral staggering of the collagen molecules at 217 angstroms (3) [see e.g. Wess (2005)]



(a) Deviation from glass transmission (thickness of the capillary)  
(b) Sample thickness with water. Transmission divided by glass in order to get water transmission and  $\mu$

Figure 3.5: Hilgenberg capillaries homogeneity

## 3.4 Sample environment

### 3.4.1 Round capillaries

where to buy them and sizes

Borosilicate glass 3.3

We used capillaries with a nominal inner diameter of 1 mm and a wall thickness of 0.05 mm. A length of 100 mm is typical. WJM Glass (Berlin, Germany)

The sample is filled into it with an medical syringe with a long thin injection needle.

### 3.4.2 Hilgenberg capillaries

vacuum-proof borosilicate glass capillaries from Hilgenberg (Malsfeld, Germany) with a rectangular cross section of  $(4.2 \pm 0.2) \times (1.25 \pm 0.05) \text{ mm}^2$ , a length of  $(80 \pm 0.5) \text{ mm}$  and a wall thickness of ca.  $120 \mu\text{m}$ . (nominal values)

where to buy them and sizes

very homogenous glass thicknes (borosilicate glass)3.5a

very homogenous sample thickness 3.5b

perfect for precise measurement

the uncertainty is even smaller when using the main vertical axis of the rectangular capillaries

we can see how the glass thickness (grey line) is very regular along the main axis, with a transmission of around 0.2 +- 0.01

the same for the water transmission (black line)

By fitting a line to the glass transmission, the relative error of the transmission is 0.04 %. The relative uncertainty of the glass thickness is calculated by  $\delta_r d = \frac{\delta_r T}{\log(T)}$  and gives 0.03 %

Dividing the measured transmission in water (ur 0.05%) over the air transmission (ur 0.04%) ( $T_{\text{water}} = 35 \%$ ), we obtain the transmission of only water and with that, the thickness of the sample. The uncertainty of the water transmission is 0.06% and the sample thickness has an uncertainty of 0.06%, by calculating  $\delta_r d = \frac{\delta_r T}{\log(T)}$ .

Summary: When measuring along the main axis of the capillary, the glass thickness has an associated uncertainty of 0.03 % and the sample thickness of 0.06 %.

#### MORE CONSERVATIVE UNCERTAINTY

the uncertainty is even smaller when using the main vertical axis of the rectangular capillaries

we can see how the glass thickness (grey line) is very regular along the main axis, with a transmission of around 0.201 +- 0.001

the same for the water transmission (black line)

By fitting a line to the glass transmission, the relative error of the transmission is 0.6 %. The relative uncertainty of the glass thickness is calculated by  $\delta_r d = \frac{\delta_r T}{\log(T)}$  and gives 0.4 %

Dividing the measured transmission in water (ur 0.7%) over the air transmission (ur 0.6%) ( $T_{\text{water}} = 35 \%$ ), we obtain the transmission of only water and with that, the thickness of the sample. The uncertainty of the water transmission is 0.9 % and the sample thickness has an uncertainty of 0.9%, by calculating  $\delta_r d = \frac{\delta_r T}{\log(T)}$ .

Summary: When measuring along the main axis of the capillary, the glass thickness has an associated uncertainty of 0.4 % and the sample thickness of 0.9 %.

cut the part of the galden. Is not giving us any extra information

### 3.4.3 Prototype cell from zoltan

In the first setup, used to access the q-range describing the overall size of the vesicles, the sample-to-detector distance was 4.4 m and the energy of the incoming X-ray beam was set to 4 keV (wavelength 0.31 nm). Due to the short penetration length of X-rays at this energy, a custom-made sample holder was used utilizing silicon-nitride windows (NX7150E, Norcada Inc., Edmonton, Canada)

by a dedicated sample cell with thin silicon nitride windows.

silicon nitride windows. Low scattering and low absorbance.

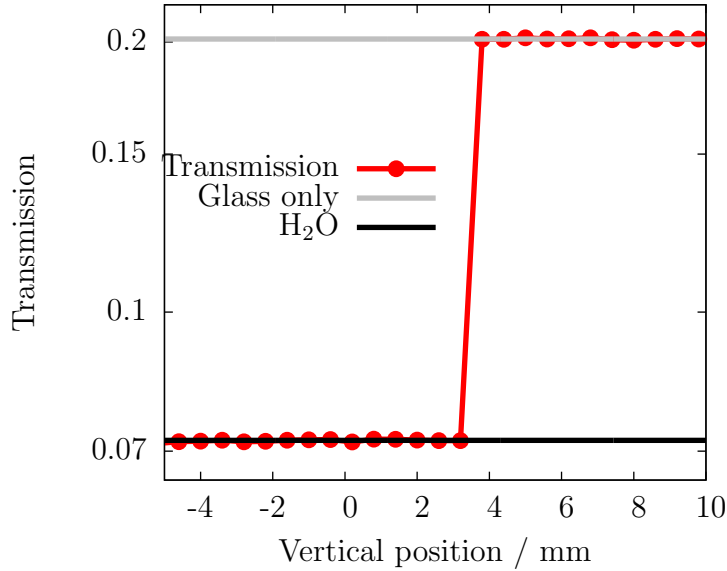


Figure 3.6: Transmissoin along the y-axis at x=-0.15 mm

where to buy them and sizes? 500 nm thickness, spacer cut with microtome in Hungary (which thickness?)

Used to increase the q-range as it enables the measurement until energies around 3 eV. We achieve much smaller q values (cite zoltans paper with the PEG-vesicle???)

## 3.5 Obtention of the scattering curves

The obtained scattering curve was normalized to the exposure time, the measured suspension transmittance and the incident photon flux, measured by means of a calibrated transparent silicon diode.

Radial integration and error propagation

### 3.5.1 Absolute intensity calibration

lupolen as standard material Kratky *et al.* (1966); Shaffer & Hendricks (1974)

glassy carbon Perret & Ruland (1972) use the knowledge from the innanopart project??????



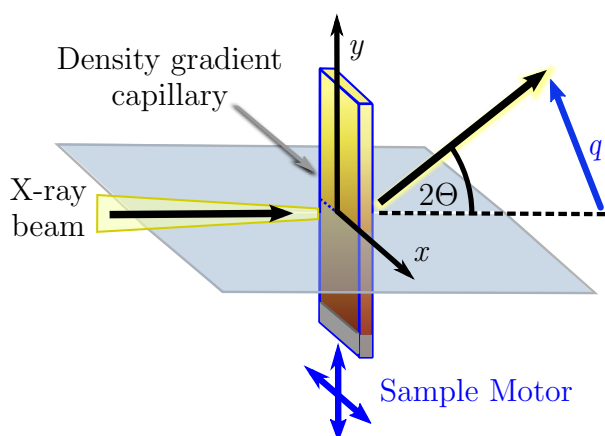


Figure 3.7: The rectangular density gradient capillary is placed in the X-ray beam and can be moved by sample motors in both directions perpendicular to the incoming beam.

### Flux monitor

thin diode

### Detector efficiency

pilatus and thin diode

—————THIS SHOULD ALL GO TO THE NEXT CHAPTER—————

## 3.6 Small-angle X-ray scattering: DIRECT FROM PAPER

The measurements were performed at the four-crystal monochromator beamline in the PTB laboratory at the electron storage ring BESSY II (Berlin, *Germany*), which provides highly intense, collimated synchrotron radiation focused on the sample and collimated into a 0.5 mm circular spot by Ge pinholes situated between the sample and the monochromator with an energy resolving power  $E/\Delta E$  of  $10^4$ . To measure the total flux and sample transmission, photodiodes were used which were calibrated against a cryogenic electric substitution radiometer with a relative uncertainty of 1 % Krumrey & Ulm (2001).

The rectangular capillary is placed in a sample holder which allows the movement with micrometer precision in the directions perpendicular to the incoming beam, as

depicted in figure 3.7. In order to determine the central vertical capillary axis, a horizontal X-ray transmission scan is performed at two different vertical positions of the capillary spaced by 20 mm. The central vertical axis can be drawn from the centers of both measurements and the sample can be moved along this axis by the simultaneous operation of the vertical and horizontal motors.

The sample was moved in steps of 0.5 mm along the central vertical capillary axis and exposed at each position for 45 seconds. At these positions, the solution transmittances were previously measured and the suspending medium electron density calibrated. The measured scattering curve is an average over a range of solvent electron densities associated with the beam size. The momentum transfer  $q$  of the scattering curves was calculated using

$$q = \frac{4\pi E}{hc} \sin \theta, \quad (3.4)$$

where  $\theta$  is half of the scattering angle,  $h$  is the Planck constant and  $c$  is the speed of light. The incident photon energy  $E = (8800.0 \pm 0.8)$  eV was chosen to be higher than the photon energy for the transmission measurements to improve the recorded statistics, due to a ca. 150 higher transmission Henke *et al.* (1993). The scattered X-ray photons were collected with a vacuum-compatible Pilatus 1M hybrid-pixel detector (Dectris Ltd, (Baden, *Switzerland*)) with a pixel size of  $d = (172.1 \pm 0.2)$   $\mu\text{m}$  at a distance  $L = (4540.2 \pm 0.8)$  mm from the capillaries, determined by triangulation using a calibrated length measurement system Wernecke *et al.* (2014). The obtained scattering curve was normalized to the exposure time and the incident intensity, measured by means of a calibrated transparent silicon diode. In total, 40 scattering curves with different solvent electron densities were measured at two different times  $t_1 = 78$  min and  $t_2 = 156$  min after filling the capillaries.

### 3.6.1 Filling of capillaries

galden at bottom, reference layer

### 3.6.2 Calibration of solvent density and finding of main axis

The transmitted intensity through the sample is recorded at a photon energy of  $E = (5500.0 \pm 0.5)$  eV for 10 seconds at each position. The measurement consists of 20 points spaced 0.5 mm along the central vertical axis of the capillary. The overall X-ray transmission measurement requires approximately 5 minutes, which is within the calculated diffusion timescale of the aqueous sucrose solution. The solvent electron

density profile within the density gradient capillary derived from this measurement is depicted in figure **NO IMAGE CORRESPONDING TO THIS MEASUREMENT HAS BEEN ADDED**. A uniform thickness of the capillary within 0.5 % along this axis was determined by measuring the X-ray transmission of an empty capillary. The associated uncertainty in the sample transmission measurement is below 4 %. The sample thickness is assumed to be constant. This transmission measurement is performed both immediately before and after recording the scattering patterns, which takes 15 minutes to complete. The transmittance values used for the density calibration are then linearly interpolated between both data sets taking into account the time-dependence. These values can be converted to solvent electron densities via the Beer-Lambert law, which relates the density of the solution with the transmitted intensity:

$$\rho(z) = A (\ln I_0 - \ln I(z)). \quad (3.5)$$

Here  $\rho$  is the electron density of the suspending medium,  $I$  and  $I_0$  are the transmitted and incoming intensities respectively and  $A$  is a factor determined by the reference values of the solvent electron density at the vertical limits of the capillary at the initial time. The sucrose concentration in solution expressed as the mass fraction  $M$  at these reference points can be converted to electron densities with the empirical formula  $\rho = 1.2681M + 333.19 \text{ nm}^{-3}$  (Haynes 2012). The suspending medium electron density shows a maximum uncertainty of  $1 \text{ nm}^{-3}$  associated with the vertical size of the focused X-ray beam.

X-ray transmission measurements at the aqueous sucrose gradient were performed at a lower incident photon energy  $E = 5500 \text{ eV}$  to increase the transmittance differences for the less absorbing sucrose solution by a factor of 5.

### 3.6.3 Limitations

#### Density range

sucrose, fructose, iodixanol

#### Challenges with different contrast agents

Background subtraction, induced aggregation by heavy salts

#### Comparison to other contrast variation scattering techniques

SANS (deuterated water) RSoXS in polymeric colloids (H.Abe 2006), Carbon K-edge

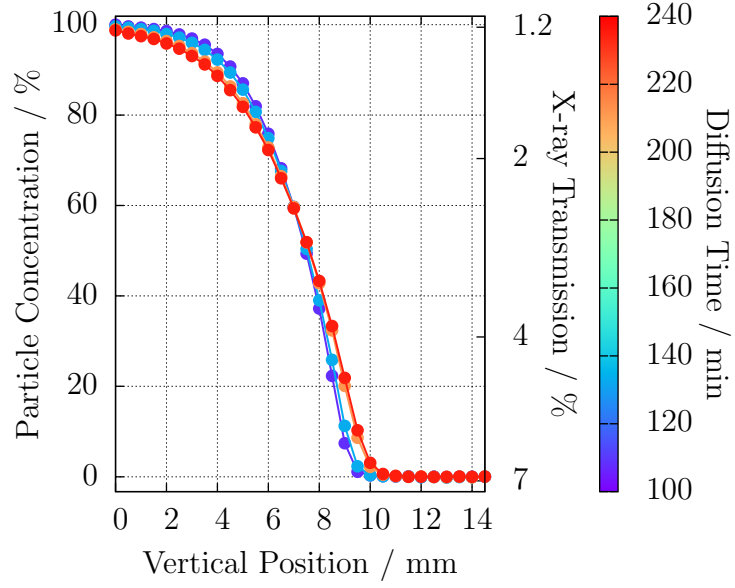


Figure 3.8: Typical measurement of particles with different diffusion timescale: Sucrose (with Kisker NPs) measured at 5500 eV and Colloids (Ludox HS40) measured at 8000eV

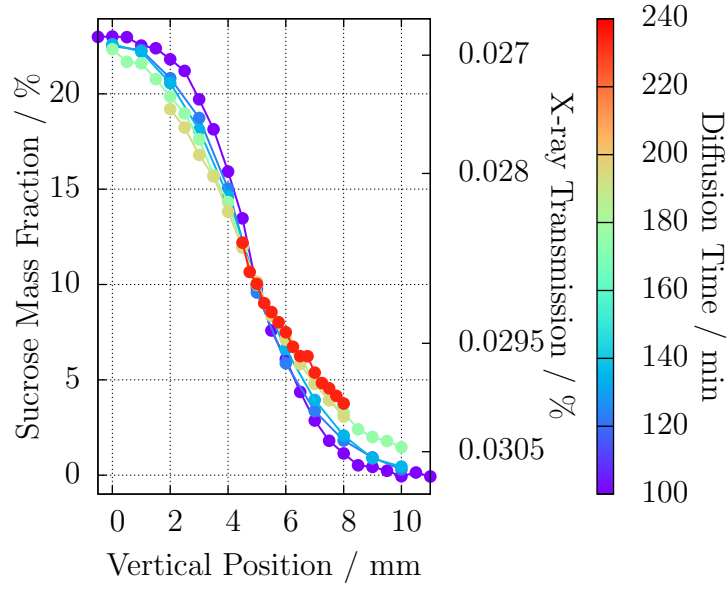


Figure 3.9: Typical measurement of particles with different diffusion timescale: Sucrose (with Kisker NPs) measured at 5500 eV and Colloids (Ludox HS40) measured at 8000eV

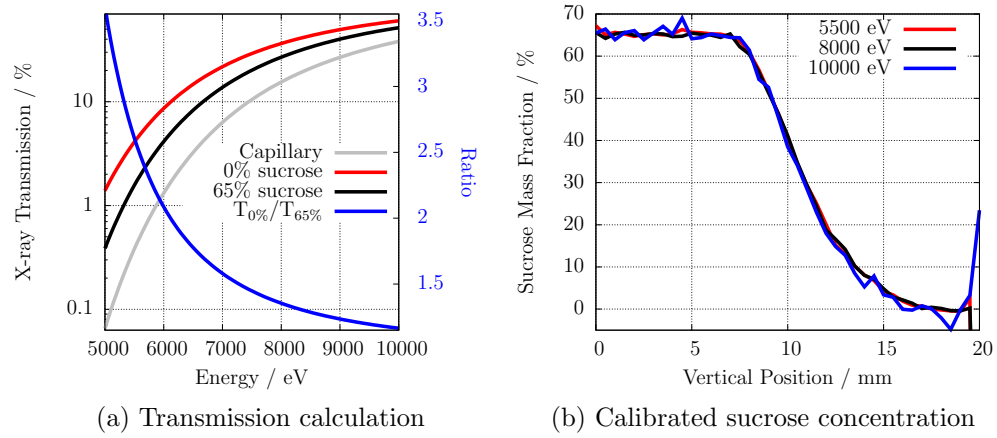


Figure 3.10: Statistics in the transmission measurement depending on the incoming energy. For lower energies, the transmission differences are larger and hence the statistics better. This was measured using only aqueous sucrose 65% in plain water (no colloids on it) Nov 2014

## Chapter 4

# Contrast variation in SAXS with the density gradient technique

The morphology of nanoparticles determines the properties necessary for their utilization in real-world applications. For instance, in drug delivery devices the phenomena involved in biocompatibility reactions (e.g. protein adsorption) depend on the amount of available surface and the nanoparticles' properties Vittaz *et al.* (1996). Particularly, polymer lattices and biodegradable nanoparticles have been of growing importance of late as drug carriers Kattan *et al.* (1992) and thus extensively characterized Soppimath *et al.* (2001). The size determination and the characterization of the radial structure of the particles are therefore fundamental tasks.

The contrast variation method in Small Angle X-ray Scattering (SAXS) experiments consists in systematically varying the electron density of the dispersing media to study the different contributions to the scattering intensity in greater detail as compared to measurements at a single contrast. It emerges as an ideally suited technique to elucidate the structure of particles with a complicated inner composition and has been repeatedly employed to investigate the radial structure of latex particles suspended in an aqueous medium Dingenouts *et al.* (1999); Ballauff (2011). In Small Angle Neutron Scattering (SANS) the contrast variation technique is widely used by mixing water and deuterium oxide, but the use of deuterated chemicals and the incoherent contribution to the background as well as the limited access to neutrons restrict the application of this technique. Other methods for structural investigation (e.g. transmission electron microscopy Joensson *et al.* (1991); Silverstein *et al.* (1989)) require prior treatment of the sample and are not ensemble averaged.

In SAXS, the solvent contrast variation technique is achieved by adding a suitable contrast agent to the suspending medium (e.g. sucrose) and recording the scattering

data as a function of the adjusted solvent electron density  $\rho_{solv}$  Ballauff (2001); Bolze *et al.* (2003). In order to resolve small changes of the radial structure, the average electron density of the colloidal particles must be close to the dispersant's, i.e., the *match point* should be approached, where the average contrast of the particle vanishes. In the case of polymeric lattices with electron densities ranging from 335 to 390 nm<sup>-3</sup>, an aqueous sucrose solution is very well suited as the suspension medium, due to the easy realization of concentrated solutions with electron densities of up to 400 nm<sup>-3</sup>. Previous studies on globular solutes Kawaguchi & Hamanaka (1992) and the influence of the sucrose on the size distribution of vesicles Kiselev *et al.* (2001a) show the feasibility of this technique, while further studies have investigated the effect of the penetration of the solvent into the particles Kawaguchi (1993).

The preparation of a number of different sucrose solutions has been a major inconvenience in solvent contrast variation experiments, due to the tedious, time-consuming process, possible inaccuracy in the sucrose concentration and the discrete range of available solvent electron densities. In this article we propose a novel approach using a density gradient column, which allows the tuning of the solvent contrast within the provided density range, resulting in a virtually continuous solvent contrast variation. By filling the bottom part of the capillary with a particle dispersion in a concentrated sucrose solution and the top part with an aqueous solution of the same particle concentration, a solvent density gradient is initiated with a constant concentration of nanoparticles along the capillary. Density gradient columns are extensively used in fields like marine biology Coombs (1981) or biochemistry together with centrifugation Hinton & Dobrota (1978), to create a continuously graded aqueous sucrose solution by diffusion of the sucrose molecules. Combining this approach with SAXS, it is possible to choose *in situ* the most appropriate solvent densities to perform measurements close to the contrast match point and to acquire extensive datasets in a short interval of time through the high brilliance and collimation of current synchrotron radiation sources. These datasets can be analysed using different, complementary evaluation methods. In this article, both a model-free theoretical framework as well as model fit are applied and, in combination, deliver a detailed insight into the inner structure of particles.

In order to demonstrate the proposed technique, latex nanoparticles with a core-shell structure were measured. The particles have a narrow size distribution and consist of a spherical polystyrene (PS) core enclosed by a thin shell of a denser polymer, most likely poly(methyl methacrylate) (PMMA). This is presented according to the following structure.

Firstly in § **THEORY CHAPTER**, the underlying theory of SAXS contrast variation is briefly reviewed and the scattering form factor used for the model fitting is

presented. The details of the experimental data acquisition are shown in § **EXPERIMENTAL CHAPTER**, followed by SAXS data evaluation using different methods in §4.2, jointly with a discussion of the experimental measurements and a consistency check of the obtained results. Finally, in §4.5 the experimental results of the particle size distribution and radial structure are summarized and the applicability of the solvent contrast variation technique in SAXS is discussed.

## 4.1 Materials and Methods

The preparation of a polymeric nanoparticle suspension density gradient within a glass capillary using an aqueous sucrose solution, the X-ray transmittance measurements at different positions along its vertical axis and the collection of scattering patterns at the calibrated capillary positions with distinct contrasts are described in the following sections.

### 4.1.1 Particles and chemicals

Carboxylated polystyrene nanoparticles with a nominal size of 105 nm suspended in water were purchased from Kisker Biotech (Steinfurt, *Germany*). The synthesis by multi-addition emulsion polymerization suggests that the assumption made in §**GUINIER SECTION WHEN DESCRIBING THE POLYDISPERSITY IN THE FORMULA** is correct and the average density of the particle is not altered by the size polydispersity.

### 4.1.2 Diffusion time and calibration height

The solvent density gradient was prepared in vacuum-proof borosilicate glass capillaries from Hilgenberg (Malsfeld, *Germany*) with a rectangular cross section of  $(4.2 \pm 0.2) \times (1.25 \pm 0.05)$  mm<sup>2</sup>, a length of  $(80 \pm 0.5)$  mm and a wall thickness of ca. 120  $\mu$ m. The bottom end of the capillary was closed by welding and the lower section, up to a height of ca. 1 cm, was filled with Galden®PFPE SV90 from Solvay Plastics (Brussels, *Belgium*). This fluid has an exceptionally high density of 1.69 g/cm<sup>3</sup>, low viscosity and is immiscible with aqueous solutions. Consequently, a uniform interface with the particle suspension is formed at the bottom.

Directly above the Galden fluid, the denser of two mixtures with different solvent densities and an equal particle concentration of 12.6 mg/ml was filled into the capillary using a syringe up to a height of 9 mm. The dense aqueous solution was prepared with 21.23 % sucrose mass fraction (Sigma-Aldrich (Missouri, *USA*)) with



a physical density of  $\rho_1 = 1.088 \text{ g/cm}^3$ , whereas a lighter one was produced without sucrose ( $\rho_2 = 0.997 \text{ g/cm}^3$ ). The light mixture was then filled on top of the aqueous sucrose solution along ca. 8 mm. By the time the two components come into contact, the density gradient is started with density values  $\rho_1$  and  $\rho_2$ , a total gradient length  $L = 17 \text{ mm}$  and the interface position at  $z_0 = 9 \text{ mm}$ . The calculated diffusion timescale of the solvent density gradient is ca. 10 minutes, considering the diffusion coefficient  $D = 5.2 \cdot 10^{-10} \frac{\text{m}^2}{\text{s}}$  Uedaira & Uedaira (1985); Ribeiro *et al.* (2006) and assuming that convection effects are negligible due to the small length-scale of the capillary Berberan-Santos *et al.* (1997). The time needed for the transfer of the sample into the high vacuum chamber amounts to ca. 1 hour. Within this time duration, the deviation of the solvent density at both ends of the gradient from the initial value can be estimated with an uncertainty below 0.5 %. If the same capillary is measured at different points in time during the diffusion process of the sucrose, several data sets with different solvent densities can be recorded and a very dense data set with a virtually continuous variation in the suspending medium density can be achieved.

## 4.2 Continuous contrast variation in SAXS on PS-COOH colloids

The measured scattering curves of the polystyrene particles are displayed in figure 4.1. In the region for  $q$  from  $0.03 \text{ nm}^{-1}$  to  $0.5 \text{ nm}^{-1}$  it is possible to observe the variation of the curve features corresponding to the particle form factor through the increase of the solvent electron density from  $333.7 \text{ nm}^{-3}$  at the top edge of the density gradient to  $360.3 \text{ nm}^{-3}$  at the maximum sucrose concentration. In this region, the experimental background is composed mainly by the contribution of the capillary scattering at the low  $q$ -region and the uniform scattering of the suspending medium. The experimental background scattering varies for different sucrose concentrations, but their variations are small and the background remains one order of magnitude below the sample scattering in the relevant Fourier region.

Upon increasing the solvent density, the position of the first minimum shifts from  $0.07 \text{ nm}^{-1}$  towards smaller  $q$ -values until it vanishes when the solvent electron density matches the average electron density of the measured particle. In the Fourier region of the scattering curves, several minima are observed which shift towards smaller  $q$ -values when increasing the solvent electron density. Upon subtracting the experimental background from the scattering curve, a decrease of the scattering intensity towards  $q = 0$  is observed only for the solvent electron density closest to

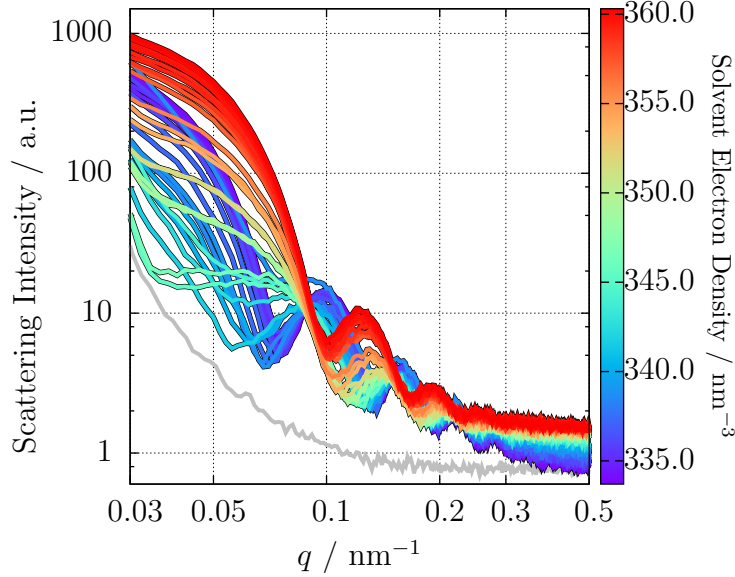


Figure 4.1: Experimental scattering curves of polystyrene nanoparticles (Kisker) for different suspending medium electron densities measured between 78 and 93 minutes after the inception of the density gradient. The dashed line shows the experimental background, containing scattering contributions from the capillary and the pure solvent.

the match point as depicted in figure 4.2. Therefore, background corrections can be neglected for systems with relatively high scattering power like in this study. For low-scatterers, an accurate background correction by measuring the pure suspending medium at different sucrose concentrations might be required. The behaviour at low  $q$ -values will be further discussed in section §4.4.2 when evaluating the zero-angle intensity.

The presence of the clearly visible isoscattering point around  $q = 0.09 \text{ nm}^{-1}$  confirms the existence of an inner structure. This heterogeneous composition was previously reported for the same colloids by Minelli *et al.* (2014), who observed methacrylic acid (MAA) and methylmethacrylate (MMA) at the particle surface, both monomer precursors of PMMA polymerization. A more detailed insight into the radial morphology is presented subsequently, using the theoretical framework already introduced.

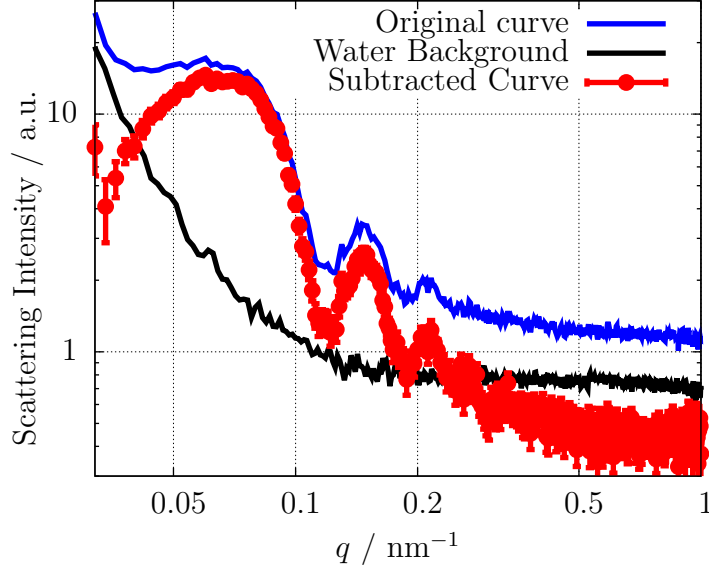


Figure 4.2: The thick red line shows the scattering curve measured at  $\rho_{solv} = 345.4 \text{ nm}^{-3}$ , close to the match point, and the dotted line displays the experimental background. The symbols with errorbars show the background corrected scattering curve.

## 4.3 Model dependent evaluation

### 4.3.1 Core-shell form factor fit

A core-shell model fit to the scattering curves is displayed in figure 4.3 for three representative contrasts. The model represents a radially symmetric particle, with a sharp interface between the outer shell and the inner core. This is a specific case of equation (2.2) with  $n = 2$

$$F_{CS}(q, R, R_{core}) = \Delta\eta f_{sph}(q, R) + \Delta\rho [f_{sph}(q, R) - f_{sph}(q, R_{core})], \quad (4.1)$$

where  $R$  and  $R_{core}$  are the outer shell and inner core radii respectively and the excess of electron density is  $\Delta\rho = \rho_{shell} - \rho_{core}$ . The simultaneous fitting of the form factor to the 40 measured scattering curves was performed by means of the method of least squares in the Fourier region Pedersen (1997). The calculated scattered intensity was modelled as the sum of the particle contributions and a two-component background  $I_{bg} = C_0 + C_4 q^{-\gamma}$ . The parameters  $\rho_{core}$ ,  $\rho_{shell}$ ,  $R$ ,  $R_{core}$  and  $\gamma$  were fitted simultaneously for all curves, whilst  $C_0$  and  $C_4$  were adjusted independently for each solvent density. A Gaussian size distribution was assumed. For the suspending

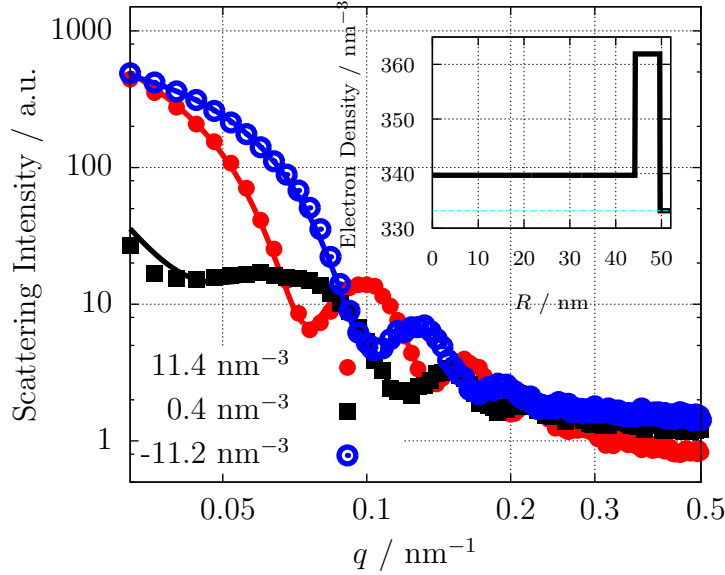


Figure 4.3: The simulated scattering curves from the core-shell model fit at three selected contrasts  $\rho_0 - \rho_{solv}$  are shown as lines together with the experimental data points. In the inset, the electron density profile corresponding to the fitted core-shell form factor is displayed.

medium electron density  $\rho_{solv}$  appearing in the contrast  $\Delta\eta$ , the value determined from the transmission measurement was used for each curve.

The obtained results are  $R = (49.7 \pm 2.8)$  nm,  $R_{core} = (44.2 \pm 0.9)$  nm,  $\rho_{core} = (339.7 \pm 0.1)$  nm<sup>-3</sup> and  $\rho_{shell} = (361.9 \pm 2.0)$  nm<sup>-3</sup>, which represent the radial structure of a dense, thin shell surrounding a lighter core, as seen in the inset of figure 4.3. The resulting average electron density of the particle is  $\rho_0 = (345.9 \pm 1.5)$  nm<sup>-3</sup> and the polydispersity degree,  $p_d = (22.8 \pm 6.0)$  %. The best fitting background corresponds to a value of  $\gamma = 4.3 \pm 0.5$ , close to the case  $\gamma = 4$  originating from large impurities or precipitates Pedersen (1994). The fit uncertainty was calculated with a confidence interval of one standard deviation.

It is noticeable that the calculated electron density of the core coincides exactly with the theoretical polystyrene electron density, although the electron density of the shell is remarkably lower than the theoretical value of 383.4 nm<sup>-3</sup> for PMMA Ballauff (2001). This might arise from the lower density of the monomers used in the particle synthesis (MAA and MMA), which could have mixed with the styrene monomers resulting in a less dense material than PMMA. This model might present some differences with the real colloid system, as a diffusive interfacial layer can be expected between polymer phases in colloids Dingenouts *et al.* (1994a), especially for

Table 4.1: Experimentally determined position of the first five isoscattering points and the corresponding external particle radius  $R$ .

	$q^*$ (nm <sup>-1</sup> )	$R$ (nm)
$q_1^*$	0.0900	49.9
$q_2^*$	0.1516	51.0
$q_3^*$	0.2267	48.1
$q_4^*$	0.2822	49.9
$q_5^*$	0.3421	50.3

incompatible polymers such as PMMA and PS. On the other hand, the large quantity of scattering curves used for the fitting process and, accordingly, the decreased uncertainty suggests that the chosen sharp core-shell model has a great resemblance to the real particle.

## 4.4 Model-free approach to contrast variation data

### 4.4.1 Isoscattering point

#### Quantification: Relative standard deviation

The first isoscattering point is clearly visible in figure 4.1. For a more quantitative evaluation, the relative standard deviation of the 40 measured curves at each  $q$  is calculated according to

$$\sigma_r(q) = \frac{1}{\bar{I}(q)} \sqrt{\frac{\sum_{i=1}^M (I_i(q) - \bar{I}(q))^2}{M - 1}}, \quad (4.2)$$

where  $\bar{I}(q)$  is the mean value of the intensity at  $q$  and  $M$  is the number of scattering curves. This value becomes minimal at an isoscattering point. In order to reduce the influence of outliers, a truncated mean value was utilized, disregarding the 10 % most dispersed data points. In figure 4.4, the relative standard deviation is plotted as a function of the momentum transfer  $q$ , which shows several distinguishable minima corresponding to isoscattering points.

A precise determination of the isoscattering point positions is performed by fitting Lorentzian functions to the minima in the relative standard deviation plot, which allows the calculation of the model-free external radius of the particle by means of equation (2.6). The results are presented in table 4.1. The obtained particle radii vary in the range from 48.1 nm to 51.0 nm, although as predicted by Kawaguchi

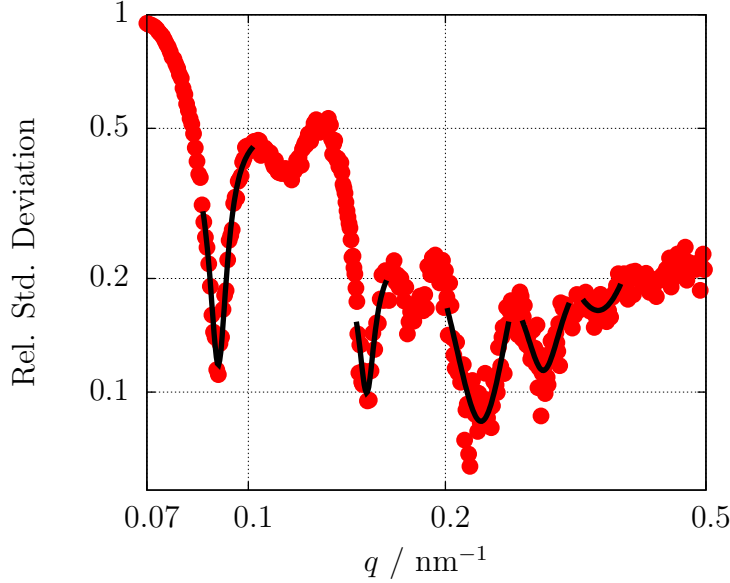


Figure 4.4: Relative standard deviation of the scattering curves as a function of the momentum transfer. The labelled minima correspond to the first five isoscattering point positions calculated by fitting a Lorentzian function (red line).

& Hamanaka (1992) for a polydisperse system, the isoscattering points get smeared out for larger  $q$ -values and the precision decreases, simultaneously with the increase of the solvent background at higher  $q$ -values. This can be directly observed in the quality of the experimental data, as the first two minima are clearly pronounced, while the subsequent minima appear smeared out. For instance, the isoscattering point  $q_5^*$  is already too weak for an accurate evaluation and the third minimum shows two remarkably close smaller minima which might affect the shape of the function. Therefore,  $q_1^*$  and  $q_2^*$  yield the most reliable values for evaluating the external radius of the particles, although all results are presented in table 4.1. The value derived from the isoscattering points  $R = 50.5$  nm differs by only 1.6 % from the radius calculated from the model fit in the previous section.

Due to the ambiguous definition of the isoscattering point diffuseness, a quantitative determination of the polydispersity of the suspended nanoparticles by means of the Lorentzian profile is rather challenging. Nevertheless, the narrow size distribution of the sample becomes clear by comparing the relative standard deviation values of the observed minima in figure 4.4 with a simulation using the structural parameters obtained in section §4.3.1. The value  $\sigma_r(q_1^*) = 0.11$  corresponds to a calculated ensemble polydispersity of 24 %. This value serves as an upper  $p_d$  limit due to

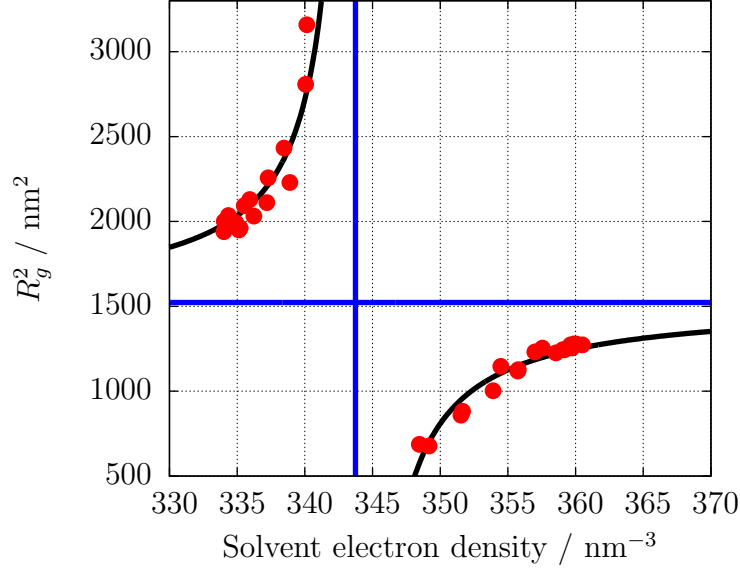


Figure 4.5: Experimental squared radius of gyration as a function of the solvent electron density. Equation (6) is fitted to the data and shown as a thick line. The vertical and horizontal asymptotes correspond to  $\rho_0$  and  $\tilde{R}_{g,c}^2$  respectively.

the possible overestimation caused by the scattering contribution of the suspending medium.

#### 4.4.2 Guinier region

By analyzing the low  $q$ -region of the scattering curves, the so-called Guinier region, two important parameters can be obtained: the radius of gyration  $R_g$  and the intensity at zero angle  $I(0)$ . According to Feigin & Svergun (1987), the fit of equation (2.8) to the Guinier region is mainly valid up to  $qR_g < 1.3$ . In this restricted  $q$ -range, too few data points are available for a reliable data analysis. Therefore, an extrapolation using the spherical form factor  $f_{sph}(q, R)$  over the range available before the first minimum has been employed instead to obtain  $R_g$  and  $I(0)$ .

As described in §**GUINIER THEORY CHAPTER**, the radius of gyration of a heterogeneous particle in a contrast variation experiment should behave according to equation (2.9). In figure 4.5, the experimental squared radius of gyration is displayed as a function of the suspending medium electron density. The best fit to the measured data with values  $\rho_0 = 343.7 \text{ nm}^{-3}$ ,  $\tilde{R}_{g,c} = 39.0 \text{ nm}$ ,  $\tilde{\alpha} = 4470 \text{ nm}^{-1}$  and  $\tilde{\beta} = 0 \text{ nm}^{-4}$  is shown by the solid line.

The positive value of  $\tilde{\alpha}$  validates the hypothesis that a more dense polymer (probably PMMA) surrounds a lighter core (PS) Stuhrmann (2008). The calculated average electron density of the particle  $\rho_0$  suggests a very thin layer of PMMA shell around the PS core, due to the proximity of its value to the polystyrene electron density ( $339.7 \text{ nm}^{-3}$ ). The value of  $\tilde{\beta} = 0$  proves a concentric model, where core and shell share the same centre. Using the same polydispersity value of 22.8 % obtained in the fitting process, the value for the particle shape radius of gyration results in  $R_{g,c} = 36.9 \text{ nm}$  and the external radius of the particle can be calculated assuming the particle as a spherical object ( $R_g^2 = \frac{3}{5}R^2$ ). This calculation gives  $R = 47.6 \text{ nm}$ , which is only 2.1 nm smaller than the calculated external radius  $R = 49.7 \text{ nm}$ , though it might be underestimated due to the choice of a possibly inflated polydispersity.

### Average electron density

Using the same set of 40 scattering curves, the behaviour of the zero-angle intensity under the contrast variation is also investigated by fitting equation (2.10) to the experimental  $I(0)$ , as depicted in figure 4.6. A minimum in the curve is observed at  $\rho_{solv} = 346.0 \text{ nm}^{-3}$ , which corresponds to the value of the average electron density of the particle. This value is in very good agreement with the result obtained by fitting the core-shell form factor. It is also noticeable that the minimum intensity is approximately 0, which means that the effective average density of the ensemble is equal to the average density of the particle Avdeev (2007). This result further legitimates the previously made assumption that the ratio between the particle components' volumes is constant independent of the polydispersity and hence  $\tilde{\rho}_0 = \rho_0$ .

First point Comparison of accuracy

Extrapolatio Using just the Guinier region or extrapolating from first minimum

## 4.5 Summary

Table 4.2 summarizes the results of all three presented methods. From the first two isoscattering points, values for the external radius and an upper bound to the polydispersity degree have been derived. Focusing on the Guinier region of the scattering curves, a value for the average electron density of the particles is found using the radius of gyration as well as the zero-angle intensity, the values of which differ by  $2.3 \text{ nm}^{-3}$ . By fitting a core-shell model, an external radius of  $R = 49.7 \text{ nm}$  and an average electron density  $\rho_0 = 345.9 \text{ nm}^{-3}$  have been obtained, which are in



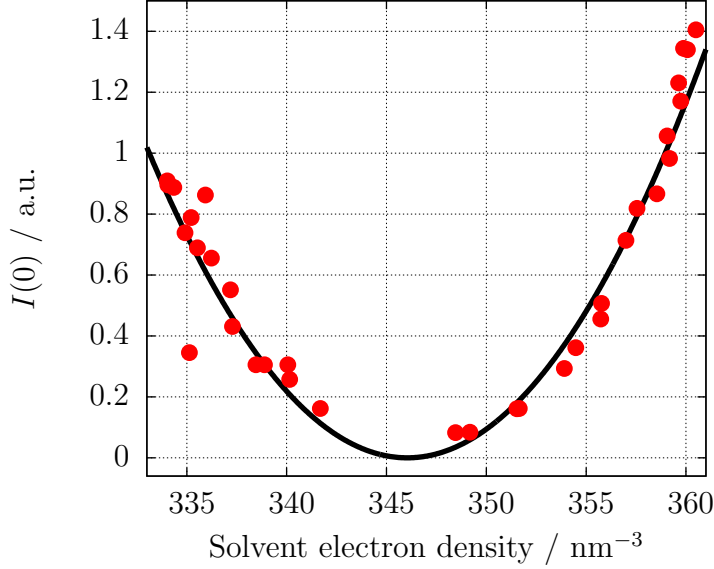


Figure 4.6: Experimental zero-angle intensity as a function of the solvent electron density. The function corresponding to equation (7) is fitted to the data and shown as a thick line. The minimum in the parabola corresponds to  $\rho_{solv} = \rho_0$ .

Table 4.2: Comparison of the different methods presented in this article to evaluate SAXS contrast variation data.

	$R$ (nm)	$\rho_0$ ( $\text{nm}^{-3}$ )	$p_d$ (%)
Core-shell fitting	$49.7 \pm 2.8$	$345.9 \pm 1.5$	$22.8 \pm 6.0$
Isoscattering point*	50.5	-	$< 24$
Radius of gyration	$47.6^{**}$	343.7	-
Zero-angle intensity	-	346.0	-

\*Mean value of  $q_1^*$  and  $q_2^*$

\*\*Using the polydispersity degree from the core-shell model fitting

considerable agreement with the previous results, i.e., the values determined by the other methods are included in their confidence ranges, except for the  $\rho_0$  calculated with the radii of gyration.

From these results, it is evident that the radius of gyration interpretation produces the most deviant values. This might be founded in the complicated function fitted to the data and the reduced availability of  $q$ -range employed to obtain  $R_g$ .

The resulting polydispersity degree of the measured particles from the model fit is in agreement with the upper limit obtained with the radii of gyration. Nevertheless

the polydispersity is the parameter determined with the largest uncertainty in the fitting process and therefore this result must be considered with care.

It can be concluded that the different approaches show consistent and complementary results about the size distribution of nanoparticles with radial inner structure, especially for the external radius of the particle and its average electron density. A precise value for the polydispersity degree could not be obtained as explained previously, although a credible upper limit to the polydispersity degree of 24 % could be given.

This article demonstrates that it is possible to perform continuous contrast variation for light nanoparticles by means of a density gradient and to collect a large quantity of SAXS curves, which can be analyzed with complementary approaches to reveal a consistent insight into the size distribution and the inner structure of the suspended nanoparticles.

By means of a model-free analysis of the experimental data based on the isoscattering point theory, an average particle diameter of 101 nm was obtained. The analysis of the Guinier region of the scattering curves shows that the radial inner structure of the particles consists of a thin, more dense layer coating the polystyrene core. Complementing these results, a core-shell model fit showed that the core component of the particle had exactly the same electron density expected for polystyrene and the shell was composed of a compound with a density below that of PMMA. This core-shell structure was expected for chemical reasons due to the different hydrophobicity of PS compared to MMA and MAA.

Considering the similar electronic composition of these polymers and the average electron density of the particle  $\rho_0 = 346 \text{ nm}^{-3}$ , an average physical density of the particles of  $\rho = 1.07 \text{ g/cm}^3$  can be calculated. The precision in the determination of this density proves this technique as a useful tool and an alternative to other techniques like isopycnic centrifugation Vauthier *et al.* (1999); Arnold *et al.* (2006); Sun *et al.* (2009), widely used with biomacromolecules.

Nevertheless, future applications of this technique must consider the limited density range accessible with an aqueous sucrose solution, which restricts the applicability to light particles. More dense solutions prepared with heavy salts could be used as an alternative, but they might compromise the stability of the particles and lead to more complicated handling of the sample due to a decreased diffusion timescale. Other possible methods that vary the contrast of a single medium have already been proposed (e.g. ASAXS Stuhrmann (2007)), although a system fulfilling the requirements must be found and a large complementary dataset might be difficult to acquire.

## Chapter 5

# Simultaneous size and density determination of polymeric colloids

In the continuously growing world of nanotechnology, nanoparticles have a pre-eminent position, employed as pharmaceutical or cosmetic products(Guterres *et al.* 2007) and especially in the emerging field of nanomedicine. Indeed, nanoparticles open exciting new possibilities in this field as platforms for drug-delivery(Wang *et al.* 2012) or encapsulating imaging agents(Tao *et al.* 2011). Nowadays, polymeric colloids and biodegradable nanocarriers are finding many research and medical applications(Vicent & Duncan 2006) and are starting to undergo clinical trials(Patel *et al.* 2012; Beija *et al.* 2012; Cabral & Kataoka 2014).

The current advances in nanomaterial development for medical applications are focused towards tailoring polymeric nano-drug carriers with flexible surface functionalisation and controlled morphologies(Euliss *et al.* 2006; Yang *et al.* 2005). Size and shape, combined with the choice of polymer and the mechanical properties, are fundamental and defining aspects of the particle functions, e.g. their *in-vivo* biodistribution(Vittaz *et al.* 1996; Mitragotri & Lahann 2009; Doshi & Mitragotri 2009) or their drug-delivery efficacy(Powers *et al.* 2006). Therefore, a full and consistent characterisation of all properties of nanoparticles is of crucial importance and must be carefully addressed.

The characterisation of polymeric nanoparticles remains a challenge due to their typically complicate internal structure(Beyer *et al.* 1990) and requires more than a single characterisation technique to detect these heterogenous compositions. For instance, electron microscopy is an effective tool for direct observation of the shape

and size distribution of nanoparticles, although it cannot conclusively elucidate their internal morphology.

The use of an ensemble-average and non-destructive technique such as small-angle X-ray scattering (SAXS) arises as an appropriate alternative (Leonard Jr *et al.* 1952; Motzkus 1959). SAXS can discern differences in the radial structure of polymeric colloids and offers advantages to other methods which require prior treatment of the sample and are not averaging (Silverstein *et al.* 1989; Joensson *et al.* 1991). Despite being a highly informative method for the accurate characterisation of polymeric particles, the difficulties in the interpretation of the scattering curves demands complementary experimental information (Mykhaylyk 2012).

The contrast variation method in SAXS varies systematically the electron density of the suspending medium by adding a suitable contrast agent, e.g. sucrose, in order to resolve the different contributions of the particle components to the scattering. By measuring SAXS patterns as a function of the adjusted contrast, a more detailed insight into the particle morphology can be obtained in comparison to single-contrast experiments (Bolze *et al.* 2004). For instance, the internal structure can be modelled in terms of the radial electron density (Dingenouts *et al.* 1994*b*, 1999; Ballauff 2011; Ballauff *et al.* 1996) and the individual contribution of each polymer can be distinguished (Beyer *et al.* 1990; Grunder *et al.* 1991, 1993; Ottewill *et al.* 1995; Bolze *et al.* 1997; Dingenouts *et al.* 1994*c*) as well as its density (Mykhaylyk *et al.* 2007).

The formation of a solvent density gradient within a capillary emerges as an intelligent strategy to measure SAXS patterns at a continuous range of contrasts and, as a result, collect in a relatively short timespan an extensive data set of complementary scattering curves (Garcia-Diez *et al.* 2015). The continuous contrast variation technique in SAXS is ideally suited for current synchrotron radiation sources, where high brilliance and collimation permit the measurement of the scattering curves within the diffusion time of the contrast agent.

This work demonstrates the simultaneous size and density determination using this technique with 3 polymeric particles of different sizes and polymeric species. By means of an aqueous sucrose density gradient, the measurements were achieved along a large range of suspending medium densities, from water density to that of poly(methyl methacrylate)'s, highlighting the relevance of the technique across a wide spectrum of polymers.

The article discusses the applicability of this method for the traceable size determination of these colloids, where a high-resolution size distribution of the particles is presented. Focusing on a low-density colloid, different evaluation approaches to SAXS contrast variation experiments are introduced and the advantages and drawbacks of a model-free formulation like the isoscattering point position are discussed,

together with the accuracy of the scattering shape factor.

In addition, a form factor model is fitted to the scattering curves to obtain decisive information about the internal morphology of the particle, which is not directly available by other techniques such as transmission scanning electron microscopy (TSEM), differential centrifugal sedimentation (DCS)(Fielding *et al.* 2012) or atomic force microscopy (AFM).

The ability of the continuous contrast variation technique to determine the density of polymeric colloids in suspension is also discussed. Normally, the density of the suspended particles can not be compared to the bulk density of the dry material. Such a complex question has been addressed by different methods, though with evident limitations. For example, the density of polymeric beads has been measured previously with field-flow fractionation (FFF) with high-accuracy but at the expense of *a priori* assumptions about the morphology of the particle(Giddings *et al.* 1981; Yang *et al.* 1983; Caldwell *et al.* 1986). Assuming the Stokes' diameter as the actual size of the colloid, recent advances in analytical ultracentrifugation allow the complementary characterisation of the size, density and molecular weight of gold nanoparticles(Carney *et al.* 2011).

The 3 polymeric colloids were also analysed by DCS and the results compared and discussed with those obtained by SAXS. DCS uses the sedimentation of particles through a density gradient to measure high resolution particle size distributions(Minelli *et al.* 2014). Its accuracy typically depends on the knowledge of the density of the particles. When the size of the particle is known, DCS can alternatively be used to measure average particle's density.

Neumann(Neumann *et al.* 2013) used two sucrose gradients resulting in different viscosities and densities, where the altered settling velocity combined with linear regression analysis was used for the calculation of the size and density of silica nanoparticles and viruses. Bell(Bell *et al.* 2012) adopted a two gradient method based on the variation of the sucrose concentration to determine the density of the Stöber silica and the calibration standards used in DCS.

In this study, the size and density of low-density particles is independently determined by performing DCS measurements with two different discs using the sedimentation and flotation respectively of the particles through a density gradient and solving the relative Stokes' equations.

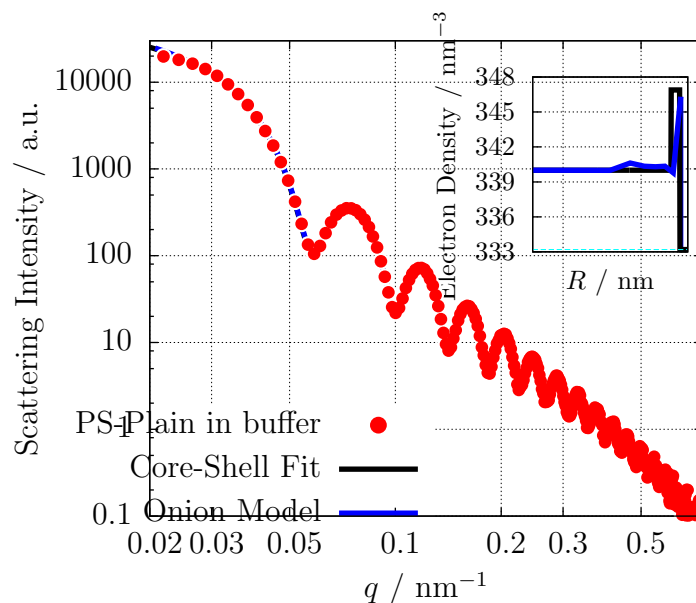


Figure 5.1: Scattering curve of PS-Plain in buffer. A core-shell and onion model fit to the experimental scattering curve are presented. In the inset, the electron density radial profile of these fits is shown, assuming the core is polystyrene with a density of  $339.7 \text{ nm}^{-3}$ .

## 5.1 Materials and methods

### 5.1.1 Particles and chemicals

Carboxylated polystyrene nanoparticles (PS-COOH) synthesized by multi-addition emulsion polymerization with a nominal size of 105 nm were purchased from Kisker Biotech (Steinfurt, Germany). Carboxylated poly(methyl methacrylate) colloids (PMMA-COOH) with a nominal diameter of 187 nm and plain polystyrene particles (PS-Plain) polymerized with  $< 1 \text{ wt\%}$  of a surface-active co-monomer with a nominal diameter of 147 nm were purchased from Microparticles (Berlin, Germany). Galden® PFPE SV90 was purchased from Solvay Plastics (Brussels, Belgium).

In figure 5.1, the SAXS curve of the PS-Plain particles in buffer at a single-contrast is shown. The large number of minima observed in the curve is remarkable and indicates the high monodispersity of the sample, which allows a traceable size determination of these colloids.

Upon trying different form factor fits detailed in the **Supplementary Information (SI)**, a simple core-shell structure with a sharp interface was found to be

Table 5.1: Parameters of the different DCS setups: composition of the sucrose gradients, average density of the gradients  $\rho_f$ , angular speed of the centrifuge  $\Omega$  and type of calibrant.

	Sucrose concentration (w/w)	$\rho_f$ (g cm <sup>-3</sup> )	$\Omega$ (rpm)	Calibrant
PS-COOH	from 2 % to 8 % in H <sub>2</sub> O	1.013	$2.0 \cdot 10^4$	A
PMMA-COOH	from 4 % to 12 % in H <sub>2</sub> O	1.025	$2.0 \cdot 10^4$	B
PS-Plain	from 2 % to 8 % in H <sub>2</sub> O	1.013	$2.4 \cdot 10^4$	B
PS-Plain*	from 4 % to 12 % in D <sub>2</sub> O	1.140	$2.4 \cdot 10^4$	C

\*Low density disc

the most suitable, suggesting a heterogeneous structure which is eluded by other characterization techniques, e.g. microscopy. The obtained particle diameter was  $(147.0 \pm 4.7)$  nm, where the fit uncertainty was calculated with a confidence level of one standard deviation ( $k = 1$ ) by examining the change in  $\chi^2$  when varying the diameter. The radial electron density profile of the core-shell fit is shown in the inset of figure 5.1, where a thin shell with high density surrounds a lighter core. This structure is likely due to the non-reacted monomers in the main matrix or the highly hydrophilic behaviour of the co-monomer, segregating polystyrene to the core.

### 5.1.2 Differential Centrifuge Sedimentation (DCS)

DCS measurements were performed with a CPS DC20000 instrument (CPS Instruments, Prairieville, LA, USA) upgraded to DC24000 for the PS-Plain measurements. The radial position of the detector was measured by injecting 100  $\mu$ L aliquots of water into the spinning disc initially empty until the accumulation of water produced a response in the detector. For the density gradient formation, the disc was filled with 14.4 mL of a sucrose (Amresco LLC, OH, USA) solution topped with 0.5 mL of dodecane to prevent evaporation. The detailed information of the gradients is summarised in table 5.1.

The measured turbidity at 405 nm was converted to the number of particles for each measured diameter by treating the particles as spherical Mie scatterers with no optical absorbance at the incident wavelength. Three different types of calibration particles were used: poly(vinyl chloride) colloids in water with density of 1.385 g cm<sup>-3</sup> and nominal size of  $(223 \pm 5)$  nm (calibrant A) and  $(239 \pm 5)$  nm (calibrant B) and polybutadiene colloids in 16 % sucrose mass fraction in heavy water with nominal size of  $(510 \pm 20)$  nm and density of 0.91 g cm<sup>-3</sup> (calibrant C). A standard disc configuration where the particles sediment through a lower density gradient

was used and additionally, a more recently developed set up which makes use of a disc where colloids float through a higher density gradient was also used for PS-Plain due to their low density (Fitzpatrick 1998). Measurements of PS-COOH and PMMA-COOH at 0.05 % w/v concentration were performed in triplicate. PS-Plain measurements were repeated seven times for each setup. Injection volumes were 100  $\mu\text{L}$ . Measurement uncertainties include both statistical and systematic uncertainty propagated from Stokes' equations.

### Stokes equations

The equation for the DCS is derived from the Stokes' law for a spherical particle of diameter  $D_p$  and density  $\rho_p$ :

$$D_p = \sqrt{\frac{18\eta \ln \frac{R}{R_0}}{(\rho_p - \rho_f) \omega^2 t_p}} \quad (5.1)$$

where  $t_p$  is the sedimentation time between radii  $R$  and  $R_0$  of the particle,  $\eta$  and  $\rho_f$  are the viscosity and the density of the fluid respectively and  $\omega$  is the disc angular frequency.

Before every sample measurement, a calibrant of known size  $D_c$  and density  $\rho_c$  is measured with the same set up for which the Stokes' law is also valid and can be expressed as:

$$D_p = D_c \sqrt{\frac{(\rho_c - \rho_f) t_c}{(\rho_p - \rho_f) t_p}} \quad (5.2)$$

### Combined analysis

When performing the measurements using two fluids, one with density  $\rho_L$  and one with higher density  $\rho_H$  (employed typically for lower density particles), one needs to solve the set of equations

$$D_p = D_{cH} \sqrt{\frac{(\rho_{cH} - \rho_H) t_{cH}}{(\rho_p - \rho_H) t_{pH}}} \quad (5.3)$$

$$D_p = D_{cL} \sqrt{\frac{(\rho_{cL} - \rho_L) t_{cL}}{(\rho_p - \rho_L) t_{pL}}} \quad (5.4)$$



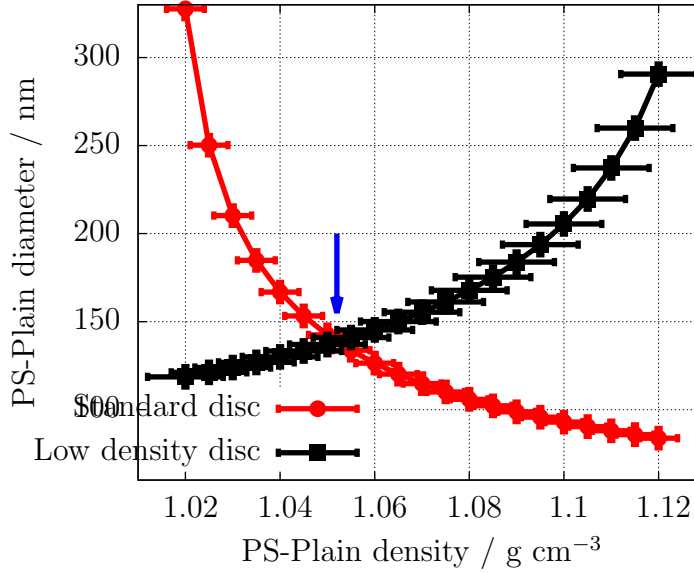


Figure 5.2: Dependence of the intensity-based modal Stokes' diameter on the particle density for PS-Plain particles analyzed in  $\text{H}_2\text{O}$ -sucrose (black) and  $\text{D}_2\text{O}$ -sucrose (red) gradients. The grey arrow indicates the crossing point of the data, which occurs for a diameter of  $(138.8 \pm 5.8)$  nm and a density of  $(1.052 \pm 0.010)$   $\text{g cm}^{-3}$

where  $cH$  and  $cL$  denote the calibrants used with high and low density fluids respectively and  $t_{pH}$  and  $t_{pL}$  are the sedimentation times of the particles measured in the high and low density fluids respectively.

The values of  $D_p$  and  $\rho_p$  which satisfy equations 5.3 and 5.4 can be found analytically or graphically. As depicted in figure 5.2, the two setups measure the same size and density of the colloid at the crossing point.

## 5.2 Technique validation for the determination of the particle size distribution

The morphology was further studied using the density gradient contrast variation technique described in §3 by varying the suspending medium electron density from 333.2 to 350.2  $\text{nm}^{-3}$ . By increasing the solvent contrast, the changes of the features in the scattering curves presented in figure 5.3a and the appearance of isoscattering points prove the multi-component composition of this colloid.

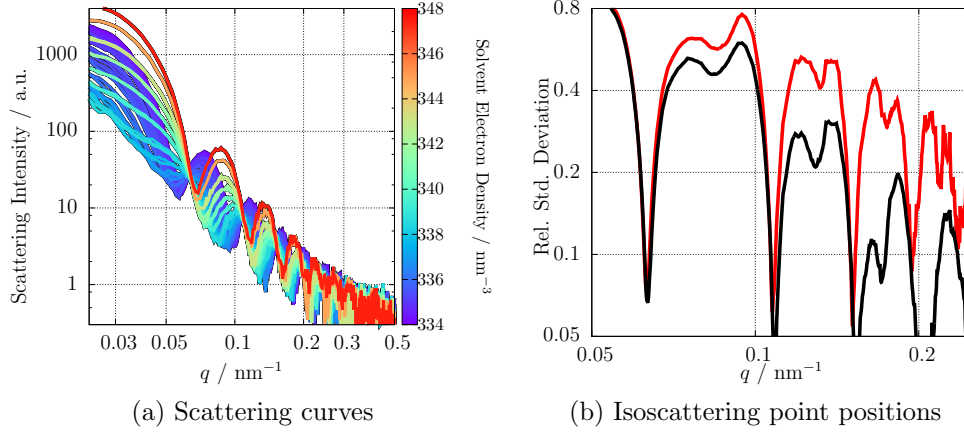


Figure 5.3: SAXS curves of PS-Plain obtained by density gradient contrast variation after solvent background subtraction. The inset shows the relative standard deviation calculated from all the scattering curves, where the minima correspond to the isoscattering points  $I_i$ .

From the 40 experimental scattering curves shown in figure 5.3a, a model-free size determination can be performed by locating the isoscattering points  $I_i$ , which are related to the radius  $R$  of the particle by  $\tan(q^*R) = q^*R$  (Kawaguchi *et al.* 1983).

The quantification of the isoscattering points positions  $q_i^*$  was performed by calculating the relative standard deviation of each  $q$  value across all the measured curves, as shown in the inset of figure 5.3a where the minima correspond to the fulfillment of the isoscattering condition.

The particle sizes obtained from the first 4 isoscattering points ( $I_1$  to  $I_4$ ) range between 142.4 and 144.4 nm, showing a good agreement for higher  $q$ -values as well. The precision of the isoscattering point positioning decreases for increasing  $q$  as demonstrated by Kawaguchi (Kawaguchi & Hamanaka 1992) and it is exemplified by the broadening of the minima for higher  $q$ .

The data can also be analyzed by using the so-called *shape factor* or *resonant term* which can be derived from the *basic functions* approach (Stuhrmann & Kirste 1965, 1967) described in the **SI**. The shape factor is defined by the scattering corresponding to the particle components impenetrable to the solvent, e.g. the external shape of the particle independently of its inner structure.

This approach is appropriate for many polymeric particles with a heterogenous morphology (Bolze *et al.* 2004), such as the PS-Plain colloid, because it enables the size distribution determination of the particles avoiding any *a priori* consideration about the particle composition.

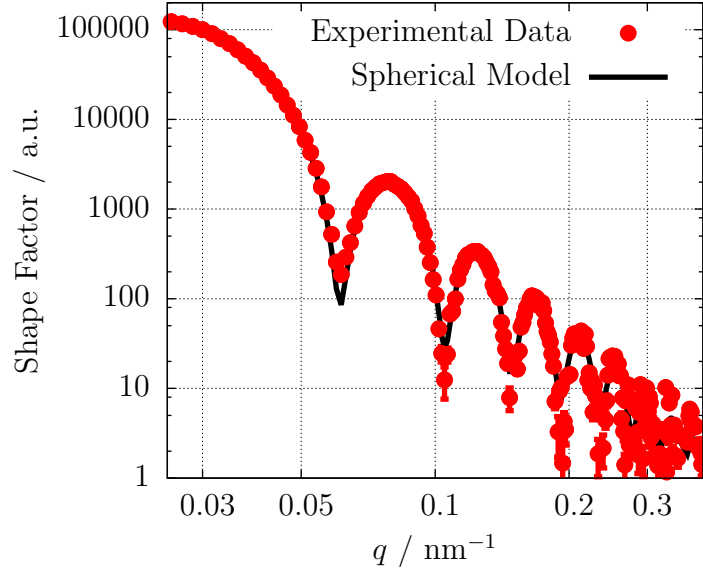


Figure 5.4: Experimental shape factor of the PS-Plain colloid calculated from 40 scattering curves and the spherical form factor fitted to the data.

The shape factor calculated from the measured scattering curves is depicted in figure 5.4 together with the spherical model fitted to the data, which employs a simple form factor that ignores the internal structure and a gaussian size distribution. From this fit, a mean particle size of  $(146.8 \pm 1.3)$  nm was determined. The fit uncertainty was determined as discussed before. By fitting an ellipsoid model to the shape factor, a sphericity of 98 % was obtained.

These results highlight the applicability of this technique for the characterization of the size and shape of polymeric colloids. Additionally, the associated uncertainty calculated with this approach is 3.5 times smaller than the one obtained with the single-contrast SAXS experiment.

### 5.2.1 Inter-laboratory comparison of the mean particle size

The improvement in the size accuracy with the shape factor approach is summarized in figure 5.5, where the size of the PS-Plain particles determined by different techniques in an inter-laboratory study is also presented (Nicolet *et al.* 2016).

The figure compares the PS-Plain size measured by the ensemble techniques SAXS and DCS and the imaging methods AFM and TSEM and presents the weighted

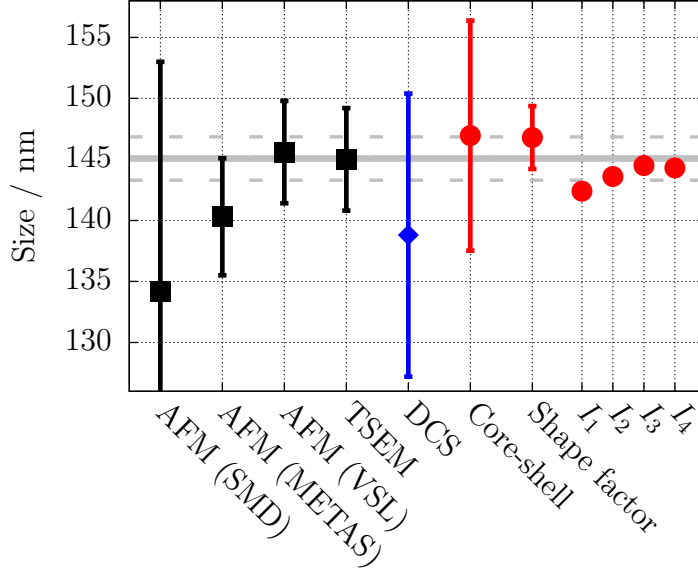


Figure 5.5: Comparison of the PS-Plain average size obtained with different techniques, where the errorbars correspond to the expanded uncertainty ( $k = 2$ ). The circles correspond to results obtained with SAXS and the diamonds to combined DCS measurements. The gray line defines the weighted mean of all the independent results.

mean value of all the independent results as a grey line, which corresponds to a diameter of 145.1 nm with an associated expanded uncertainty ( $k = 2$ ) of 1.8 nm. The SAXS results tend to larger values when modelling the scattering form factor, whilst the size obtained from the isoscattering points positions  $I_i$  present values slightly smaller than the calculated mean value. However, the maximum deviation from the weighted mean is less than 2 %.

The microscopy values are obtained from Belgian Service Métrologie-Metrologische Dienst (SMD), Swiss Federal Institute of Metrology (METAS) and Dutch Metrology Institute (VSL).

The DCS result is obtained by a combined analysis of two complementary centrifuge configurations as detailed in **SI**, where figure **S1** depicts the dependency of the measured particle size on the density values for the two setups. The two setups measure the same size and density at the crossing point of the data, which occurs for a diameter of  $(138.8 \pm 5.8)$  nm and a density of  $(1.052 \pm 0.010)$  g cm<sup>-3</sup>. The measured size fits within its uncertainty in the confidence interval of one standard deviation of the inter-laboratory comparison.

All the techniques are in very good agreement, even considering that they are

based on different physical principles. The improvement in accuracy for the size determination with SAXS by using the shape factor approach is further sustained by this comparison.

This improvement was confirmed by employing the same approach with the PS-COOH colloids. The size obtained from the core-shell model fit is  $(99.4 \pm 5.6)$  nm (Garcia-Diez *et al.* 2015), while the value obtained from the shape factor calculation is  $(101.4 \pm 2.4)$  nm. Again, the uncertainty associated to the size decreases by  $\sim 60$  %, whilst it is still in accordance with the size obtained with the isoscattering points positions of 101.0 nm with a standard deviation of 1.1 nm.

Due to the low polydispersity of the PMMA-COOH particles and their homogeneous composition, a spherical form factor fit to the single-contrast scattering curve provides already a very accurate size  $(186.5 \pm 2.3)$  nm. In this case, contrast variation experiments in SAXS show no advantages.

It has been demonstrated that the possibility to determine the particle size distribution by the scattering shape factor is a clear improvement to single-contrast SAXS techniques reducing relevantly the uncertainty, although an accurate determination of the contrast and a relatively high number of scattering curves are required.

Nevertheless, another contrast variation evaluation approach such as the isoscattering points presents as well certain assets which can not be ignored. For instance, the independence of  $q^*$  from the sample contrast facilitates its easy application. On the other hand, the diffuseness of the isoscattering point position due to the polydispersity and ellipticity of the sample (Kawaguchi & Hamanaka 1992) arises as an indisputable drawback.

## 5.2.2 Colloidal size distribution

An important attribute of polymeric colloids is their polydispersity, as the suitability for specific applications depends on their spread in size. For example, colloids are known to induce different inflammatory responses depending on their size (Kusaka *et al.* 2014). The polydispersity degree  $p_d$  is calculated as the full width at half-maximum of the number-weighted particle size distribution divided by its average value.

The SAXS results determine a  $p_d$  for the PS-Plain colloids of 6.1 %, which is an indicator of a very monodisperse distribution, as also suggested by the regular minima observed in figure 5.1. Particle polydispersities measured by DCS are also low as observed in figure 5.6, ranging from 7.8 % measured with the standard set up, to 11.3 % measured with the low density disc setup. The standard setup appears therefore to achieve a higher resolution size distribution. The size distribution measured by

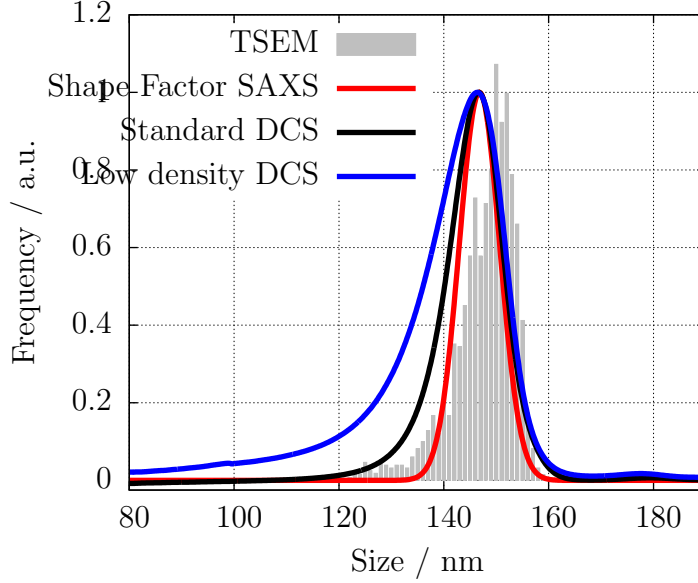


Figure 5.6: Number-weighted size distribution of PS-Plain particles measured by DCS, TSEM (Nicolet *et al.* 2016) and SAXS with the scattering shape factor approach.

TSEM with a  $p_d$  of 8.3 % shows good agreement with the ensemble techniques.

The measurements obtained by AFM provide polydispersity degrees larger than 10 % (Nicolet *et al.* 2016) and, therefore, slightly broader size distributions than those calculated by SAXS, TSEM and standard DCS. This can be in part attributed to the low statistics that typically affect imaging methods, along with artefacts associated with the posterior analysis.

For instance, in the TSEM images (Nicolet *et al.* 2016), smaller and larger populations with different contrasts have been observed which could affect the evaluation of the density measured by ensemble techniques in §5.4, as the particle average density might vary. Indeed, when a bimodal distribution is used to analyze the SAXS shape factor of PS-Plain particles, a second size population is found at 101 nm in agreement with TSEM, while the main mode maintains a  $p_d$  of ca. 5 %.

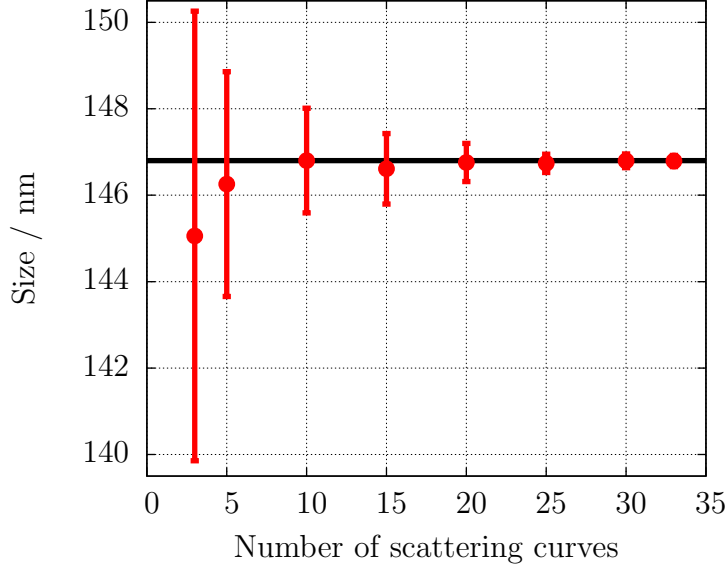


Figure 5.7: Size of PS-Plain as a function of the number of scattering curves used in the shape factor calculation.

## 5.3 Considerations about contrast variation data evaluation

### 5.3.1 Shape factor formalism

The shape factor obtained by density gradient contrast variation has been demonstrated as a powerful technique which can provide precise information about the size distribution and shape of the colloid by fitting a simple form factor.

However, an accurate determination of the suspending medium density for each scattering curve is required, due to the increased uncertainties Lefebvre *et al.* (2000) that can arise from the resolution of the system of linear equations described in the **Supplementary Information**.

Besides, a minimum of 3 scattering curves measured at different contrasts is necessary to obtain the resonant term, although an increasing number improves the determination of the size distribution. This issue has been addressed with the data measured by the density gradient contrast variation of the PS-F colloid.

From the 40 experimental curves, only a limited number  $N$  was randomly selected to compute the shape factor, while this process was repeated 100 times. The mean

	Raw data		Corrected data		Deviation
	$q^*$ (nm <sup>-1</sup> )	Size (nm)	$q^*$ (nm <sup>-1</sup> )	Size (nm)	%
$q_1^*$	0.0633	142.0	0.0631	142.4	0.3
$q_2^*$	0.1088	142.0	0.1076	143.6	1.1
$q_3^*$	0.1537	141.9	0.1510	144.4	1.7
$q_4^*$	0.206	136.6	0.195	144.3	5.3

Table 5.2: Isoscattering points position and the corresponding particle size for the scattering curves before and after background correction

size obtained from this data set and its standard deviation are plotted in figure 5.7 as a function of  $N$ .

The effect of increasing the number of measured contrasts evidences that the result tends asymptotically to the value of 146.8 nm discussed in §5.2 and the standard deviation of the 100 iterations decreases for large  $N$ , e.g. the associated uncertainty. This outcome emphasizes further the advantages of the continuous contrast variation technique due to the large number of scattering curves at different contrasts which can be easily measured.

Simulation depending on number of curves

## Advantages and disadvantages

### 5.3.2 Isoscattering point approach

It is noticeable in figure 5.3b that the subtraction of the suspending medium scattering plays an important role in the  $q^*$  values as the curve shifts to smaller  $q$ -values when subtracting the previously calibrated solvent scattering, as summarized in table 5.2.

The isoscattering point  $q^*$ , where all the scattering curves have the same intensity independently of the contrast, was first formulated by (Kawaguchi *et al.* 1983). It relates in a simple way the position of  $q^*$  with the size of the particle inaccessible to the suspending medium and, thus, a good method to determine the diameter of the colloid.

The theory defines  $q^*$  as a morphological parameter independent of the suspending medium density, which is a enormous practical advantage as it can be located without the proper calibration of the contrast. In cases where the composition of the buffer is unknown or the density of the solvent cannot be properly calibrated, the isoscattering point position might still be quantifiable by calculating the relative standard deviation of all the measured scattering curves. In order to obtain reliable



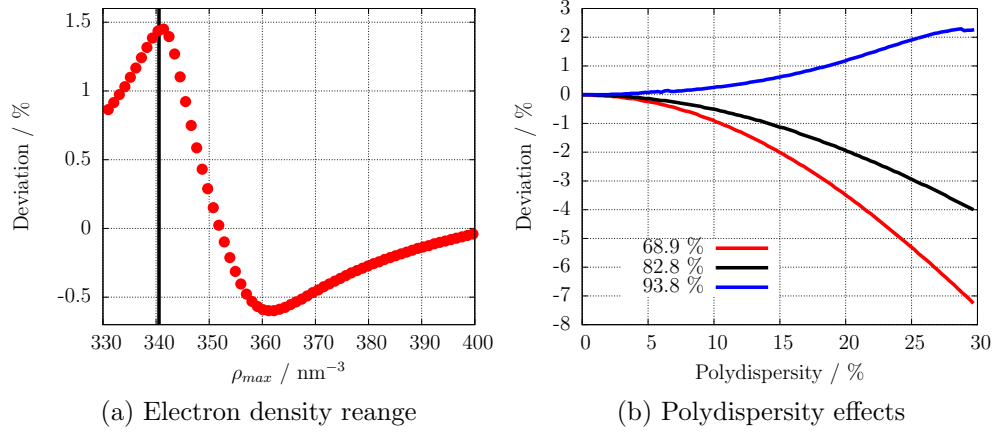


Figure 5.8: Deviation of the size calculated from  $q_1^*$  from the nominal value depending on the contrast range ( $330 \text{ nm}^{-3}$ ,  $\rho_{max}$ ) or the polydispersity of the core-shell colloid.

results, a proper subtraction of the solvent scattering must be performed as discussed in §5.2.

Nevertheless, it has been demonstrated that the polydispersity of the latex and its ellipticity influence the position and diffuseness of  $q^*$ , principally at high  $q$ -values [REF](#). This can disturb the size determination for lattices with broad size distributions and limit the applicability of this technique.

Besides, this work demonstrates that the  $q^*$  value determined with the previously described method depends on the range of solvent densities used in the contrast variation experiment. This conflicts partly with the initial intuition that this technique is independent of the experimental practice, although it can be avoided by selecting the range skillfully.

For this purpose, it was simulated the result of a contrast variation experiment with 10 different solvent densities for a colloid with the morphology and size distribution obtained with the onion model and presented in figure 5.1. Using a lower bound to the contrast range of  $\rho_{min} = 330 \text{ nm}^{-3}$  and increasing systematically the upper limit, it is shown in figure 5.8a that the calculated result deviates from the nominal value until 1.5%. This could be one explanation behind the size differences observed in figure 5.5 between the SAXS results.

In this example, the largest deviations occur when the contrast range excludes the average density of the latex, e.g. match point (depicted as a grey line), or when  $\rho_{max}$  is close to this matching density. These observations are applicable to other contrast variation experiments, advising to include the match point in the contrast

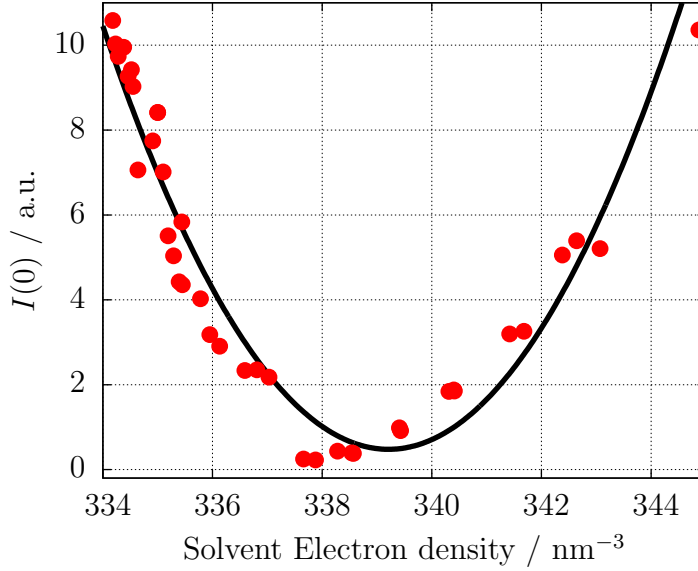


Figure 5.9: Intensity at zero-angle of PS-Plain particles as a function of the solvent electron density measured with continuous contrast variation in SAXS. The minimum defines the average electron density of the particle.

range and extending it along all the possible components' densities of the colloid.

#### Advantages and disadvantages

### 5.4 Determination of the particle physical density

In contrast variation SAXS, the solvent electron density which matches the average electron density of the particle ( $\rho_0$ ) corresponds to a minimum in the intensity of the scattering curve. In order to quantify the particle density, the scattering intensity of PS-Plain at zero angle  $I(0)$  is examined along the contrast range of the experiment as shown in figure 5.9. The value of  $I(0)$  was determined by extrapolation to  $q \rightarrow 0$  using a spherical form factor function fitted to the available range before the first minimum.

This parameter behaves parabolically around the average electron density of the particle like  $I(0) \propto (\rho_0 - \rho_{solv})^2$  (Avdeev 2007). From the position of the minimum,  $\rho_0$  can thus be solved. The parabolic fit to the data is plotted as a black line in figure 5.9 and results in  $\rho_0 = (339.2 \pm 1.0) \text{ nm}^{-3}$ , which is consistent with the tabulated

value of dry bulk polystyrene  $339.7 \text{ nm}^{-3}$  (Dingenouts *et al.* 1999).

The electron density is directly proportional to the physical density. Nevertheless, an assumption about the polymer (or monomer) components and their atomic structure is necessary for the calculation. Therefore, a typical value of  $Z/A = 0.54$  was adopted, where  $Z$  and  $A$  are the average atomic number and mass of the polymer respectively.

### 5.4.1 Validation through comparison with DCS

In figure 5.10, the value of  $(1.043 \pm 0.003) \text{ g cm}^{-3}$  obtained with the  $I(0)$  approach from the continuous contrast variation experiment is compared to the average density of the PS-Plain colloid measured with different DCS configurations. For single disc setups, the size value used for the density calculation was 147 nm, as measured by SAXS, while combining the information from the two setups allowed the measurement of the density independently of the particle diameter, as explained in §5.2.

The results agree with each other within their stated measurement uncertainties, although DCS measurements exhibit slightly higher densities than SAXS. Typical causes of systematic errors in DCS are the inaccuracy of the size and density of the calibration standard and the thermal variation in the centrifuge gradient during the measurements, which affect its viscosity and density (Kamiti *et al.* 2012). A temperature variation within the gradient of about 7 degree C before and after measurements was detected and a period of 30 min was considered appropriate to reach reliable thermal equilibrium. In the low density disc configuration, the accuracy of the average density of the D<sub>2</sub>O sucrose gradient becomes an important source of uncertainty.

### Uncertainties

In SAXS, the uncertainty is associated to the vertical size of the focused X-ray beam as in (Garcia-Diez *et al.* 2015). Furthermore, the result can be affected by the polymeric composition of the colloid, and therefore, the assumption of  $Z/A$ .

### 5.4.2 Use for homogenous polymeric colloids

The applicability of the continuous contrast variation techniques is further discussed by comparing with DCS for higher-density polymeric colloids, as summarized in figure 5.10. The density of the PS-COOH particles derived from the  $I(0)$  approach is in excellent agreement with that measured by DCS using a standard configuration

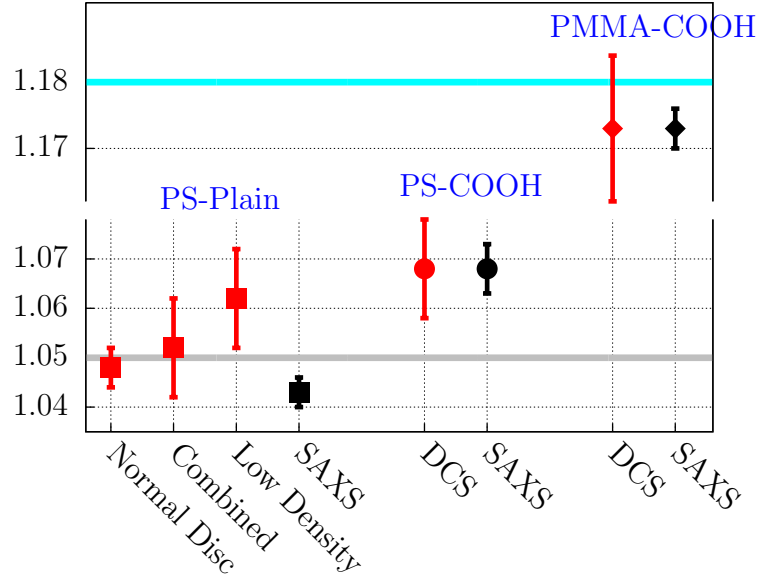


Figure 5.10: Comparison between the physical densities of 3 polymeric colloids measured with SAXS using the  $I(0)$  approach and DCS: PS-Plain (squares), PS-COOH (circles) and PMMA-COOH (diamonds). The nominal densities of polystyrene ( $1.05 \text{ g cm}^{-3}$ ) and PMMA ( $1.18 \text{ g cm}^{-3}$ ) are also shown in the plot as horizontal lines [22].

and assuming a particle diameter of 99.4 nm, which was obtained by SAXS. These core-shell particles, more dense than polystyrene (Garcia-Diez *et al.* 2015), illustrate the tendency during the emulsion polymerization to segregate polar and nonpolar components (Dingenouts *et al.* 1994c).

Similarly, the density of the PMMA-COOH colloids was measured using the standard DCS setup and assuming a diameter of 186.5 nm, as measured by SAXS. This value is compared to the density obtained by computing the intensity at zero-angle of a continuous contrast variation experiment. Again, both techniques are in excellent agreement and reveal a physical density slightly lower than the expected PMMA density of  $1.18 \text{ g cm}^{-3}$  (Dingenouts *et al.* 1999).

This result highlights the fact that the density of polymeric colloids in suspension may vary from that of bulk materials, for example dry particles. For instance, a volume variation can be expected when going from the MMA monomer to the polymer PMMA (Nichols & Flowers 1950) which might reduce the colloid density.

## 5.5 Summary

This work demonstrates how continuous contrast variation in SAXS emerges as a powerful characterisation technique for polymeric colloids, which can determine their size and density in a traceable way. For instance, the accuracy in the density information achieved with the density gradient technique is remarkable and extends along a rather large density range of polymers.

Since contrast variation in SAXS is very sensitive to small electron density differences in the colloid morphology, the applicability of this method to investigate the inner structure of 3 different particles has been discussed. This is of paramount importance in polymeric particle characterisation because the direct observation by imaging techniques is inadequate for this purpose.

The detection of core-shell structures in polymeric colloids appears as essential for understanding the possible processes occurring during the particle formation, e.g. the consequences of emulsion polymerization synthesis.

These results were compared successfully with other techniques. In particular, SAXS measurements of the density of these colloids are in excellent agreement with those performed by DCS. The use of a novel DCS setup is also shown, which makes use of a centrifuge disc where the colloids float through a gradient of higher density, in contrast to a standard setup where the particles typically sediment. The use of the two complementary DCS configurations allowed the simultaneous determination of both the size and density of polymeric colloids consistently with the SAXS results.

Furthermore, different evaluation approaches to contrast variation SAXS data are examined in detail. The isoscattering point framework is found to be of easy utilization and very appropriate for spherical and quite monodisperse colloids. On the other hand, the calculation of the scattering shape factor arises as a precise sizing technique which can additionally provide an insight into the particle shape, although a high number of measurements with different contrasts and an accurate calibration of the system are required.

With the continuous contrast variation technique in SAXS, a more precise characterisation of the morphology of polymeric particles is achieved which opens new opportunities to investigate complex polymeric colloids. Besides, both ensemble techniques presented in this paper arise as powerful methods which can describe simultaneously the density and size distribution of polymeric colloids at the nanoscale.

## Chapter 6

# Continuous contrast variation applied to relevant bio-materials

In the continuously growing world of nanotechnology, nanoscience provides understanding for biological structures at the nanometer length scale, such as lipoprotein biology, while the application of nanoparticles in medicine opens exciting new possibilities in this field Nie *et al.* (2007); Sahoo & Labhasetwar (2003); Wickline & Lanza (2003); Zhou *et al.* (2014); Rosen & Abribat (2005). For example, polymeric colloids and other biodegradable nanocarriers are finding many medical applications (Vicent & Duncan 2006) and are starting to undergo clinical trials (Patel *et al.* 2012; Beija *et al.* 2012; Cabral & Kataoka 2014).

In this sense, liposomes have an increasing importance in the emerging field of nanomedicine, due to their capacity to encapsulate hydrophilic compounds within the closed phospholipid bilayer membrane. The first approved nanodrug, Caelyx®, consists of a PEGylated liposomal formulation of doxorubicin. In fact, liposomal nanocarriers are nowadays a widespread instrument for drug delivery.

Despite SAXS being a usual method of choice for the accurate characterization of nanomaterials, the interpretation of the scattering curves, i.e. the uniqueness of the solution of the model fitting, is frequently intricate for complex samples. Liposomal drugs or loaded polymeric nanoparticles belong to this class, as both the carrier and the incorporated biotarget contribute to the scattering intensity.

Therefore, the characterization of NPs with a broad size distribution, a heterogeneous composition or with a complicated inner structure require either *a priori* knowledge about the morphology of the sample or the measurement of complementary scattering curves obtained under different experimental conditions, like in solvent contrast variation in SAXS

In this chapter, the utilization of continuous contrast variation in SAXS is examined for the nanodrug Caelyx® and for typical nanocarriers like lipid vesicles or polymeric colloids. In the latter case, the particle is coated with an antibody to resemble the biological conditions found upon injection in the bloodstream. Other components of the blood plasma like lipoproteins are also investigated with this technique.

## 6.1 Materials and methods

The continuous contrast variation method in SAXS has been employed in a variety of samples related with nanomedicine. In this section, the different samples characterized with this technique are described and the more relevant aspects of the experiments are detailed. The results obtained on the Caelyx® nanodrug are described principally in section 6.2 and 6.3.1, while the empty liposomes are investigated under osmotic pressure in section 6.3.2. The size measurements on the lipoproteins are presented in section 6.4 and the use of the protein-coated nanoparticles is detailed in section 6.5.

### 6.1.1 Caelyx®: PEGylated liposomal doxorubicin

The PEGylated liposomal formulation of doxorubicin, Caelyx® (SP Europe, Brussels, Belgium), was purchased from Hungaropharma Ltd. Caelyx ® (or Doxil ® in US) consist of liposomes formed by fully hydrogenated soy phosphatidylcholine (HSPC), cholesterol, and DSPE-PEG2000 (N-(carbonyl-methoxypolyethylene glycol 2000)-1,2-distearoyl-sn-glycero-3-phosphoethanolamine). The latter results a steric barrier at the liposomal surface due to the PEG 2000 residues. Doxorubicin is encapsulated in Caelyx ® via an active loading procedure, which results a crystal-like doxorubicin precipitate inside the liposomes, as observed in the micrograph 6.1a. An schematic depiction of the sample morphology is shown in figure 6.1b.

The suspending medium contrast variation study was performed with the iso-osmolar contrast agent Optiprep ® (an aqueous solution of iodixanol), which has an osmolality of 290 to 310 mOsm kg<sup>-1</sup>. The suspending medium density gradient was achieved by bringing together two mixtures of different densities: For the bottom of the capillary, a high density mixture of Caelyx ® was prepared with an Optiprep ® mass fraction of 35 % and a corresponding solvent electron density of 365.2 nm<sup>-3</sup>, whilst on the top side of the capillary a low density preparation of Caelyx ® using phosphate buffered saline solution (pH 7.4) with the same volume fraction of Caelyx ® was introduced, with a solvent electron density of 341.9 nm<sup>-3</sup>. By employing

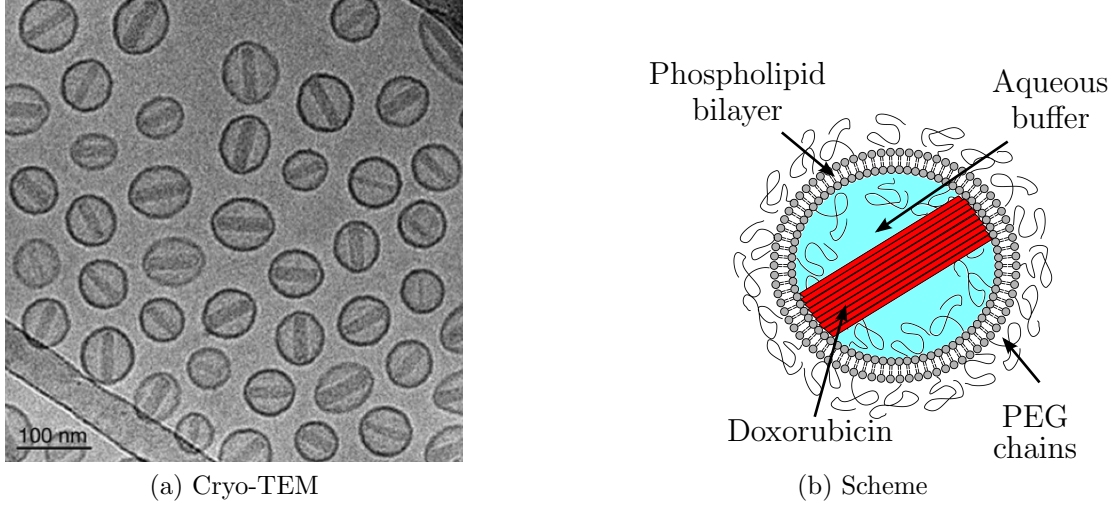


Figure 6.1: Cryo-TEM image of Caelyx® Barenholz (2012) and schematic representation of the PEGylated liposomal doxorubicin morphology Garcia-Diez *et al.* (2016).

Optiprep ® as a contrast agent, the suspending medium osmolality is constant along the capillary.

In order to study the effects of the suspending medium osmolality in the liposomal drug carrier, another capillary with a density gradient was created by introducing a dense aqueous sucrose solution with 37.8 % sucrose mass fraction (Sigma-Aldrich, Missouri, USA) at the bottom of the capillary (which corresponds to an electron density of  $381.1 \text{ nm}^{-3}$  and a solvent osmolality of  $1775.6 \text{ mOsm kg}^{-1}$ ), whereas a lighter solution was produced without sucrose by adding pure water to get the same Caelyx ® concentration. Considering the sucrose mass fraction of the Caelyx® buffer to be 10%, this latter preparation has an electron density of  $339.4 \text{ nm}^{-3}$  and an osmolality of  $151.1 \text{ mOsm kg}^{-1}$ .

A wide-angle configuration was employed to observe the diffraction peak of the fiber-like doxorubicin precipitate encapsulated in the liposomes. At this configuration, the sample-to-detector distance was reduced to  $L = (569 \pm 1) \text{ mm}$  and as a result the available  $q$ -range was extended until  $5.55 \text{ nm}^{-1}$ . For the wide-angle X-ray scattering measurements, a density gradient capillary was prepared using a denser aqueous solution with a sucrose mass fraction of 34% and a lighter one with 6%.



### 6.1.2 Lipid vesicles: PEGylated and plain liposomes

The PEGylated liposomes were prepared with the same lipid composition that the commercially available Caelyx ® for comparison purposes: the weight ratios of HSPC:DSPE-PEG 2000:cholesterol were 3:1:1 (corresponding to molar ratios of 0.565:0.053:0.382). The samples were extruded through polycarbonate filters (Nucleopore, Whatman Inc., Little Chalfont, UK) of 5 different pore sizes, from 50 to 400 nm. A more detailed description of the preparation is found elsewhere Varga *et al.* (2014). The components of the plain liposomes are HSPC:cholesterol with a weight ratio of 3:1 (corresponding to molar ratios of 0.6:0.4). The preparation is identical to the PEGylated liposomes. All the liposome samples are suspended in a 10 mM phosphate buffered saline (PBS) pH 7.4 buffer solution.

The DLS size measurements were performed on a W130i apparatus (Avid Nano Ltd, High Wycombe, UK) in the Institute of Materials and Environmental Chemistry (Hungarian Academy of Sciences, Budapest, Hungary) similarly to the protocol described in Varga *et al.* (2014). The samples sizes employed in the discussion of section 6.3.2 are the **intensity-weighted** results from these measurements. It is apparent from these measurements that the size of the pore and the polydispersity degree of the liposome sample are directly related.

The concentration of sucrose employed to constitute the high-density phase of the different density gradients is detailed in the discussion of section 6.3.2. The top-part of the capillary was filled with a diluted preparation of the sample in buffer to match the liposome concentration in the bottom phase.

### 6.1.3 Human lipoproteins

Native lipoproteins from human plasma were purchased from Merck Milipore (Darmstadt, Deutschland) and suspended in 150 mM NaCl, 0.01 % EDTA buffer with pH 7.4. The High Density Lipoprotein (HDL) had a protein concentration of 14.3 g/L, while the Low Density Lipoprotein (LDL) had a protein concentration of 5.96 g/L, considering that the weight ratio between lipids and proteins is approximately 4:1 in the LDL sample.

In figure 6.2, a single-contrast SAXS curve of HDL in buffer is displayed, where the best fit of a core-shell model is also shown. It is evident that the fit does not match the data correctly and, thus, the morphology of the lipoprotein cannot be described with a simple core-shell model. The complementary measurements were performed by continuous contrast variation in SAXS using sucrose as contrast agent. The maximum sucrose mass fraction employed in the preparation of the density gradients was 40 %, as detailed in section 6.4.

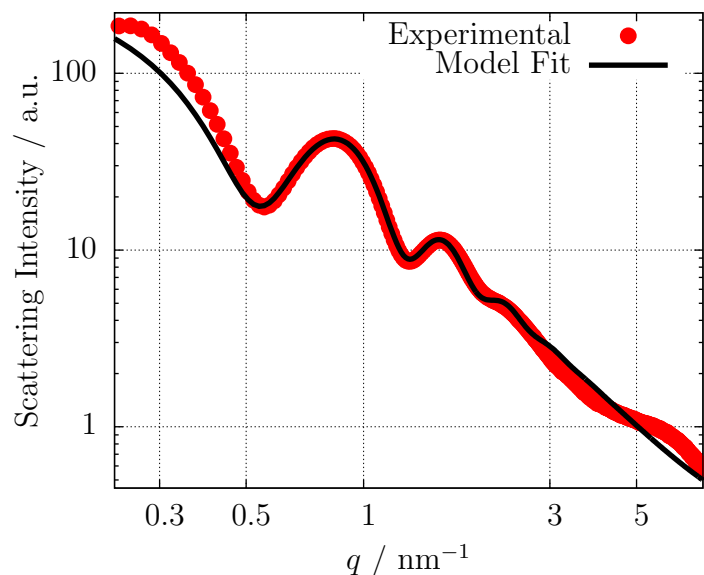


Figure 6.2: Scattering curve of HDL: A core-shell model is fitted to the experimental data (red symbols) resulting in an outer diameter of 9.7 nm and a core radius of 4.2 nm.

#### 6.1.4 PS-COOH particles coated with IgG

The polystyrene nanoparticles with carboxylated surfaces (PS-COOH) described in section **WHICH ONE???** are coated with the protein Immunoglobulin G (IgG). A set of four IgG-coated polystyrene nanoparticle samples was prepared by incubating 0.05 % (w/w) particles with varying concentrations of IgG from 0.5 to 4 g/L in 100 mM Tris buffer at pH 8 under continuous shaking for 2 h. Any unbound IgG was then removed from the particle samples by three cycles of centrifugation and redispersion in clean buffer.

In the continuous contrast variation experiment with sucrose as contrast agent, a protein concentration of 4 g/L IgG was physisorbed at the surface of the bare PS-COOH particles. The details of the density gradient capillary are discussed in section 6.5.1.

## 6.2 Traceable size determination of a liposomal drug

The first approved nano-drug was Doxil® (Caelyx® in Europe), a PEGylated liposomal formulation of doxorubicin, which was followed by a few other products Yeh *et al.* (2011); Barenholz (2012). Nowadays there are approximately 250 nanomedicine products that are either approved by the relevant health agencies or are under clinical trials Etheridge *et al.* (2013). On the other hand, there is a translational gap between the experimental work devoted to the development of new nano-drug candidates and the clinical realization of their use, which is also reflected in the high number of studies dealing with nanomedicine and the number of approved products on the market Khorasani *et al.* (2014); Venditto & Szoka Jr. (2013). As highlighted in a recent review by Khorasani *et al.* (2014), one of the main reasons for this translational gap is that the current characterization techniques possess limitations and there is a need for standardization on this field.

Among many relevant physicochemical properties of nano-drugs, one of the most important to be accurately determined is the size of the nanocarriers, which directly relates to the *in vivo* biodistribution of the drug. The ultimate goal in this regard is to reach a "traceable size determination" of the nanomaterial, which means that the measurand can be related to the SI unit "meter" through an unbroken chain of comparisons with known uncertainties.

The most widely used technique for size determination in the field of nanomedicine is dynamic light scattering (DLS), which measures the hydrodynamic diameter of the nanoparticles (NPs) Murphy (1997); Hallett *et al.* (1991); Egelhaaf *et al.* (1996); Takahashi *et al.* (2008); Jans *et al.* (2009); Hoo *et al.* (2008). DLS is well-established and has indisputable advantages in the size characterization of the NPs, e.g. easy-to-use instrumentations, fast and low-cost operation, but it is not capable of a traceable size determination as there is no general relationship between the hydrodynamic diameter and the physical size of the NPs Meli *et al.* (2012).

Transmission electron microscopy (TEM) is also frequently used for sizing of NPs and proved to be an appropriate technique for solid nanoparticles, whilst its employment in soft matter NPs (e.g. liposomes, micelles and polymeric nanoparticles) is questionable due to the possible distortion of the particles during the drying process. Although cryo-TEM could overcome this limitation Li *et al.* (1998), the statistical accuracy of this non-ensemble method is usually not sufficient.

SAXS is capable of traceable size determination for sufficiently monodisperse nanoparticles Meli *et al.* (2012) and therefore the continuous contrast variation technique with SAXS is a suitable method to assess the size of a complex liposomal

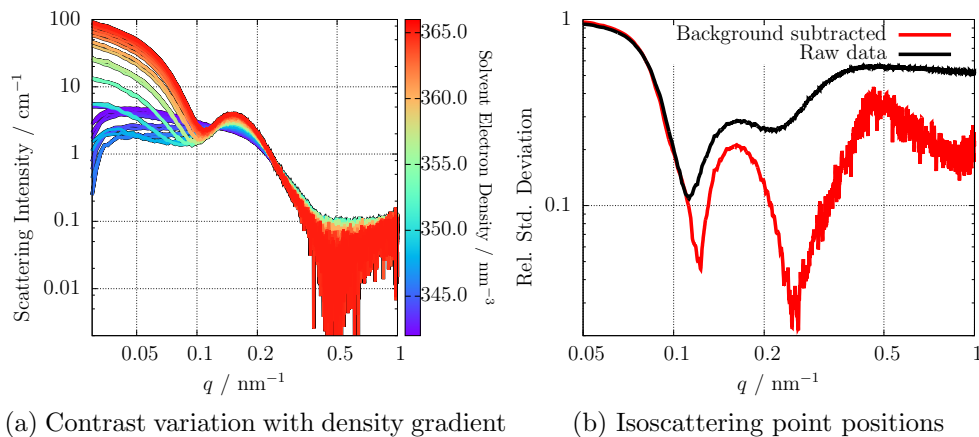


Figure 6.3: a) Scattering curves at different suspending medium electron densities obtained with a solvent density gradient of Caelyx in aqueous iodixanol with constant buffer osmolality. Figure b) shows the precise position of the isoscattering points before and after the proper correction of the background.

drug, such as the PEGylated liposomal formulation of doxorubicin. The need of an iso-osmolal suspending medium to mimic the physiological conditions of plasma requires the use of Optiprep® as contrast agent, as explained in section 6.1.1.

SAXS curves of the liposomal doxorubicin sample measured at different suspending medium electron densities are shown in figure 6.3a. In the scattering curves, it is possible to observe the variation of the curve features through the increase of the suspending medium density, which indicates the complexity of the internal structure of the nanocarrier. Besides, the appearance of an intersection point around  $q = 0.12 \text{ nm}^{-1}$  is a further indicator of the structural complexity of the drug-carrier.

The solvent background has been subtracted by measuring the scattering curves of a density gradient of Optiprep® and buffer without nanocarriers. The low scattering power of the PEGylated liposomal doxorubicin at high  $q$  values and the contribution of the iodixanol background result in an increased uncertainty in the high- $q$  range of the corrected scattering curves, although in the Fourier region below  $q = 0.3 \text{ nm}^{-1}$  the background effect is much less dominant.

### 6.2.1 Isoscattering point approach

In the low  $q$  part of the scattering curve, an isoscattering point is clearly visible as highlighted in figure 6.3a, where all the scattering curves intersect at one point. The isoscattering point position relates directly to the external radius of the measured

particle inaccessible to the solvent, as explained in the [Supplementary Information. WHERE?](#) Therefore, the PEG-chains attached to the liposome surface might not be quantified in this approach due to the permeability of the polymer layer. The isoscattering point position is precisely determined by calculating the relative standard deviation of all the scattering curves at each  $q$ -value, as shown in figure 6.3b. [As discussed before WHERE???, the proper subtraction of the solvent background is essential for the right interpretation of the data, specially for intense incoherent scatterers like Optiprep ®.](#) A clear shift in the minima of the relative standard deviation curve is observed in figure 6.3b after correcting the background effects. Hence, the first isoscattering point  $q_1^*$  is located at  $q_1^* = 0.123 \text{ nm}^{-1}$ , which corresponds to a radius of  $R = 36.5 \text{ nm}$  and a diameter of  $73 \text{ nm}$ . A second isoscattering point at  $q_2^* = 0.25 \text{ nm}^{-1}$  is still visible, although the diffuseness of the isoscattering points at higher  $q$  values, related with the polydispersity of the ensemble, makes it less reliable for the determination of the outer radius.

The determination of the  $q$  values have an associated relative uncertainty of 0.1 %, which corresponds to a size uncertainty of 0.6 nm. Furthermore, the radial integration of the scattering pattern was performed choosing a  $q$ -bin of size  $0.0015 \text{ nm}^{-1}$ , with an associated uncertainty in the size of 0.9 nm. Without further considerations, the Caelyx® size uncertainty associated to the determination of the  $q$ -value of the isoscattering point is 1.1 nm. Other possible sources of uncertainty arise from the polydispersity degree of the sample and the ellipticity of the doxorubicin loaded liposomes, which might shift the measured position of the isoscattering point, although the uncertainty associated to them cannot be easily quantified.

## 6.2.2 Shape factor calculation

In order to provide a traceable uncertainty for the obtained size value, we have used an alternative evaluation procedure, namely the calculation of the so-called shape factor (Stuhrmann & Kirste 1965, 1967) which extracts all contributions from the 30 measured scattering curves that change with the contrast at different solvent densities. The shape factor of the Caelyx® sample contains essentially information only about the shape and size distribution of the space filled up by the liposomes, i.e. the contributions of the phospholipid bilayer and the encapsulated doxorubicin to the scattering intensity are cancelled. Thus, the complex interpretation of the original SAXS curve of Caelyx® is avoided and enables the size determination of the liposomal carrier by fitting a simple analytical model for homogeneous spherical objects. A model with a certain ellipticity was also attempted, due to the slight liposomal eccentricity observed in TEM images (Barenholz 2012) though the best fit

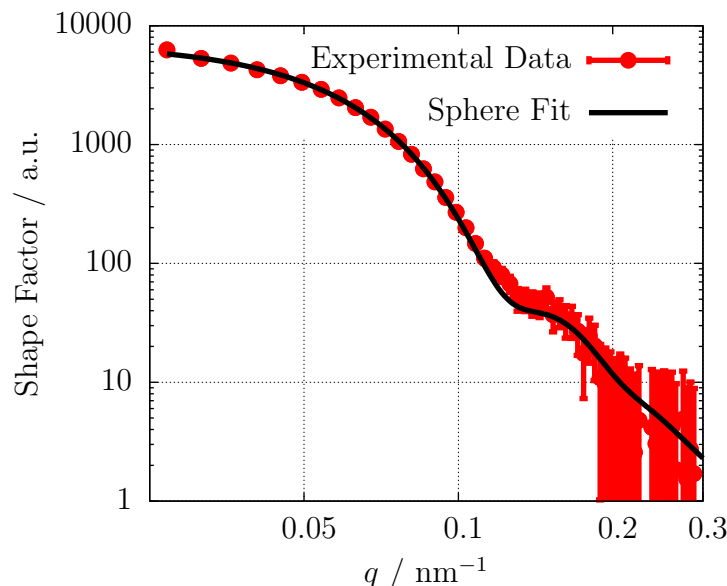


Figure 6.4: Experimental shape factor of the liposomes is shown with symbols and the model fit for homogeneous spherical particles is depicted with a thick line.

was accomplished with a spherical model. Details on the calculation of the shape factor as well as the analytical expression for the model fitting can be found in the [Supplementary Information. WHERE?](#)

The shape factor calculated from the SAXS curves and the theoretical model fitting are depicted in figure 6.4. The mean diameter obtained from the spherical form factor fit is  $(65.5 \pm 4.7)$  nm, slightly smaller than the value calculated from the isoscattering point position. Nevertheless, both values overlap when considering the associated standard uncertainties and that the polydispersity smearing of the isoscattering point is difficult to quantify. The latter fact is supported by the broad size distribution determined by the shape factor fitting. When assuming a Gaussian size distribution, the polydispersity degree (defined as the full width at half maximum of the size distribution divided by its mean value) of the nanocarrier is ca. 40%. Therefore, the average value of  $(69 \pm 5)$  nm can be embraced as a reliable external size for the liposomal drug-carrier.

The average size obtained by contrast variation in SAXS is smaller than the result obtained with DLS of ca. 86 nm (in-house measurement), which can be attributed to the fact that the DLS measurand is the hydrodynamic size of the nanoparticles, while SAXS provides the size of the spherical volume inaccessible to the solvent. As the 2 kDa PEG-chains attached to the surface of the liposomes contribute to

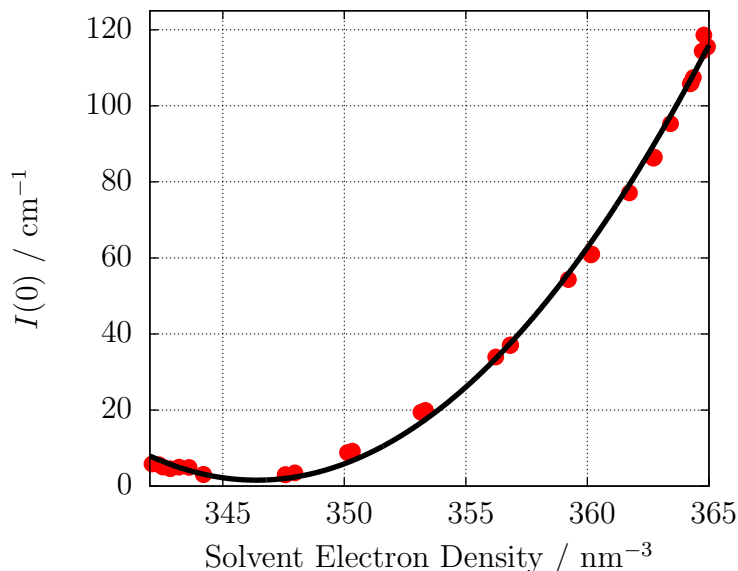


Figure 6.5: Measured intensity at zero-angle of Caelyx as a function of the electron density of the aqueous iodixanol suspending medium. The function fitted to the experimental data is depicted in black: Average density is  $346.39 \text{ nm}^{-3}$  and there is a offset of  $1.56 \text{ cm}^{-1}$

the hydrodynamic radius but that layer is permeable to the solvent and, therefore, invisible to contrast variation SAXS, the ca. 15 nm difference between the sizes determined by DLS and SAXS is justified.

### 6.2.3 Average electron density

At low  $q$ -values, the Guinier approximation can be used as explained in the [Supplementary Information. WHERE?](#). By fitting the spherical form factor to the  $q$ -range just below the first minimum of the scattering curves, an extrapolated value for the intensity at zero-angle  $I(0)$  could be obtained as displayed in figure 6.5. The minimum of the parabola fitted to the experimental points determines the average electron density of the drug carrier system, according to the equation  $I(0) \propto (\rho_0 - \rho_{solv})^2$  [CITE ORIGINAL EQUATION IN THE THESIS - THEORY CHAPTER](#).

From this calculation, a value of  $\rho_0 = (346.2 \pm 1.2) \text{ nm}^{-3}$  is obtained which corresponds to the density of the liposomal nanocarrier and the precipitated drug combined. The uncertainty of  $1.2 \text{ nm}^{-3}$  is associated with the vertical size of the focused X-ray beam. The obtained density is slightly higher than the value of  $338 \text{ nm}^{-3}$  estimated for empty PEGylated liposomes Kučerka *et al.* (2006) due to the

presence of the doxorubicin-sulfate aggregate in the intraliposomal volume.

## 6.3 Osmotic effects in liposomes

The rigidity of the nanocarriers is a relevant property directly related with its drug delivery efficacy, the particle stability or the release rate of the encapsulated drug. In fact, some of these characteristics might change upon injection due to the osmotic pressure applied to the nanocarriers in the process. In the case of lipid vesicles, i.e. liposomes, the permeability of water through the phospholipid bilayer is a defining aspect of its physicochemical behavior. Although many aspects about the membrane permeability have been studied Nagle *et al.* (2008); Mathai *et al.* (2008); Olbrich *et al.* (2000), the evaluation of the liposomes rigidity and its osmotic activity is still challenging.

The osmotic behavior of liposomes depends, basically, on their size and chemical composition. For example, the incorporation of cholesterol can vary the fluidity of the lipid bilayer. Larger liposomes tend to be osmotically active de Gier (1993) and behave according to the Laplace law: the osmotic pressure needed to deform them decreases for increasing sizes. In the case of liposomal nanocarriers, the intraliposomal osmolality should be equal to the buffer outside of the liposomes to enhance the particle stability.

Therefore, it is an important question whether the incorporation of a drug into the intraliposomal volume might modify its osmotic activity. For example, the small size of Caelyx® and the doxorubicin-sulfate aggregate in the intraliposomal volume create an extraordinary resistance against the buffer osmotic pressure in comparison to the empty liposomal particle. This effect can be studied by increasing systematically the osmolality of the suspending medium by increasing the sucrose concentration in the aqueous buffer. As shown in figure 6.6, the sucrose molecule acts simultaneously as a contrast agent and as an instrument to increase the solvent osmolality. This enables the study of the osmotic effects in liposomes by the density gradient technique with SAXS using aqueous sucrose as suspending medium, as it will be discussed in the following section.

Due to the constant osmolality of the suspending medium along the whole density gradient, no osmotic pressure effects were observed in the size or density of the liposomal drug Caelyx ® in the previous section 6.2. In this section, a thorough investigation of Caelyx ® under the effects of an increasing solvent osmolality is performed, complementary to the study of the empty liposomal nanocarrier under similar conditions. Besides, the consequences of PEGylation on the liposomal structure are also studied using this technique, focusing principally in its osmotic activity.



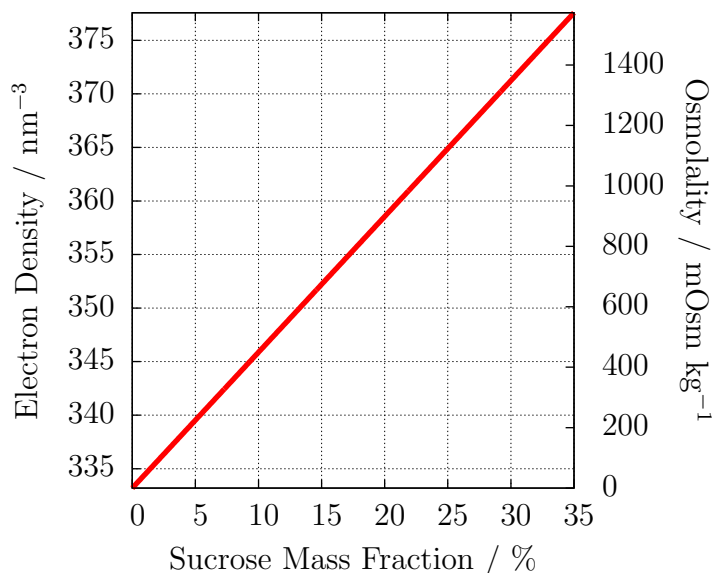


Figure 6.6: Relationship between solvent electron density and solvent osmolality for an aqueous sucrose solution.

### 6.3.1 Application to drug-stabilized liposomes

By means of the density gradient technique, scattering curves of the liposomal doxorubicin were recorded at different sucrose concentrations of the suspending medium, i.e. at different buffer osmolalities, as shown in figure 6.7a. The X-ray scattering measurements were performed at two different detector-to-sample distances, as described in section 6.1.1, in order to study a broader  $q$ -range, spanning from 0.03 to 5.55 nm<sup>-1</sup>, and observe the 1,0-diffraction peak of the doxorubicin fiber-like precipitate around  $q = 2.3$  nm<sup>-1</sup> Li *et al.* (1998), as depicted in the figure 6.8a after proper background correction.

As discussed in the previous section, by increasing the electron density of the suspending medium, the scattering curves of the drug carrier change drastically due to contrast variation. In the case of the aqueous sucrose gradient shown in figure 6.7a, this effect is also observed and strongly resembles the curves measured with the Optiprep ® density gradient depicted in figure 6.3a. Nevertheless, upon a certain sucrose concentration (greenish and reddish colored curves in figure 6.7a), the features of the scattering curves disappear abruptly, because the suspending medium osmolality is so high that it induces morphological changes in the liposomal structure and, consequently, the scattering form factor of the particles changes.

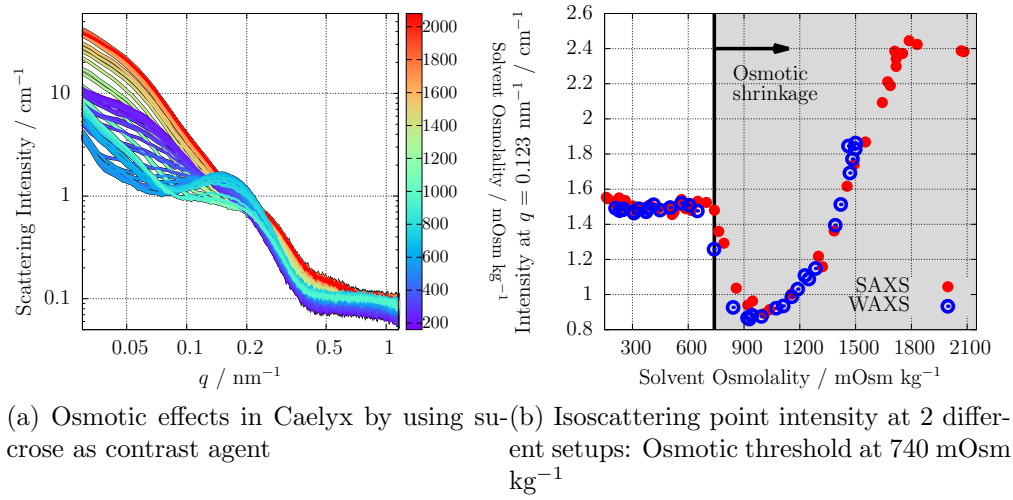


Figure 6.7: Scattering curves of Caelyx in an aqueous sucrose density gradient calibrated to the osmolality of the suspending medium. Intensity of the first isoscattering point depending on the aqueous sucrose solution osmolality is shown with black dots.

This effect can be quantified by examining the intensity of the first isoscattering point at  $q_1^* = 0.123 \text{ nm}^{-1}$ , because the scattered intensity at this point should be independent of the electron density of the solvent, as observed with the Optiprep® gradient. The isoscattering point intensity as a function of the suspending medium osmolality is shown in figure 6.7b and there is a clear osmolality threshold at  $670 \text{ mOsm kg}^{-1}$ . Above this threshold, the osmotic pressure at the liposomal bilayer is so high that the liposome starts shrinking and changes its size, structure and, consequently, scattering form factor. The increased resistance against osmotic pressure, more than double the blood plasma osmolality and much higher than the osmolality needed to shrink empty PEGylated liposomes Varga *et al.* (2014), is explained by the encapsulation of doxorubicin inside the liposome.

The large osmotic pressure produces a reversible shrinkage of the liposome though it is not capable of cracking it. This was proved in an additional experiment by increasing the osmolality of the buffer to  $1333.6 \text{ mOsm kg}^{-1}$  with a sucrose mass fraction of 31.4% and then reducing it to  $565.4 \text{ mOsm kg}^{-1}$  by adding distilled water. The solvent with high osmolality produced a featureless scattering curve, as expected from figure 6.7a, whereas, after reducing the osmotic pressure, the scattering curve was the same as the measured Caelyx® curve with the corresponding electron density, which gives evidence that the osmotic shrinkage process is reversible.

The behavior of the nano-drug for an increasing solvent osmolality can be further

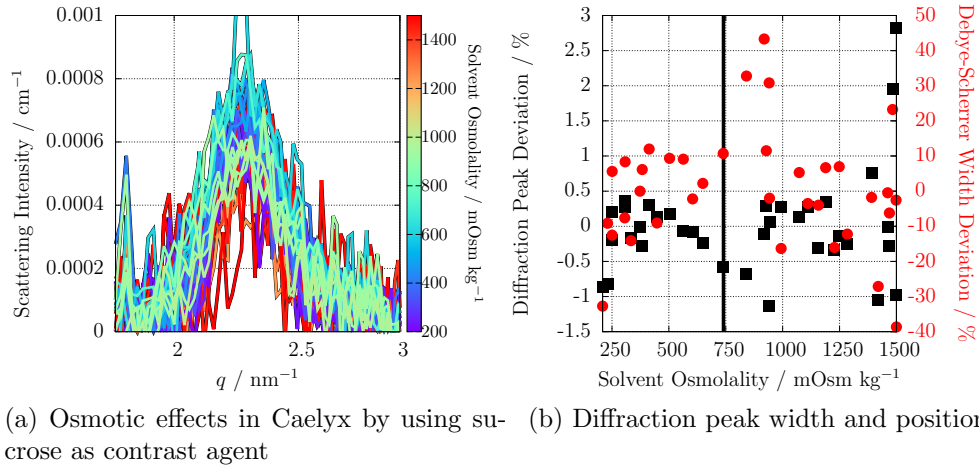


Figure 6.8: Measured in WAXS, the  $q$ -region where the doxorubicin diffraction peak appears can be observed. With black symbols, the shift of the doxorubicin-aggregate diffraction peak from  $q = 0.123 \text{ nm}^{-1}$  is displayed. The mean width (FWHM) is  $0.333 \text{ nm}^{-1}$ .

studied by evaluating the crystal structure of the doxorubicin aggregate, represented by the diffraction peak observed in the figure 6.8a. The position of the peak in the reciprocal space depending on the suspending medium osmolality is depicted in figure 6.8b and shows that its position deviates less than 1 % from the weighted average  $q = 2.28 \text{ nm}^{-1}$  along the whole osmolality range. This proves that the fiber-like structure of the drug inside the liposome is also constant during the osmotic shrinkage of the liposomes. The measured position of the (1,0) diffraction peak matches exactly the value measured from doxorubicin-sulfate complexes in solution Lasic *et al.* (1992). It can also be observed in figure 6.8b how the width of the diffraction peak does not change significantly along the osmolality range and thus, according to the Scherrer equation Cullity & Stock (2001), the size of the precipitated doxorubicin remains stable upon the osmotic shrinkage.

To conclude this section, the diameter obtained from the isoscattering position in the aqueous iodixanol solution can be compared with what is measured in an aqueous sucrose suspending medium. In the latter, if only the scattering curves below this osmolality threshold are considered, the relative standard deviation for each  $q$  value reveals a pronounced minimum for the first isoscattering point as depicted in figure 6.9. When comparing this result with the relative standard deviation curve obtained from the Optiprep <sup>®</sup> contrast variation measurements, both values for the size of the drug carrier agree remarkably well within 0.8 %. This reflects the independence

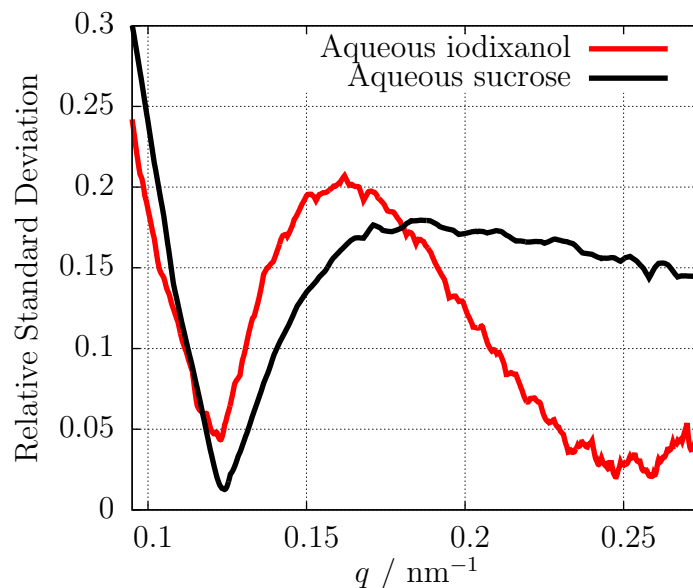


Figure 6.9: Isoscattering point position quantified by the calculation of the relative standard deviation of the scattering curves for different solvent density gradients. In the case of the aqueous sucrose solution (black line), only the scattering curves below the osmolality threshold were employed for the calculation.

of the technique from the contrast agent added to the suspending medium and shows the repeatability of the results.

### 6.3.2 Does PEGylation affect the osmotic activity of liposomes?

Typically, unilamellar liposomes present a very narrow size distribution and spherical shape, whose diameter ranges from 50 nm to some hundreds of nanometers, and emerge as suitable nanocarriers for drug delivery. The covalent attachment of biocompatible polymers can improve the liposome stability. For example, polyethylene glycol (PEG) shows very low toxicity Yamaoka *et al.* (1994) and is a widely used stabilizer Sou *et al.* (2000). PEGylated liposomal formulations, also called sterically stabilized liposomes (SSL), show longer blood circulation times *in vivo* Barenholz (2001) and exhibit a slow drug release rate. PEG-modified liposomes have become of importance lately due to their increased drug pharmacokinetics, decreased plasma clearance and improved patient convenience Gabizon & Martin (1997); Harris & Chess (2003). Therefore, the self-assembly of lipid structures in the presence of PEG

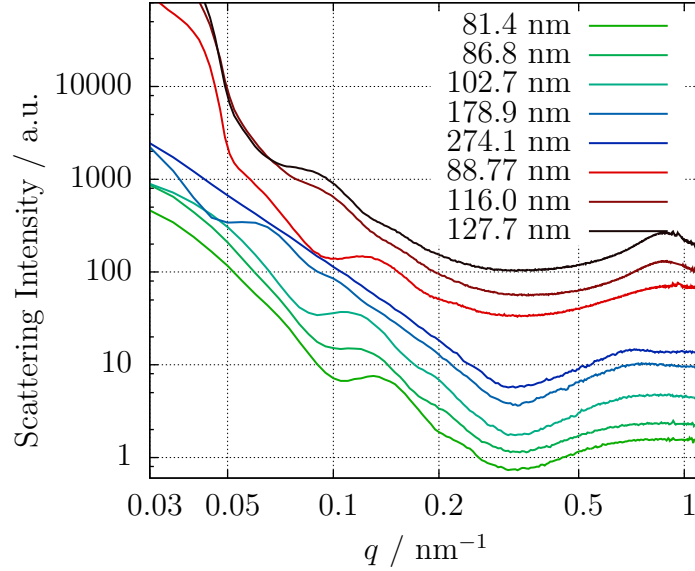


Figure 6.10: Scattering curves of the different liposomes in buffer. The curves are intensity shifted for clarity. The 5 SSLs are presented in the lower part of the plot. The sizes in the legend are extracted from DLS measurements.

moieties has been studied for different lipids Lee & Pastor (2011).

The incorporation of biocompatible polymers increases the phospholipid bilayer strength and enhances the vesicle rigidity, which relates to the increase of the bending modulus Liang *et al.* (2005); Sou *et al.* (2000). The higher membrane stiffness of SSLs has been extensively characterized with methods such as Atomic Force Microscopy (AFM) Spyratou *et al.* (2009) though other techniques such as light scattering have found a higher osmotic activity in SSLs in comparison to their non-PEGylated counterparts when incubated in serum Wolfram *et al.* (2014). Further investigations about the relationship between PEGylation and the liposomal osmotic behavior in suspension are essential. In the following work, the different response of SSLs and plain liposomes to osmotic pressure is studied with SAXS. The creation of multilamellar domains in the phospholipid layer is evaluated and the role of the PEG moieties in the membrane resilience is also analyzed.

For this purpose, 5 PEGylated and 3 plain liposomes were extruded with different pore sizes, as explained in section ???. To simplify the following discussion, the liposomes are named after the hydrodynamic diameter measured by DLS. The SAXS measurements of the 8 liposomes are showed in figure 6.10, where the first minimum shifts from  $\sim 0.1 \text{ nm}^{-1}$  to smaller  $q$ -values for increasing size. For high polydispersities

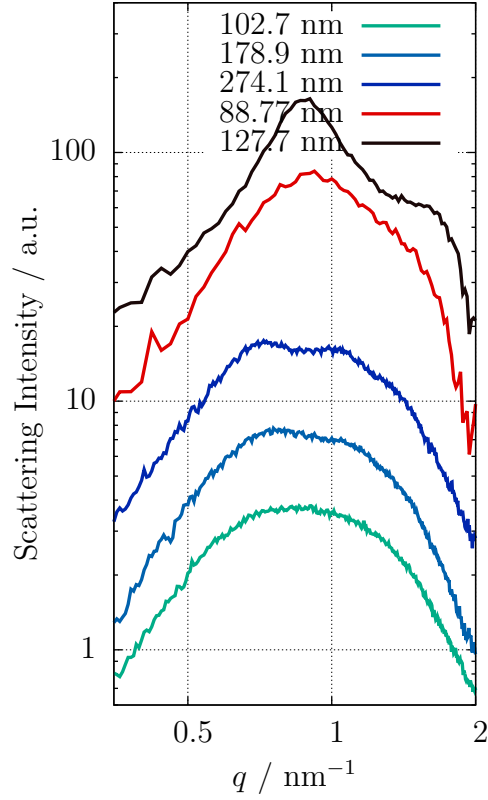


Figure 6.11: The phospholipid bilayer feature: High  $q$ -region of the scattering curves of 2 plain liposomes and the 3 largest SSLs. The SSLs are presented in the lower part of the plot.

this scattering minimum gets smeared out, as it can be observed for the 274.1 nm SSL. It can be stated from these measurements and the DLS results that the polydispersity degree rises for increasing liposomal sizes. Besides, non-PEGylated liposomes show slightly broader size distributions than SSLs.

Focusing on the high  $q$ -region of the single-contrast SAXS curves as displayed in figure 6.11, the scattering feature related to the phospholipid bilayer structure is observed. For Unilamellar Vesicles (ULV), the feature shape is typically round with a maximum around  $q = 0.86 \text{ nm}^{-1}$  Varga *et al.* (2012), related to a distance of 7.3 nm, as it can be seen in the case of small PEGylated liposomes. For SSLs extruded with larger pores, the bilayer shape shows incipient Bragg peaks which suggest the simultaneous presence of Multilamellar Vesicles (MLV) with unilamellar SSLs. Nevertheless, the MLV population cannot exceed 10 % of the total liposomes Sakuragi *et al.* (2011), as the scattering contribution from ULV is still clearly dominant.

However, the bilayer feature of the plain liposomes differs completely from the round shape visible in unilamellar vesicles. The diffraction peaks appearing at  $q_1 = 0.88$  and  $q_2 = 1.9 \simeq 2q_1 \text{ nm}^{-1}$  correspond to a slightly smaller lamellar repeat distance of 7.1 nm and the narrow shape of the bilayer feature indicates a variation of the phospholipid bilayer form factor. This change in the bilayer is emphasized for larger vesicles, as observed for the 127.7 plain liposome.

The effect of PEGylation induces a higher membrane stability due to the sterical stabilization of the liposome and the reduction of the electrostatic interactions within the phospholipid bilayer. The electrostatic repulsion in the non-PEGylated membrane is revealed by the appearance of the Bragg peaks in the plain liposomes. Nevertheless, secondary populations of MLVs coexisting with unilamellar liposomes can be observed for large extrusion pore sizes. In conclusion, the size and composition of the liposomes affect remarkably the formation of unilamellar vesicles and the shape of the phospholipid bilayer.

The quasi Bragg-peak in case of MLVs comes from the periodic structure of the phospholipid bilayer and water layers. It is because of the van der Waals attraction (more precisely the sum of electrostatic, van der Waals, and hydration terms of the interaction potential has a minimum at the observed periodic distance).

The PEG-lipid increases the negative charge of the bilayer in comparison to plain liposomes.

You wrote about "second population of MLVs" around this paragraph. In fact it is a distribution of uni, bi- and oligolamellar liposomes (OLV is a better term here than MLV). So I wouldn't use "second population".

The behavior of the different liposomal structures to osmotic stress can be examined with a continuous contrast variation experiment using sucrose as contrast agent, similarly to the measurements with the Caelyx sample in section 6.3.1. The scattering curves measured for a PEGylated liposome with size 81.4 nm are displayed in figure 6.12, where the solvent osmolality has been increased until 1409 mOsm  $\text{kg}^{-1}$  using a maximum sucrose mass fraction of 27.3 %. From the low  $q$ -region of these scattering curves some facts can be extracted which reveal preliminary the structural changes of the liposome induced by the osmotic pressure applied.

The curves do not intersect clearly in one point, even for low sucrose concentrations as occurred in the Caelyx case. The absence of an evident isoscattering point can be related with the relatively high polydispersity of the sample or the shape variation of the liposome already at small osmotic pressures. However, a diffuse intersection point, or pseudo isoscattering point Kawaguchi (2004), is visible at  $q = 0.18 \text{ nm}^{-1}$ . In analogy to figure 6.7b, the intensity of the pseudo  $q^*$  as a function of the solvent osmolality is depicted in figure 6.13, where the deviation from the original intensity

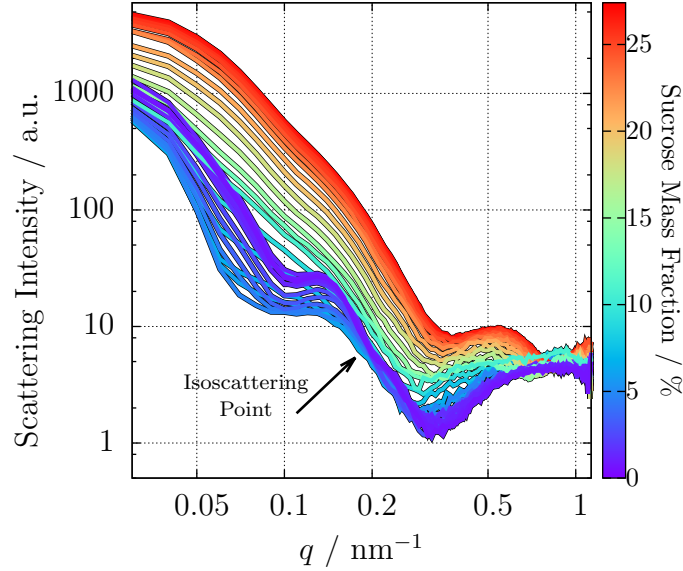


Figure 6.12: Scattering curves of the 81.4 nm SSL measured at different solvent osmolalities with an aqueous sucrose density gradient. The position of the pseudo isosscattering point at  $q = 0.18 \text{ nm}^{-1}$  is marked.

at  $q^*$  is shown for a plain and a PEGylated liposome.

The intensity at  $q^*$  starts diverging from the original value already at very low solvent osmolalities and reflects the continuous change in shape or size of the liposome when increasing the osmotic pressure. This behavior occurs for both SSLs and plain liposomes and suggest that a sharp osmotic threshold, like in the Caelyx case, does not exist. Thus, the response of liposomes to osmotic pressure is steady and is already apparent at low osmolalities.

Besides, an evident variation of the scattering curves below  $q \leq 0.3 \text{ nm}^{-1}$  is observed in figure 6.12 when increasing the solvent osmolality. For example, the minimum originally appearing at  $0.1 \text{ nm}^{-1}$  shifts slightly to larger  $q$ -values and disappears almost completely for high sucrose concentrations. This variation of the form factor is directly related with the flattening of the liposomal shape observed with Freeze-fracture TEM Varga *et al.* (2014). Due to the increased osmotic activity, the original spherical liposome shrinks into an oblate spheroid. This hypothesis can be further explored by focusing on the scattering feature related to the phospholipid bilayer at the high  $q$ -region.

For this purpose, the bilayer feature of the 178.9 nm PEGylated liposome is shown in figure 6.14a for increasing solvent osmolalities. The scattering curves were



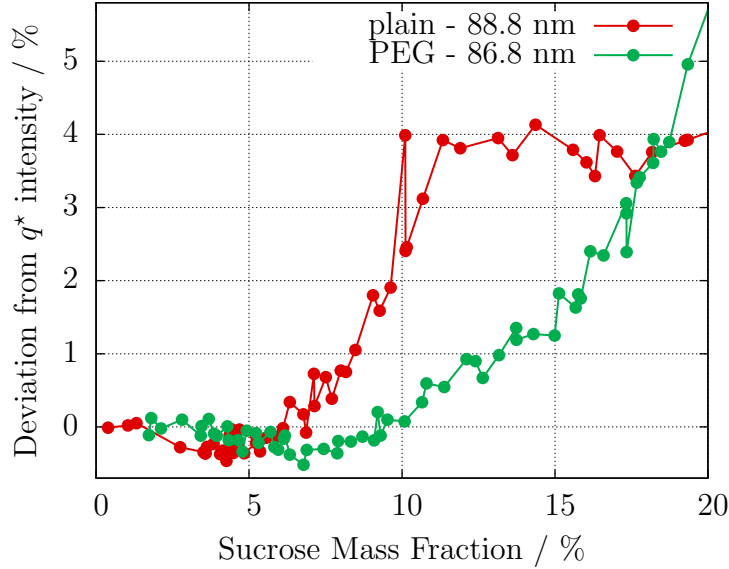


Figure 6.13: Isoscattering point intensity: Deviation from the initial intensity at  $q^*$  at different solvent osmolalities measured for a PEGylated and plain liposome of similar sizes. A clear osmotic threshold can not be observed.

measured with sucrose concentrations  $\leq 10$  % to avoid undesired contrast effects, because the average electron density of the phospholipid bilayer is ca.  $348 \text{ nm}^{-3}$ , which corresponds to a sucrose mass fraction of  $\sim 12$  %. Indeed, the bilayer form factor shows undesired, large contrast effects for solvent densities close to the average density of the membrane, i.e. match point, as already observed in figure 6.12, where the bilayer feature shifts abruptly to smaller  $q$ -values for sucrose concentrations above 15 %. The convolution of the contrast-related effects with the variations induced by the osmotic pressure demands a more challenging evaluation, can prevent the right interpretation of the data and is, thus, unwanted.

The original double-peak structure of the SSL at 0 % sucrose concentration observed in figure 6.14a transforms upon increasing the solvent osmolality and splits into 3 peaks of decreasing intensity at  $q_1 = 0.48 \text{ nm}^{-1}$ ,  $q_2 = 0.86 \text{ nm}^{-1}$  and  $q_3 = 1.28 \text{ nm}^{-1}$ . These Bragg peaks superimposed on the bilayer form factor reveal a periodic structure which can be related with a partial oligolamellar structure in the liposome system Fernandez *et al.* (2008). The 3 mentioned diffraction peaks translate into a lamellar repeat distance of ca. 13 nm, approximately doubling the thickness of the single phospholipid bilayer Kenworthy *et al.* (1995) and suggesting the appearance of a bilamellar structure Demé *et al.* (2002).

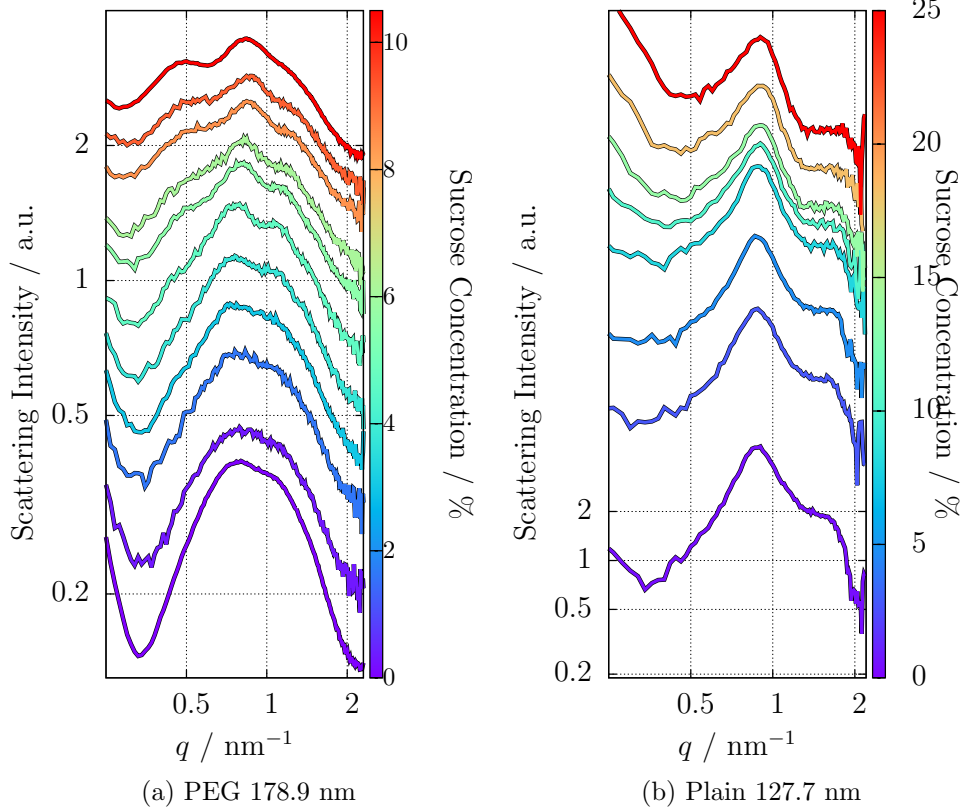


Figure 6.14: Osmotic effects in the phospholipid bilayer: Scattering curves measured at different solvent osmolalities for a 178.9 nm SSL and a 127.7 nm plain liposome. The appearance of Bragg peaks in the SSL membrane contrasts with the unaltered shape of the bilayer in the plain liposome.

The transition between a single bilayer phase and a bilamellar phase at 10 % sucrose concentration supports the hypothesis already presented that the liposome shrinks into lens-shaped vesicles due to the osmotic pressure. The bilamellar structure might arise from the close bilayer contacts at the outest part of the elliptical liposomes, while the single bilayer conformation still remains dominant in the mid-section of the liposomes. A similar morphology has been observed after the osmotic shrinkage of DPPC/DSPE-PEG<sub>2000</sub> vesicles Terreno *et al.* (2009). In fact, this behavior was identical for all 5 studied PEGylated liposomes, independent of their size.

Besides, the changes of the phospholipid bilayer form factor are smooth upon increasing the osmotic pressure as shown in figure 6.15, where the bilayer feature

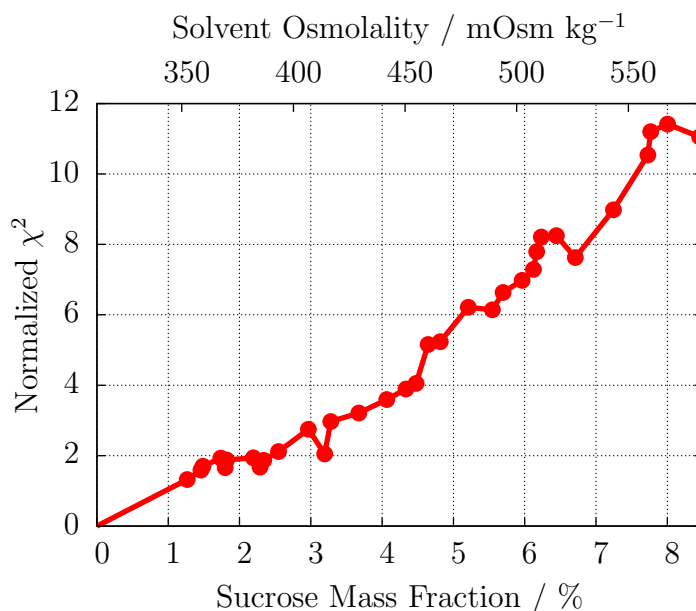


Figure 6.15: Variation of the 274.1 nm SSL bilayer scattering feature for increasing solvent osmolalities: normalized difference of the scattering curves at a certain sucrose concentration and in buffer. There are no sharp transitions, thus the osmotic effect is continuously modifying the bilayer structure.

scattering for increasing sucrose concentration is compared to the scattering curve of the SSL in buffer. This validates the observation from figure 6.13 and confirms that the increasing solvent osmolality affects continuously the structure of the liposomes and not as abruptly as in the case of Caelyx.

Contrarily, the phospholipid bilayer of the plain liposomes remains invariable upon increasing the solvent osmolality until 1285 mOsm kg<sup>-1</sup>, as displayed in figure 6.14b. This suggests that the MLV structure of the non-PEGylated vesicles increase their resilience and the multiple phospholipid bilayers strengthen the elastic modulus of the liposome membrane.

The fact that the incorporation of PEG moieties influences already the preparation and formation of the liposomes prevents a proper comparison of the osmotic effects between SSLs and plain liposomes. In fact, the existence of MLVs for non-PEGylated liposomes acts as a limiting factor for the osmotic activity. This contrasts with the osmotic effects observed in SSLs already at low sucrose concentrations which shrinks the PEGylated liposomes into oblated ellipsoids.

Although the chemical effect of sucrose on the SSL membrane can be discussed, previous studies in this subject Kiselev *et al.* (2003, 2001*b*, *a*), the large size of the su-

crose molecule and similar results with other experiments performed with salt Varga *et al.* (2014) validate this approach. The study of the osmotic activity of liposomes can be performed successfully using aqueous sucrose and shows very distinguishable effects for ULV (PEGylated liposomes) and MLV (plain liposomes).

## 6.4 Sizing of blood plasma components

From a nanoscience point of view, human blood can be seen as a suspension of particles with different physiological roles. Serum lipoproteins are the colloidal particles involved in the transport and metabolism of insoluble lipids and are among the most studied biological particles. The interest in their activity is understandable due to their direct relationship with very extended diseases in the Western world population, such as morbidity or atherogenesis, e.g. obturation of the arterial walls. For example, the dysregulation of cholesterol in plasma, primarily carried within lipoproteins, is responsible of atherosclerosis Munro & Cotran (1988). Besides, they are a convenient model for lipid-protein interactions Assmann & Brewer (1974) due to their lipid core and the hydrated proteins isometrically situated on its surface.

Lipoproteins are normally classified by the density range within they are isolated from blood plasma by ultracentrifugation Havel *et al.* (1955), showing different chemical composition, size and pathological condition for each class German *et al.* (2006). Indeed, the size of lipoproteins is critically connected with disease risk Gardner CD *et al.* (1996) and Low-density Lipoproteins (LDL) are suggested to be more or less atherogenic depending on their size Dreon *et al.* (1994). The effect of diabetes on the lipoprotein size is also of great interest, specially the sex-dependency of High-density Lipoproteins (HDL) size Colhoun *et al.* (2002).

Therefore, precise sizing techniques are a crucial tool to understand the physiological processes of lipoproteins German *et al.* (2006). The naturally narrow size distributions of LDL and HDL suggest small-angle scattering as a well-suited method and their heterogenous morphology advises the use of a contrast variation approach. For instance, the first characterization attempts date back to the late 1970s with neutron scattering Stuhrmann *et al.* (1975), using salt Tardieu *et al.* (1976) and sucrose Müller *et al.* (1978) as SAXS contrast agents or modifying the sample temperature Laggner *et al.* (1977); Luzzati *et al.* (1979).

The complicated inner structure of the lipoproteins revealed in more recent studies Baumstark *et al.* (1990); Schnitzer & Lichtenberg (1994) encourages the use of parameter-independent and model-free analysis of the scattering data. With this objective, LDL and HDL samples were measured with continuous contrast variation in SAXS using 40 % sucrose mass fraction to increase the solvent electron density

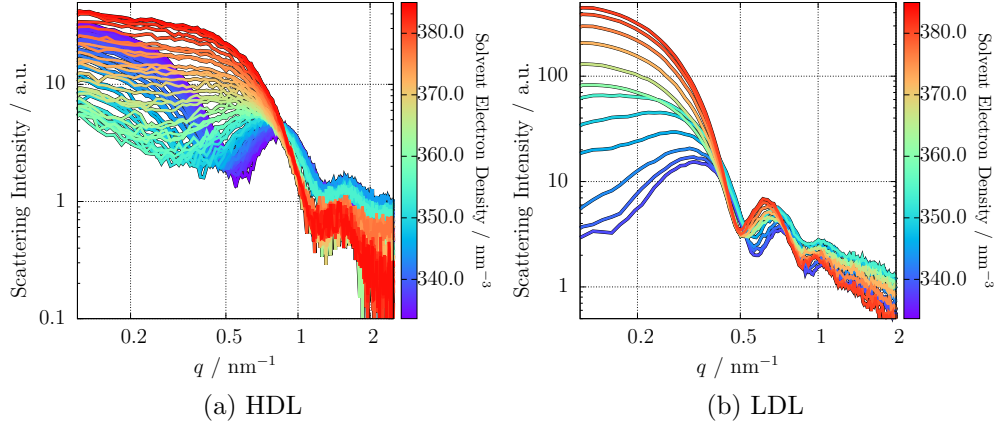


Figure 6.16: Scattering curves of HDL and LDL measured at different solvent densities by using an aqueous sucrose density gradient.

until  $384 \text{ nm}^{-3}$ . The scattering curves obtained for HDL and LDL are presented in figures 6.16a and 6.16b respectively.

In the case of HDL in buffer, the first minimum appears at  $q \approx 0.5 \text{ nm}^{-1}$  as already observed in figure 6.2. By increasing the solvent density, this minimum shifts to smaller  $q$ -values hinting the denser composition of the protein shell in comparison to the lighter lipid and cholesterol core. A lighter core morphology is also expected for LDL Luzzati *et al.* (1979) and it agrees with the contrast effect observed in the scattering curves displayed in figure 6.16b.

The appearance of so many minima indicates the narrow size distributions of both samples, providing the ideal conditions to use the isoscattering point  $q^*$  approach. The relative standard deviation as a function of  $q$  calculated for both lipoproteins is shown in figure 6.17a, where the minima correspond to the position of  $q_i^*$ . The clear minimum for HDL is located at  $q^* = 0.826 \text{ nm}^{-1}$ , corresponding to an impenetrable size for the solvent of 11 nm. The position of the first  $q^*$  in LDL is shifted to smaller  $q$ ,  $q^* = 0.42 \text{ nm}^{-1}$ , which translates into a solvent-excluded diameter of 21 nm.

Considering that the lipoproteins are quasi-spherical Stuhrmann *et al.* (1975), these results can be compared to those extracted from literature. The different cholesterol transport necessities reflect into a large variety of HDL subclasses with a size range between 7 and 13 nm German *et al.* (2006). For example, a size of 13 nm was observed for the HDL3 subfraction Tardieu *et al.* (1976), which deviates only 15 % from the result measured in our study. Difficulties to know the measured subclass of HDL hinders a more thorough comparison.

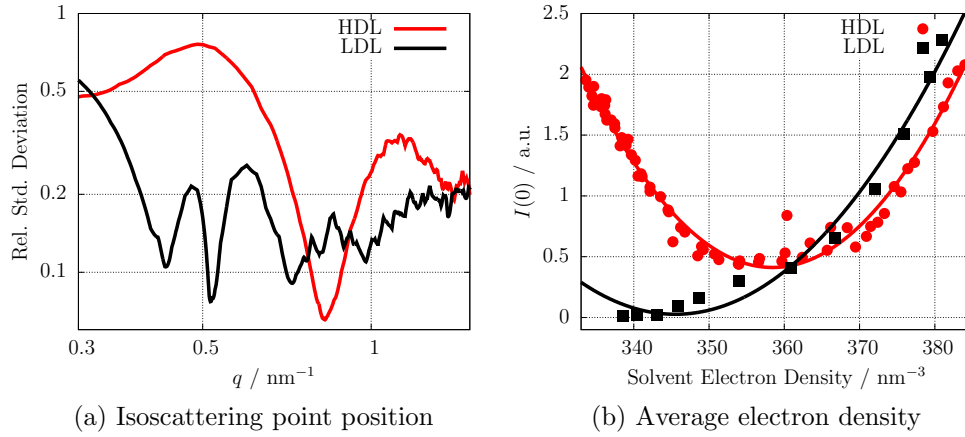


Figure 6.17: Comparison of the model free approaches for HDL (red) and LDL (black)

In the case of LDL, several studies provide diameters between 21 and 28 nm Tardieu *et al.* (1976); Colhoun *et al.* (2002); German *et al.* (2006), though the most repeated values lay around 22-23 nm Müller *et al.* (1978); Luzzati *et al.* (1979), less than 10 % deviation from our result. Nevertheless, the possible solvent penetration into the outer layers of LDL Stuhrmann *et al.* (1975); Tardieu *et al.* (1976) calls for caution as the size obtained from the  $q^*$  position considers an impenetrable particle.

The effects of permeability and protein hydration might be related to the density of the lipoprotein, which is the most identifying property of each lipoprotein class. As described previously, the intensity at zero-angle is related to the average electron density by the expression [REF EQ](#) and can be measured. The experimental  $I(q = 0)$  values are depicted in figure 6.17b, where the fit of the previous equation is shown as a solid line.

According to the analytical fit, the average density of HDL is  $358.4 \text{ nm}^{-3}$  and the density measured in the LDL case is ca.  $345 \text{ nm}^{-3}$ . In the latter, the low number of points increases the inaccuracy of the result, although the value is still in pretty good agreement with other SAXS studies Tardieu *et al.* (1976); Luzzati *et al.* (1979). The protein-rich ( $\sim 50 \%$ ) structure of HDL explains its higher density in comparison to LDL, composed mainly of lipids ( $\sim 80 \%$ ).

Another model-free interpretation of the HDL scattering data is presented in figure 6.18, where the the squared radius of the Guinier region is presented as a function of the solvent electron density. As previously shown, the analytical expression [REF EQ](#) can be fitted to the experimental data, resulting in an average electron density  $\rho_0 = 353.6 \text{ nm}^{-3}$  and a particle shape radius of  $R_c = 6 \text{ nm}$ . The size obtained with

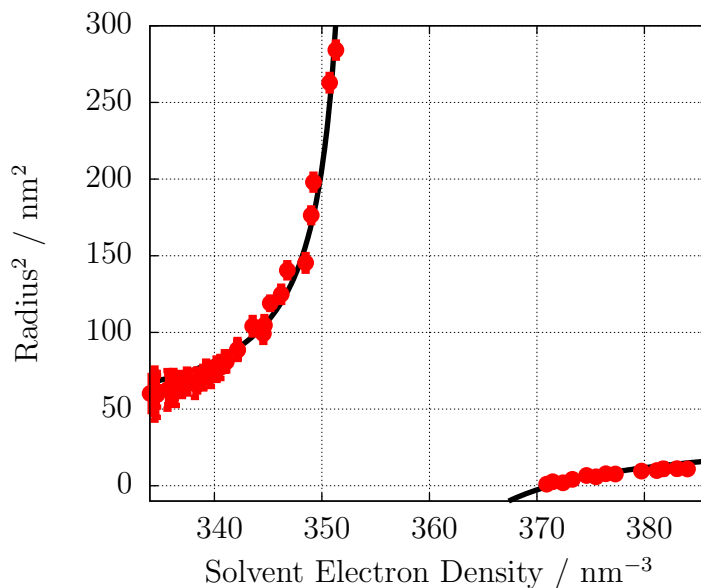


Figure 6.18: Squared radius of the HDL scattering data. The analytical fit results in an average density of  $353.6 \text{ nm}^{-3}$  and an external diameter of 12 nm.

this approach, 12 nm, is consistent with the previous result. Probably because of the absence of relevant experimental points around the match point, the average density differs in almost  $5 \text{ nm}^{-3}$  from the  $I(0)$  result.

The continuous contrast variation technique and the subsequent model-free analysis are easy and effective tools to measure the size and density of lipoproteins, very important attributes to understand the biological processes related to cholesterol and lipid transport. A more detailed analysis and modelling of the scattering data could have addressed some issues such as the hydration and distribution of the proteins on the surface, the permeability of the steric and lipid core or the radial distribution of cholesterol and triglycerides in the lipoprotein. However, the focus of our study was principally on the most distinctive traits of the lipoprotein classes: density and size.

## 6.5 Protein-coated low-density nanoparticles

The most recent efforts in nanomedicine aim for a high control of the nanocarrier surface, as the surface's properties are a defining element of its efficiency as drug carrier. Besides, nanoparticles interact with proteins when introduced into biological media, leading to the formation of the so-called *protein corona* surrounding the

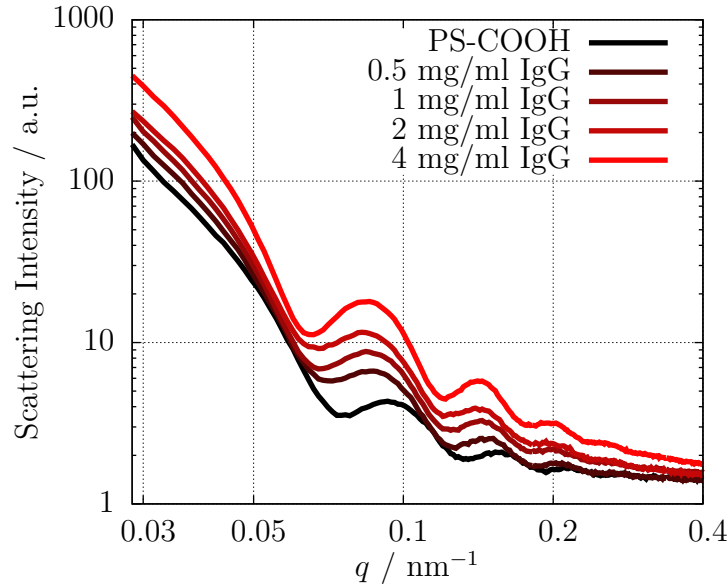


Figure 6.19: SAXS curves at a single contrast of PS-COOH particles coated with IgG at different concentrations.

nanocarrier Cedervall *et al.* (2007); Monopoli *et al.* (2011); Casals *et al.* (2010). The identity of the biomolecule coating depends on the particle size, surface functionalization and charge Lundqvist *et al.* (2008); Tenzer *et al.* (2013); Gessner *et al.* (2003) and its detailed description is challenging. Yet, the ability to quantitatively characterise this interface is important in understanding particle behaviour in these complex environments and improving their surface engineering for enhanced functionality.

Immunoglobulin G (IgG) is the most common type of antibody found in human serum and, therefore, a logical candidate to coat the studied nanoparticles with. In this case, we used commercially available PS-COOH particles, because polystyrene is a frequent material in nanomedicine strategies and has a wide variety of possible surface functionalizations. The carboxylated surface prevents the agglomeration of the particles and also provides a chemical anchor for the protein binding. The use of SAXS to obtain a quantitative description of the protein corona is examined for different IgG concentrations, e.g. shell thicknesses, and compared with DLS and DCS Minelli *et al.* (2014).

The bare PS-COOH particles are highly charged, showing a  $\zeta$ -potential of  $(-49 \pm 1)$  mV, which is drastically reduced to around  $-10$  mV following the binding of the positively charged IgG. The SAXS measurements of the IgG-coated particles with different protein concentrations are shown in figure 6.19, where a clear shift to



Table 6.1: Concentration of IgG incubated with PS-COOH particles and IgG shell thickness as measured by single-contrast SAXS, DCS and DLS Minelli *et al.* (2014). A double-shell model with sharp interfaces was used for the SAXS results. The uncertainties are the standard deviations of repeated measurements.

$\rho_{IgG}$ / <b>mg mL<sup>-1</sup></b>	<b><math>\zeta</math>-potential / mV</b>	<b><math>T_{DLS}</math> / nm</b>	<b><math>T_{DCS}</math> / nm</b>	<b><math>T_{SAXS}</math> / nm</b>
0.5	$-10.8 \pm 0.9$	$10 \pm 1$	$3.7 \pm 0.6$	$7.7 \pm 1.4$
1	$-10.7 \pm 0.6$	$11 \pm 2$	$5.9 \pm 0.5$	$8.4 \pm 1.4$
2	$-9.6 \pm 0.5$	$12 \pm 2$	$7.6 \pm 0.4$	$9.6 \pm 1.5$
4	$-9.7 \pm 0.5$	$15 \pm 2$	$8.3 \pm 0.4$	$9.6 \pm 1.5$

smaller  $q$ -values is observed for increasing concentration of IgG. This effect is clearly related with the increase in size for higher IgG concentration, although a quantitative description is complicated.

Due to the core-shell morphology of the polymeric bare particle (see **PREVIOUS SECTION**), SAXS curves were analyzed using a double-shell model (see **EXPRESSION IN SECTION**), considering a sharp interface between the different components and a constant thickness and density of the IgG corona. In order to focus on the total diameter instead of the details of the internal structure, the limits of the inner and outer radii of the polymer shell are not fixed and are treated as fitting parameters together with the outer radius and the contrast difference of each shell with the polystyrene core.

The IgG shell thickness obtained for IgG-coated particles with different protein concentrations is shown in table 6.1 and compared to the size measurements performed with other techniques. All DLS, DCS and SAXS techniques show an increase in the IgG-shell thickness with increasing concentration of the protein in solution during incubation. As expected, DLS provides higher values than the other techniques, as the measured thickness is related to the hydrodynamic properties of the system.

Although all techniques show an increase of the IgG shell thickness with increasing concentration of the protein, full consistency among them requires further refinements of the SAXS and DCS modelling. For instance, the SAXS evaluation has neglected the possible spatial heterogeneity and hydration of the IgG corona and the model employed for the core particle overestimates the size in almost 10 % Minelli *et al.* (2014); Garcia-Diez *et al.* (2015).

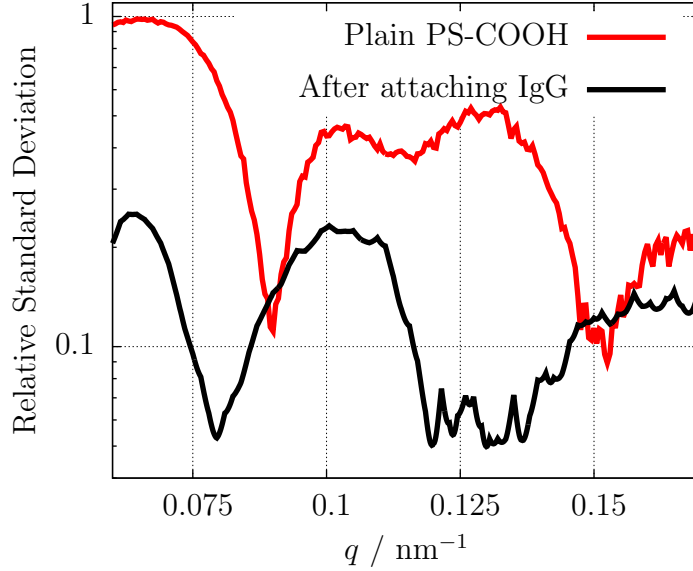


Figure 6.20: Isoscattering point position before and after attaching IgG ( $4 \text{ mg mL}^{-1}$ ) to the PS-COOH particles. A shift of the first minimum to lower  $q$ -values is observed after attaching the biotarget to the nanoparticle.

### 6.5.1 Hard protein corona characterization with contrast variation

The possible inaccuracies arising from the previous modelling approach might be prevented by using continuous contrast variation and a model-free evaluation. For this purpose, the protein-coated particle with  $4 \text{ mg mL}^{-1}$  IgG was introduced in a density gradient with sucrose as contrast agent, resulting in an increase of the solvent electron density until  $350.8 \text{ nm}^{-3}$  at the maximum sucrose concentration of 14.7 %. As **DISCUSSED BEFORE**, the isoscattering point position is quantified by calculating the relative standard deviation of the 20 measured curves at each  $q$ , as depicted in figure 6.20. This value becomes minimal at  $q = 0.0795 \pm 0.0019 \text{ nm}^{-1}$ .

By comparing the relative standard deviation curves of the bare PS-COOH particle Garcia-Diez *et al.* (2015) and the IgG-coated sample (figure 6.20), it is noticeable that the position of the minimum is shifted to smaller  $q$ -values after attaching the bioprobe to the surface as a consequence of the increase in size. The diameter increase  $t$  can be quantified by inserting the isoscattering positions before and after the target attachment,  $q^* = 0.0900 \text{ nm}^{-1}$  and  $q_{IgG}^* = 0.0795 \text{ nm}^{-1}$  respectively, in the equation already discussed in section **EQUATION OF ISOSCATTERING POINT**,

Table 6.2: Uncertainty contributions associated to the isoscattering point  $q^*$  position, where  $u_I$  and  $u_r$  correspond to the input uncertainty and relative uncertainty respectively.

Input quantity	$u_I$	$u_r$	Contribution
Photon Energy	0.8 eV	$10^{-4}$	$0.000008 \text{ nm}^{-1}$
Sample-detector distance	5 mm	$10^{-3}$	$0.00008 \text{ nm}^{-1}$
Pixel size	$0.2 \text{ }\mu\text{m}$	$10^{-3}$	$0.00008 \text{ nm}^{-1}$
Center determination	n.a.	n.a.	$0.0008 \text{ nm}^{-1}$
$q$ -bin size	$0.0015 \text{ nm}^{-1}$	$2 \cdot 10^{-2}$	$0.0015 \text{ nm}^{-1}$
Solvent background	n.a.	n.a.	$0.0009 \text{ nm}^{-1}$
<b>Combined standard uncertainty</b>			<b><math>0.0019 \text{ nm}^{-1}</math></b>

TANQR=QR:

$$t = R_{IgG} - R = \frac{K_1}{q_{IgG}^*} - \frac{K_1}{q^*}, \quad (6.1)$$

where  $K_1$  is a factor which depends slightly on the particle polydispersity and sphericity (typically  $K_1 = 4.493$ ),  $t$  is the IgG-shell thickness and  $R$  and  $R_{IgG}$  are the particle radii before and after IgG incubation. This results in a shell thickness of  $(6.6 \pm 1.9) \text{ nm}$ .

It is important to highlight that this result corresponds to the volume inaccessible for the solvent (section **theory contrast variation**) and, thus, it can be identified with the hard protein corona surrounding the polymeric nanoparticle. This assumption agrees with the larger values found with other methods in table 6.1, which probe the permeable part of the IgG shell as well. The hard corona has a thickness of  $(6.6 \pm 1.9) \text{ nm}$ , around 2 nm thinner than the complete protein layer.

### Uncertainty analysis

The associated uncertainty to the isoscattering point position  $q^*$  of  $0.0019 \text{ nm}^{-1}$  depends on the chosen  $q$ -bin size, the correction of the background contributions from the solvent Garcia-Diez *et al.* (2015), the energy resolution of the photon beam Krumrey & Ulm (2001), the accuracy of the distance between the irradiated sample and the scattering detector, the detector pixel size Werneck *et al.* (2014) or the determination of the scattering center. Each contribution to the uncertainty budget has been detailed in table 6.2, where the contribution of the selected  $q$ -bin size is the largest. The uncertainties given are standard uncertainties ( $k = 1$ )

The uncertainty associated to the thickness of the protein layer  $t$  produces a limit

of detection of 1.9 nm, which arises from the previously discussed  $q^*$  uncertainty and an uncertainty of 10 % associated with the particle polydispersity and reflected in  $K_1$ . From the expression 6.1, the thickness uncertainty  $\delta t$  can be derived as:

$$\delta t^2 = \left( t \frac{\delta K_1}{K_1} \right)^2 + \left( \frac{K_1}{(q_{IgG}^*)^2} \delta q_{IgG}^* \right)^2 + \left( \frac{K_1}{(q^*)^2} \delta q^* \right)^2 \quad (6.2)$$

where  $\delta q_{IgG}^* = \delta q^* = 0.0019 \text{ nm}^{-1}$ .

## 6.6 Summary

The results presented in this section demonstrate that it is possible to determine the size of complicated nanoparticles relevant in nanomedicine with continuous contrast variation in SAXS. This technique has been used to characterize a great variety of systems in the nanoscale such as the PEGylated liposomal nanodrug Caelyx®, empty liposomal nanocarriers, human lipoproteins or protein-coated polymeric nanoparticles.

In the case of Caelyx®, by means of an iso-osmolal density gradient, the position of the isoscattering point was measured whereby the size of the liposomal drug was determined with this model-free approach. Supplemented by the model fitting of the so called *shape factor* of the liposomes, the size was also obtained from an independent evaluation procedure and an average size of  $(69 \pm 5) \text{ nm}$  was obtained. This size is smaller than the value measured by DLS, which can be attributed to the fact that the contrast variation SAXS determines the size of the liposomes impermeable to the contrast agent, i.e. the outer PEG layer of the liposomes is not probed. The latter implies that the combination of SAXS with DLS can reveal the difference between the hydrodynamic diameter and the "core" size of the nanocarrier, which is related to the thickness of the PEG-layer in case of stealth liposomes. Moreover it is shown that by means of the shape factor fitting, complementary information about the shape of the nanocarrier can be obtained. Complementary, it was found that the average electron density of the liposomal doxorubicin was higher than that of the empty PEGylated liposomes.

Besides, using an aqueous sucrose density gradient, it was possible to study the behavior of the liposomal drug carrier under different osmotic conditions. It was shown that an increasing osmolality of the buffer produces an osmotic shrinkage of the liposomal structure, although this structural deformation is reversible and does not affect the crystalline structure of the intraliposomal doxorubicin.

For comparison purposes with the liposomal doxorubicin system, the osmotic activity of empty liposomes was also investigated using aqueous sucrose. The distinguishable osmotic effects observed in PEGylated and plain liposomes arise from the different formation of the liposomes, which is influenced by the presence of PEG moieties in the preparation. The MLV structure of the plain liposomes show higher resilience against osmotic pressure than the unilamellar membrane of the PEGylated vesicles. In the latter, the ULV structure shrinks due to the osmotic pressure and deforms the liposomes into obloid ellipsoids, creating a bilamellar structure at the outermost part of the vesicles.

The continuous contrast variation technique was used to determine the most distinctive traits of human lipoproteins: size and density, the latter being fundamental to classify them. The parameters obtained by means of a model-free analysis are in good agreement with the reported values in literature.

Finally, the application of the technique on nanoparticles incubated in different concentrations of IgG reveals the difference between the IgG-shell and the hard protein-corona impenetrable for the solvent, probed with contrast variation SAXS. In addition, the use of complementary techniques such as DLS, SAXS and DCS show an increase of the protein-shell thickness with increasing concentration of the proteins during incubation. The SAXS contribution to this study requires of a model refinement for full consistency with the results measured for the bare PS-COOH particle.

# Bibliography

- AMENITSCH, H., BERNSTORFF, S., KRIECHBAUM, M., LOMBARDO, D., MIO, H., RAPPOLT, M. & LAGGNER, P. 1997 Performance and First Results of the ELETTRA High-Flux Beamline for Small-Angle X-ray Scattering. *Journal of Applied Crystallography* **30**, 872–876.
- ARNOLD, M. S., GREEN, A. A., HULVAT, J. F., STUPP, S. I. & HERSAM, M. C. 2006 Sorting carbon nanotubes by electronic structure using density differentiation. *Nat. Nano.* **1**, 60–65.
- ASSMANN, G. & BREWER, H. B. 1974 Lipid-protein interactions in high density lipoproteins. *Proceedings of the National Academy of Sciences* **71**, 989–993.
- AVDEEV, M. V. 2007 Contrast variation in small-angle scattering experiments on polydisperse and superparamagnetic systems: basic functions approach. *Journal of Applied Crystallography* **40**, 56–70.
- BALLAUFF, M. 2001 SAXS and SANS studies of polymer colloids. *Curr. Opin. Colloid Interface Sci.* **6**, 132–139.
- BALLAUFF, M. 2011 Analysis of Polymer Colloids by Small-Angle X-Ray and Neutron Scattering: Contrast Variation. *Adv Eng Mater* **13**, 793–802.
- BALLAUFF, M., BOLZE, J., DINGENOUTS, N., HICKL, P. & PÖTSCHKE, D. 1996 Small-angle X-ray scattering on latexes. *Macromol Chem Phys* **197**, 3043–3066.
- BARENHOLZ, Y. 2001 Liposome application: problems and prospects. *Current Opinion in Colloid & Interface Science* **6**, 66–77.
- BARENHOLZ, Y. C. 2012 Doxil® — The first FDA-approved nano-drug: Lessons learned. *Journal of Controlled Release* **160**, 117–134.

- BAUMSTARK, M. W., KREUTZ, W., BERG, A., FREY, I. & KEUL, J. 1990 Structure of human low-density lipoprotein subfractions determined by X-ray small-angle scattering. *Biochimica et Biophysica Acta (BBA)-Protein Structure and Molecular Enzymology* **1037**, 48–57.
- BEIJA, M., SALVAYRE, R., LAUTH-DE VIGUERIE, N. & MARTY, J.-D. 2012 Colloidal systems for drug delivery: from design to therapy. *Trends Biotechnol* **30**, 485–496.
- BELL, N. C., MINELLI, C., TOMPKINS, J., STEVENS, M. M. & SHARD, A. G. 2012 Emerging Techniques for Submicrometer Particle Sizing Applied to Stöber Silica. *Langmuir* **28**, 10860–10872.
- BERBERAN-SANTOS, M. N., BODUNOV, E. N. & POGLIANI, L. 1997 On the barometric formula. *Am. J. Phys.* **65**, 404–412.
- BEYER, D., LEBEK, W., HERGETH, W.-D. & SCHMUTZLER, K. 1990 SAXS study of core-shell colloids. *Colloid Polym Sci* **268**, 744–748.
- BLANTON, T. N., HUANG, T. C., TORAYA, H., HUBBARD, C. R., ROBIE, S. B., LOUËR, D., GÖBEL, H. E., WILL, G., GILLES, R. & RAFTERY, T. 1995 JCPDS—International Centre for Diffraction Data round robin study of silver behenate. A possible low-angle X-ray diffraction calibration standard. *Powder Diffraction* **10**, 91–95.
- BLUMENTHAL, G. R. & GOULD, R. J. 1970 Bremsstrahlung, Synchrotron Radiation, and Compton Scattering of High-Energy Electrons Traversing Dilute Gases. *Rev. Mod. Phys.* **42**, 237–270.
- BOLZE, J., BALLAUFF, M., KIJLSTRA, J. & RUDHARDT, D. 2003 Application of Small-Angle X-Ray Scattering as a Tool for the Structural Analysis of Industrial Polymer Dispersions. *Macromol. Mater. Eng.* **288**, 495–502.
- BOLZE, J., BALLAUFF, M., RISCHE, T., RUDHARDT, D. & MEIXNER, J. 2004 In situ Structural Characterization of Semi-Crystalline Polymer Latex Particles by Small-Angle X-Ray Scattering. *Macromol Chem Phys* **205**, 165–172.
- BOLZE, J., HÖRNER, K. D. & BALLAUFF, M. 1997 Small-angle X-ray scattering analysis of the radial structure of latex particles swollen by a nonpolar monomer. *Langmuir* **13**, 2960–2964.

- CABRAL, H. & KATAOKA, K. 2014 Progress of drug-loaded polymeric micelles into clinical studies. *J Control Release* **190**, 465–476.
- CALDWELL, K. D., JONES, H. K. & GIDDINGS, J. C. 1986 Measurement of the size and density of colloidal particles by combining sedimentation field-flow fractionation and quasi-elastic light scattering. *Colloid Surface* **18**, 123–131.
- CARNEY, R. P., KIM, J. Y., QIAN, H., JIN, R., MEHENNI, H., STELLACCI, F. & BAKR, O. M. 2011 Determination of nanoparticle size distribution together with density or molecular weight by 2D analytical ultracentrifugation. *Nat Commun* **2**, 335.
- CASALS, E., PFALLER, T., DUSCHL, A., OOSTINGH, G. J. & PUNTES, V. 2010 Time Evolution of the Nanoparticle Protein Corona. *ACS Nano* **4**, 3623–3632.
- CEDERVALL, T., LYNCH, I., LINDMAN, S., BERGGÅRD, T., THULIN, E., NILSSON, H., DAWSON, K. A. & LINSE, S. 2007 Understanding the nanoparticle–protein corona using methods to quantify exchange rates and affinities of proteins for nanoparticles. *Proc Natl Acad Sci U S A* **104**, 2050–2055.
- COLHOUN, H. M., OTVOS, J. D., RUBENS, M. B., TASKINEN, M. R., UNDERWOOD, S. R. & FULLER, J. H. 2002 Lipoprotein subclasses and particle sizes and their relationship with coronary artery calcification in men and women with and without type 1 diabetes. *Diabetes* **51**, 1949–1956.
- COOMBS, S. H. 1981 A density-gradient column for determining the specific gravity of fish eggs, with particular reference to eggs of the mackerel *Scomber scombrus*. *Mar. Biol.* **63**, 101–106.
- CULLITY, B. D. & STOCK, S. R. 2001 *Elements of X-Ray Diffraction*, 3rd edn. Upper Saddle River, NJ: Pearson.
- DE GIER, J. 1993 Osmotic behaviour and permeability properties of liposomes. *Chemistry and Physics of Lipids* **64**, 187–196.
- DEMÉ, B., DUBOIS, M., GULIK-KRZYWICKI, T. & ZEMB, T. 2002 Giant Collective Fluctuations of Charged Membranes at the Lamellar-to-Vesicle Unbinding Transition. 1. Characterization of a New Lipid Morphology by SANS, SAXS, and Electron Microscopy. *Langmuir* **18**, 997–1004.



- DINGENOUTS, N., BOLZE, J., PÖTSCHKE, D. & BALLAUFF, M. 1999 Analysis of Polymer Latexes by Small-Angle X-Ray Scattering. In *Polymer Latexes - Epoxy Resins - Polyampholytes* (ed. A. Abe), pp. 1–47. Berlin-Heidelberg: Springer Verlag.
- DINGENOUTS, N., KIM, Y. S. & BALLAUFF, M. 1994a The interface between immiscible polymers in composite latexes: a small-angle x-ray scattering study employing contrast variation. *Colloid Polym. Sci.* **272**, 1380–1387.
- DINGENOUTS, N., KIM, Y.-S. & BALLAUFF, M. 1994b Radial density distribution in core-shell latexes as revealed by small-angle X-ray scattering. *Macromol Rapid Comm* **15**, 613–617.
- DINGENOUTS, N., PULINA, T. & BALLAUFF, M. 1994c Structure of carboxylated latices as revealed by small-angle X-ray scattering. *Macromolecules* **27**, 6133–6136.
- DOSHI, N. & MITRAGOTRI, S. 2009 Designer Biomaterials for Nanomedicine. *Adv Funct Mater* **19**, 3843–3854.
- DREON, D. M., FERNSTROM, H. A., MILLER, B. & KRAUSS, R. M. 1994 Low-density lipoprotein subclass patterns and lipoprotein response to a reduced-fat diet in men. *FASEB J* **8**, 121–126.
- EGELHAAF, S. U., WEHRLI, E., MULLER, M., ADRIAN, M. & SCHURTENBERGER, P. 1996 Determination of the size distribution of lecithin liposomes: a comparative study using freeze fracture, cryoelectron microscopy and dynamic light scattering. *Journal of Microscopy* **184**, 214–228.
- ETHERIDGE, M. L., CAMPBELL, S. A., ERDMAN, A. G., HAYNES, C. L., WOLF, S. M. & MCCULLOUGH, J. 2013 The big picture on nanomedicine: the state of investigational and approved nanomedicine products. *Nanomedicine: Nanotechnology, Biology and Medicine* **9**, 1–14.
- EULISS, L. E., DUPONT, J. A., GRATTON, S. & DESIMONE, J. 2006 Imparting size, shape, and composition control of materials for nanomedicine. *Chem Soc Rev* **35**, 1095.
- FEIGIN, L. A. & SVERGUN, D. I. 1987 *Structure Analysis by Small-Angle X-Ray and Neutron Scattering*, 1st edn. New York: Plenum Press.

- FERNANDEZ, R. M., RISKE, K. A., AMARAL, L. Q., ITRI, R. & LAMY, M. T. 2008 Influence of salt on the structure of DMPG studied by SAXS and optical microscopy. *Biochimica et Biophysica Acta (BBA) - Biomembranes* **1778**, 907–916.
- FIELDING, L. A., MYKHAYLYK, O. O., ARMES, S. P., FOWLER, P. W., MITTAL, V. & FITZPATRICK, S. 2012 Correcting for a Density Distribution: Particle Size Analysis of Core–Shell Nanocomposite Particles Using Disk Centrifuge Photosedimentometry. *Langmuir* **28**, 2536–2544.
- FITZPATRICK, S. T. 1998 Structure and method for centrifugal sedimentation particle size analysis of particles of lower density than their suspension medium.
- GABIZON, A. & MARTIN, F. 1997 Polyethylene glycol-coated (pegylated) liposomal doxorubicin. Rationale for use in solid tumours. *Drugs* **54 Suppl 4**, 15–21.
- GARCIA-DIEZ, R., GOLLWITZER, C. & KRUMREY, M. 2015 Nanoparticle characterization by continuous contrast variation in small-angle X-ray scattering with a solvent density gradient. *Journal of Applied Crystallography* **48**, 20–28.
- GARCIA-DIEZ, R., GOLLWITZER, C., KRUMREY, M. & VARGA, Z. 2016 Size Determination of a Liposomal Drug by Small-Angle X-ray Scattering Using Continuous Contrast Variation. *Langmuir* **32**, 772–778.
- GARDNER CD, FORTMANN SP & KRAUSS RM 1996 Association of small low-density lipoprotein particles with the incidence of coronary artery disease in men and women. *JAMA* **276**, 875–881.
- GERMAN, J. B., SMILOWITZ, J. T. & ZIVKOVIC, A. M. 2006 Lipoproteins: When size really matters. *Curr Opin Colloid Interface Sci* **11**, 171–183.
- GESSNER, A., LIESKE, A., PAULKE, B.-R. & MÜLLER, R. H. 2003 Functional groups on polystyrene model nanoparticles: Influence on protein adsorption. *J. Biomed. Mater. Res.* **65A**, 319–326.
- GIDDINGS, J. C., KARAIKAKIS, G. & CALDWELL, K. D. 1981 Density and Particle Size of Colloidal Materials Measured by Carrier Density Variations in Sedimentation of Field-Flow Fractionation. *Separ Sci Technol* **16**.
- GRUNDER, R., KIM, Y. S., BALLAUFF, M., KRANZ, D. & MÜLLER, H.-G. 1991 Analysis of Polymer Lattices by Small-Angle X-Ray Scattering. *Angew Chem Int Edit* **30**, 1650–1652.

- GRUNDER, R., URBAN, G. & BALLAUFF, M. 1993 Small-angle x-ray analysis of latex particles with core-shell morphology. *Colloid Polym Sci* **271**, 563–572.
- GUINIER, A. 1939 Diffraction of X-rays of very small angles-application to the study of ultramicroscopic phenomena. *Ann. Phys.(Paris)* **12**, 161–237.
- GUINIER, A. & FOURNET, G. 1955 *Small-angle scattering of X-rays*. New York: Wiley.
- GUTERRES, S. S., ALVES, M. P. & POHLMANN, A. R. 2007 Polymeric Nanoparticles, Nanospheres and Nanocapsules, for Cutaneous Applications. *Drug Target Insights* **2**, 147–157.
- HALLETT, F. R., WATTON, J. & KRYGSMAN, P. 1991 Vesicle sizing. *Biophys J* **59**, 357–362.
- HARRIS, J. M. & CHESS, R. B. 2003 Effect of pegylation on pharmaceuticals. *Nature Reviews Drug Discovery* **2**, 214–221.
- HAVEL, R. J., EDER, H. A. & BRAGDON, J. H. 1955 THE DISTRIBUTION AND CHEMICAL COMPOSITION OF ULTRACENTRIFUGALLY SEPARATED LIPOPROTEINS IN HUMAN SERUM. *J Clin Invest* **34**, 1345–1353.
- HAYNES, W. M. 2012 *CRC Handbook of Chemistry and Physics*, 93rd edn. Philadelphia: Taylor & Francis Ltd.
- HENKE, B., GULLIKSON, E. & DAVIS, J. 1993 X-Ray Interactions: Photoabsorption, Scattering, Transmission, and Reflection at  $E = 50\text{--}30,000$  eV,  $Z = 1\text{--}92$ . *Atom. Data Nucl. Data* **54**, 181–342.
- HINTON, R. J. & DOBROTA, M. 1978 *Density Gradient Centrifugation*. Amsterdam: Elsevier.
- HOO, C. M., STAROSTIN, N., WEST, P. & MECARTNEY, M. L. 2008 A comparison of atomic force microscopy (AFM) and dynamic light scattering (DLS) methods to characterize nanoparticle size distributions. *J Nanopart Res* **10**, 89–96.
- JANS, H., LIU, X., AUSTIN, L., MAES, G. & HUO, Q. 2009 Dynamic Light Scattering as a Powerful Tool for Gold Nanoparticle Bioconjugation and Biomolecular Binding Studies. *Anal. Chem.* **81**, 9425–9432.

- JOENSSON, J. E. L., HASSANDER, H., JANSSON, L. H. & TOERNELL, B. 1991 Morphology of two-phase polystyrene/poly(methyl methacrylate) latex particles prepared under different polymerization conditions. *Macromolecules* **24**, 126–131.
- KAMITI, M., BOLDRIDGE, D., NDOPING, L. M. & REMSEN, E. E. 2012 Simultaneous Absolute Determination of Particle Size and Effective Density of Submicron Colloids by Disc Centrifuge Photosedimentometry. *Anal Chem* **84**, 10526–10530.
- KATTAN, J., DROZ, J.-P., COUVREUR, P., MARINO, J.-P., BOUTAN-LAROZE, A., ROUGIER, P., BRAULT, P., VRANCKX, H., GROGNET, J.-M., MORGE, X. & SANCHO-GARNIER, H. 1992 Phase I clinical trial and pharmacokinetic evaluation of doxorubicin carried by polyisohexylcyanoacrylate nanoparticles. *Invest. New Drugs* **10**, 191–199.
- KAWAGUCHI, T. 1993 The isoscattering point in X-ray scattering curves of globular solute particles measured by the contrast-variation method: the influence of additive penetration into the solute particles. *J. Appl. Cryst.* **26**, 214–218.
- KAWAGUCHI, T. 2004 Application of isoscattering points to the analysis of globular solute structures. *Crystallography Reviews* **10**, 233–246.
- KAWAGUCHI, T. & HAMANAKA, T. 1992 The isoscattering point in X-ray scattering curves of globular solute particles measured by the contrast-variation method. *Journal of Applied Crystallography* **25**, 778–784.
- KAWAGUCHI, T., HAMANAKA, T. & MITSUI, T. 1983 X-ray structural studies of some nonionic detergent micelles. *J Colloid Interf Sci* **96**, 437–453.
- KENWORTHY, A. K., HRISTOVA, K., NEEDHAM, D. & MCINTOSH, T. J. 1995 Range and magnitude of the steric pressure between bilayers containing phospholipids with covalently attached poly(ethylene glycol). *Biophys J* **68**, 1921–1936.
- KHORASANI, A. A., WEAVER, J. L. & SALVADOR-MORALES, C. 2014 Closing the gap: accelerating the translational process in nanomedicine by proposing standardized characterization techniques. *Int J Nanomedicine* **9**, 5729–5751.
- KISELEV, M. A., LESIEUR, P., KISSELEV, A. M., LOMBARDO, D., KILLANY, M. & LESIEUR, S. 2001a Sucrose solutions as prospective medium to study the vesicle structure: SAXS and SANS study. *Journal of Alloys and Compounds* **328**, 71–76.

- KISELEV, M. A., LESIEUR, P., KISSELEV, A. M., LOMBARDO, D., KILLANY, M., LESIEUR, S. & OLLIVON, M. 2001*b* A sucrose solutions application to the study of model biological membranes. *Nuclear Instruments and Methods in Physics Research Section A: Accelerators, Spectrometers, Detectors and Associated Equipment* **470**, 409–416.
- KISELEV, M. A., WARTEWIG, S., JANICH, M., LESIEUR, P., KISELEV, A. M., OLLIVON, M. & NEUBERT, R. 2003 Does sucrose influence the properties of DMPC vesicles? *Chemistry and Physics of Lipids* **123**, 31–44.
- KRATKY, O., PILZ, I. & SCHMITZ, P. J. 1966 Absolute intensity measurement of small angle x-ray scattering by means of a standard sample. *Journal of Colloid and Interface Science* **21**, 24–34.
- KRUMREY, M. & ULM, G. 2001 High-accuracy detector calibration at the PTB four-crystal monochromator beamline. *Nuclear Instruments and Methods in Physics Research Section A: Accelerators, Spectrometers, Detectors and Associated Equipment* **467–468, Part 2**, 1175–1178.
- KUČERKA, N., TRISTRAM-NAGLE, S. & NAGLE, J. F. 2006 Structure of Fully Hydrated Fluid Phase Lipid Bilayers with Monounsaturated Chains. *J Membrane Biol* **208**, 193–202.
- KUSAKA, T., NAKAYAMA, M., NAKAMURA, K., ISHIMIYA, M., FURUSAWA, E. & OGASAWARA, K. 2014 Effect of Silica Particle Size on Macrophage Inflammatory Responses. *PLoS ONE* **9**, e92634.
- LAGGNER, P., DEGOVICS, G., MÜLLER, K. W., GLATTER, O., KRATKY, O., KOSTNER, G. & HOLASEK, A. 1977 Molecular packing and fluidity of lipids in human serum low density lipoproteins. *Hoppe-Seyler's Z. Physiol. Chem.* **358**, 771–778.
- LASIC, D. D., FREDERIK, P. M., STUART, M. C. A., BARENHOLZ, Y. & MCINTOSH, T. J. 1992 Gelation of liposome interior A novel method for drug encapsulation. *FEBS Letters* **312**, 255–258.
- LEE, H. & PASTOR, R. W. 2011 Coarse-Grained Model for PEGylated Lipids: Effect of PEGylation on the Size and Shape of Self-Assembled Structures. *J. Phys. Chem. B* **115**, 7830–7837.

- LEFEBVRE, M., KEELER, R. K., SOBIE, R. & WHITE, J. 2000 Propagation of errors for matrix inversion. *Nuclear Instruments and Methods in Physics Research Section A: Accelerators, Spectrometers, Detectors and Associated Equipment* **451**, 520–528.
- LEONARD JR, B. R., ANDEREGG, J. W., KAESBERG, P. & BEEMAN, W. W. 1952 The Size of Latex Particles by X-Ray Scattering. *J Appl Phys* **23**, 152–152.
- LI, X., HIRSH, D. J., CABRAL-LILLY, D., ZIRKEL, A., GRUNER, S. M., JANOFF, A. S. & PERKINS, W. R. 1998 Doxorubicin physical state in solution and inside liposomes loaded via a pH gradient. *Biochimica et Biophysica Acta (BBA) - Biomembranes* **1415**, 23–40.
- LIANG, X., MAO, G. & NG, K. Y. S. 2005 Effect of chain lengths of PEO–PPO–PEO on small unilamellar liposome morphology and stability: an AFM investigation. *Journal of Colloid and Interface Science* **285**, 360–372.
- LIU, X., LU, S., ZHANG, J. & CAO, W. 2006 Thermal decomposition process of silver behenate. *Thermochimica Acta* **440**, 1–6.
- LUNDQVIST, M., STIGLER, J., ELIA, G., LYNCH, I., CEDERVALL, T. & DAWSON, K. A. 2008 Nanoparticle size and surface properties determine the protein corona with possible implications for biological impacts. *Proceedings of the National Academy of Sciences* **105**, 14265–14270.
- LUZZATI, V., TARDIEU, A. & AGGERBECK, L. P. 1979 Structure of serum low-density lipoprotein. *Journal of Molecular Biology* **131**, 435–473.
- MATHAI, J. C., TRISTRAM-NAGLE, S., NAGLE, J. F. & ZEIDEL, M. L. 2008 Structural Determinants of Water Permeability through the Lipid Membrane. *J Gen Physiol* **131**, 69–76.
- MELI, F., KLEIN, T., BUHR, E., FRASE, C. G., GLEBER, G., KRUMREY, M., DUTA, A., DUTA, S., KORPELAINEN, V., BELLOTTI, R., PICOTTO, G. B., BOYD, R. D. & CUENAT, A. 2012 Traceable size determination of nanoparticles, a comparison among European metrology institutes. *Meas. Sci. Technol.* **23**, 125005.
- MERTENS, H. D. & SVERGUN, D. I. 2010 Structural characterization of proteins and complexes using small-angle X-ray solution scattering. *J. Struc. Biol.* **172**, 128–141.

- MINELLI, C., GARCIA-DIEZ, R., SIKORA, A. E., GOLLWITZER, C., KRUMREY, M. & SHARD, A. G. 2014 Characterization of IgG-protein-coated polymeric nanoparticles using complementary particle sizing techniques. *Surf. Interface Anal.* **46**, 663–667.
- MITRAGOTRI, S. & LAHANN, J. 2009 Physical approaches to biomaterial design. *Nat Mater* **8**, 15–23.
- MONOPOLI, M. P., WALCZYK, D., CAMPBELL, A., ELIA, G., LYNCH, I., BALDELLI BOMBELLI, F. & DAWSON, K. A. 2011 Physical-Chemical Aspects of Protein Corona: Relevance to in Vitro and in Vivo Biological Impacts of Nanoparticles. *J. Am. Chem. Soc.* **133**, 2525–2534.
- MOTZKUS, F. 1959 Untersuchung kolloider Systeme auf Partikelgrösse und Polydispersität mit Hilfe der Röntgenkleinwinkelstreuung. *Acta Crystallogr* **12**, 773–786.
- MÜLLER, K., LAGGNER, P., GLATTER, O. & KOSTNER, G. 1978 The Structure of Human-Plasma Low-Density Lipoprotein B. *European Journal of Biochemistry* **82**, 73–90.
- MUNRO, J. M. & COTRAN, R. S. 1988 The pathogenesis of atherosclerosis: atherogenesis and inflammation. *Lab. Invest.* **58**, 249–261.
- MURPHY, R. M. 1997 Static and dynamic light scattering of biological macromolecules: what can we learn? *Current Opinion in Biotechnology* **8**, 25–30.
- MYKHAYLYK, O. O. 2012 Structural Characterization of Colloidal Core-shell Polymer-based Nanoparticles Using Small-angle X-ray Scattering. In *Proceedings of the International Conference Nanomaterials: Applications and Properties*, p. 01PCN04. Sumy State University Publishing.
- MYKHAYLYK, O. O., RYAN, A. J., TZOKOVA, N. & WILLIAMS, N. 2007 The application of distance distribution functions to structural analysis of core-shell particles. *J Appl Crystallogr* **40**, s506–s511.
- NAGLE, J. F., MATHAI, J. C., ZEIDEL, M. L. & TRISTRAM-NAGLE, S. 2008 Theory of Passive Permeability through Lipid Bilayers. *J Gen Physiol* **131**, 77–85.
- NEUMANN, A., HOYER, W., WOLFF, M. W., REICHL, U., PFITZNER, A. & ROTH, B. 2013 New method for density determination of nanoparticles using a CPS disc centrifuge<sup>TM</sup>. *Colloid Surface B* **104**, 27–31.

- NICHOLS, F. S. & FLOWERS, R. G. 1950 Prediction of Shrinkage in Addition Polymerizations. *Ind Eng Chem* **42**, 292–295.
- NICOLET, A., MELI, F., VAN DER POL, E., YUANA, Y., GOLLWITZER, C., KRUMREY, M., PETR CIZMAR, BUHR, E., PÉTRY, J., SEBAIHI, N., DE BOECK, B., FOKKEMA, V., BERGMANS, R. & RIENK NIEUWLAND 2016 Inter-laboratory comparison on the size and stability of monodisperse and bimodal synthetic reference particles for standardization of extracellular vesicle measurements. *Meas. Sci. Technol.* **27**, 035701.
- NIE, S., XING, Y., KIM, G. J. & SIMONS, J. W. 2007 Nanotechnology Applications in Cancer. *Annual Review of Biomedical Engineering* **9**, 257–288.
- OLBRICH, K., RAWICZ, W., NEEDHAM, D. & EVANS, E. 2000 Water Permeability and Mechanical Strength of Polyunsaturated Lipid Bilayers. *Biophysical Journal* **79**, 321–327.
- OTTEWILL, R. H., COLE, S. J. & WATERS, J. A. 1995 Characterization of particle morphology by scattering techniques. *Macromol Symp* **92**, 97–107.
- PATEL, T., ZHOU, J., PIEPMEIER, J. M. & SALTZMAN, W. M. 2012 Polymeric nanoparticles for drug delivery to the central nervous system. *Adv Drug Deliver Rev* **64**, 701–705.
- PEDERSEN, J. S. 1994 Determination of size distribution from small-angle scattering data for systems with effective hard-sphere interactions. *J. Appl. Cryst.* **27**, 595–608.
- PEDERSEN, J. S. 1997 Analysis of small-angle scattering data from colloids and polymer solutions: modeling and least-squares fitting. *Adv. Colloid Interfac.* **70**, 171–210.
- PERRET, R. & RULAND, W. 1972 Glassy carbon as standard for the normalization of small-angle scattering intensities. *Journal of Applied Crystallography* **5**, 116–119.
- POWERS, K. W., BROWN, S. C., KRISHNA, V. B., WASDO, S. C., MOUDGIL, B. M. & ROBERTS, S. M. 2006 Research Strategies for Safety Evaluation of Nanomaterials. Part VI. Characterization of Nanoscale Particles for Toxicological Evaluation. *Toxicol Sci* **90**, 296–303.



- RIBEIRO, A. C. F., ORTONA, O., SIMÕES, S. M. N., SANTOS, C. I. A. V., PRAZERES, P. M. R. A., VALENTE, A. J. M., LOBO, V. M. M. & BURROWS, H. D. 2006 Binary Mutual Diffusion Coefficients of Aqueous Solutions of Sucrose, Lactose, Glucose, and Fructose in the Temperature Range from (298.15 to 328.15) K. *J. Chem. Eng. Data* **51**, 1836–1840.
- ROSEN, H. & ABRIBAT, T. 2005 The rise and rise of drug delivery. *Nat Rev Drug Discov* **4**, 381–385.
- SAHOO, S. K. & LABHASETWAR, V. 2003 Nanotech approaches to drug delivery and imaging. *Drug Discovery Today* **8**, 1112–1120.
- SAKURAGI, M., KOIWAI, K., NAKAMURA, K., MASUNAGA, H., OGAWA, H. & SAKURAI, K. 2011 Transformation from Multilamellar to Unilamellar Vesicles by Addition of a Cationic Lipid to PEGylated Liposomes Explored with Synchrotron Small Angle X-ray Scattering. *Journal of Physics: Conference Series* **272**, 012011.
- SCHNITZER, E. & LICHTENBERG, D. 1994 Re-evaluation of the structure of low density lipoproteins. *Chemistry and Physics of Lipids* **70**, 63–74.
- SHAFFER, L. B. & HENDRICKS, R. W. 1974 Calibration of polyethylene (lupolen) as a wavelength-independent absolute intensity standard. *Journal of Applied Crystallography* **7**, 159–163.
- SILVERSTEIN, M. S., TALMON, Y. & NARKIS, M. 1989 Microstructure of polyacrylate/polystyrene two-stage lattices. *Polymer* **30**, 416–424.
- SIM, A. Y. L., LIPFERT, J., HERSCHLAG, D. & DONIACH, S. 2012 Salt dependence of the radius of gyration and flexibility of single-stranded DNA in solution probed by small-angle x-ray scattering. *Phys. Rev. E* **86**, 021901.
- SOPPIMATH, K. S., AMINABHAVI, T. M., KULKARNI, A. R. & RUDZINSKI, W. E. 2001 Biodegradable polymeric nanoparticles as drug delivery devices. *J. Control. Release* **70**, 1–20.
- SOU, K., ENDO, T., TAKEOKA, S. & TSUCHIDA, E. 2000 Poly(ethylene glycol)-Modification of the Phospholipid Vesicles by Using the Spontaneous Incorporation of Poly(ethylene glycol)-Lipid into the Vesicles. *Bioconjugate Chem.* **11**, 372–379.
- SPYRATOU, E., MOURELATOU, E. A., MAKROPOULOU, M. & DEMETZOS, C. 2009 Atomic force microscopy: a tool to study the structure, dynamics and stability of liposomal drug delivery systems. *Expert Opinion on Drug Delivery* **6**, 305–317.

- STUHRMANN, H. B. 2007 Contrast variation in X-ray and neutron scattering. *J. Appl. Cryst.* **40**, s23–s27.
- STUHRMANN, H. B. 2008 Small-angle scattering and its interplay with crystallography, contrast variation in SAXS and SANS. *Acta Crystallogr. A Found. Cryst.* **64**, 181–191.
- STUHRMANN, H. B. & KIRSTE, R. G. 1965 Elimination der intrapartikulären Untergrundstreuung bei der Röntgenkleinwinkelstreuung an kompakten Teilchen (Proteinen). *Z Phys Chem* **46**, 247–250.
- STUHRMANN, H. B. & KIRSTE, R. G. 1967 Elimination der intrapartikulären Untergrundstreuung bei der Röntgenkleinwinkelstreuung an kompakten Teilchen. II. *Z Phys Chem* **56**, 334–337.
- STUHRMANN, H. B., TARDIEU, A., MATEU, L., SARDET, C., LUZZATI, V., AGGERBECK, L. & SCANU, A. M. 1975 Neutron scattering study of human serum low density lipoprotein. *Proc Natl Acad Sci U S A* **72**, 2270–2273.
- SUN, X., TABAKMAN, S. M., SEO, W.-S., ZHANG, L., ZHANG, G., SHERLOCK, S., BAI, L. & DAI, H. 2009 Separation of Nanoparticles in a Density Gradient: FeCoC and Gold Nanocrystals. *Angew. Chem. Int. Edit.* **48**, 939–942.
- TAKAHASHI, K., KATO, H., SAITO, T., MATSUYAMA, S. & KINUGASA, S. 2008 Precise Measurement of the Size of Nanoparticles by Dynamic Light Scattering with Uncertainty Analysis. *Particle & Particle Systems Characterization* **25**, 31–38.
- TAO, L., HU, W., LIU, Y., HUANG, G., SUMER, B. D. & GAO, J. 2011 Shape-specific polymeric nanomedicine: emerging opportunities and challenges. *Exp Biol Med* **236**, 20–29.
- TARDIEU, A., MATEU, L., SARDET, C., WEISS, B., LUZZATI, V., AGGERBECK, L. & SCANU, A. M. 1976 Structure of human serum lipoproteins in solution. *Journal of Molecular Biology* **101**, 129–153.
- TENZER, S., DOCTER, D., KUHAREV, J., MUSYANOVYCH, A., FETZ, V., HECHT, R., SCHLENK, F., FISCHER, D., KIOUPTSI, K., REINHARDT, C., LANDFESTER, K., SCHILD, H., MASKOS, M., KNAUER, S. K. & STAUBER, R. H. 2013 Rapid formation of plasma protein corona critically affects nanoparticle pathophysiology. *Nat Nano* **8**, 772–781.

- TERRENO, E., DELLI CASTELLI, D., VIOLANTE, E., SANDERS, H. M., SOMMERDIJK, N. A. & AIME, S. 2009 Osmotically Shrunken LIPOCEST Agents: An Innovative Class of Magnetic Resonance Imaging Contrast Media Based on Chemical Exchange Saturation Transfer. *Chem. Eur. J.* **15**, 1440–1448.
- UEDAIRA, H. & UEDAIRA, H. 1985 Sugar-water interaction from diffusion measurements. *J. Solution. Chem.* **14**, 27–34.
- VAN BEURTEN, P. & VRIJ, A. 1981 Polydispersity effects in the small-angle scattering of concentrated solutions of colloidal spheres. *J. Chem. Phys.* **74**, 2744–2748.
- VARGA, Z., WACHA, A. & BÓTA, A. 2014 Osmotic shrinkage of sterically stabilized liposomes as revealed by time-resolved small-angle X-ray scattering. *Journal of Applied Crystallography* **47**, 35–40.
- VARGA, Z., WACHA, A., VAINIO, U., GUMMEL, J. & BÓTA, A. 2012 Characterization of the PEG layer of sterically stabilized liposomes: a SAXS study. *Chemistry and Physics of Lipids* **165**, 387–392.
- VAUTHIER, C., SCHMIDT, C. & COUVREUR, P. 1999 Measurement of the Density of Polymeric Nanoparticulate Drug Carriers by Isopycnic Centrifugation. *J. Nanopart. Res.* **1**, 411–418.
- VENDITTO, V. J. & SZOKA JR., F. C. 2013 Cancer nanomedicines: So many papers and so few drugs! *Advanced Drug Delivery Reviews* **65**, 80–88.
- VICENT, M. J. & DUNCAN, R. 2006 Polymer conjugates: nanosized medicines for treating cancer. *Trends Biotechnol* **24**, 39–47.
- VITTAZ, M., BAZILE, D., SPENLEHAUER, G., VERRECCHIA, T., VEILLARD, M., PUISIEUX, F. & LABARRE, D. 1996 Effect of PEO surface density on long-circulating PLA-PEO nanoparticles which are very low complement activators. *Biomaterials* **17**, 1575–1581.
- WANG, A. Z., LANGER, R. & FAROKHZAD, O. C. 2012 Nanoparticle Delivery of Cancer Drugs. *Annu Rev Med* **63**, 185–198.
- WERNECKE, J., GOLLWITZER, C., MÜLLER, P. & KRUMREY, M. 2014 Characterization of an in-vacuum PILATUS 1M detector. *J Synchrotron Radiat* **21**, 529–536.

- WICKLINE, S. A. & LANZA, G. M. 2003 Nanotechnology for Molecular Imaging and Targeted Therapy. *Circulation* **107**, 1092–1095.
- WOLFRAM, J., SURI, K., YANG, Y., SHEN, J., CELIA, C., FRESTA, M., ZHAO, Y., SHEN, H. & FERRARI, M. 2014 Shrinkage of pegylated and non-pegylated liposomes in serum. *Colloids and Surfaces B: Biointerfaces* **114**, 294–300.
- YAMAOKA, T., TABATA, Y. & IKADA, Y. 1994 Distribution and tissue uptake of poly(ethylene glycol) with different molecular weights after intravenous administration to mice. *Journal of pharmaceutical sciences* **83**, 601–606.
- YANG, F.-S., CALDWELL, K. D. & GIDDINGS, J. C. 1983 Colloid characterization by sedimentation field-flow fractionation: II. Particle-size distribution. *J Colloid Interf Sci* **92**, 81–91.
- YANG, Z., HUCK, W. T. S., CLARKE, S. M., TAJBAKHS, A. R. & TERENTJEV, E. M. 2005 Shape-memory nanoparticles from inherently non-spherical polymer colloids. *Nat Mater* **4**, 486–490.
- YEH, M.-K., HSIN-I CHANG & MING-YEN CHENG 2011 Clinical development of liposome based drugs: formulation, characterization, and therapeutic efficacy. *International Journal of Nanomedicine* p. 49.
- ZHAO, D., FENG, J., HUO, Q., MELOSH, N., FREDRICKSON, G. H., CHMELKA, B. F. & STUCKY, G. D. 1998 Triblock Copolymer Syntheses of Mesoporous Silica with Periodic 50 to 300 Angstrom Pores. *Science* **279**, 548–552.
- ZHOU, X., PORTER, A. L., ROBINSON, D. K. R., SHIM, M. S. & GUO, Y. 2014 Nano-enabled drug delivery: A research profile. *Nanomedicine: Nanotechnology, Biology and Medicine* **10**, e889–e896.